DYNAMIC RESERVOIR CHARACTERIZATION USING COMPLEX GRIDS BASED ON STREAMLINE AND FAST MARCHING METHODS

A Dissertation

by

YANBIN ZHANG

Submitted to the Office of Graduate Studies of
Texas A&M University
in partial fulfillment of the requirements for the degree of

DOCTOR OF PHILOSOPHY

Chair of Committee,	Akhil Datta-Gupta
Co-Chair of Committee,	Michael J. King
Committee Members,	Christine Ehlig-Economides
	Wolfgang Bangerth
Department Head,	A. Daniel Hill

August 2013

Major Subject: Petroleum Engineering

ABSTRACT

Dynamic reservoir characterization of large three dimensional earth models has become an increasingly important topic in recent years. Conventional finite difference reservoir simulation may not always be the optimal choice in such applications. Alternative methods such as the streamline method and the Fast Marching Method (FMM) could be advantageous in many cases. A comprehensive study to extend these methods to more complex grids is both theoretically interesting and practically beneficial. The ability to use complex grids greatly increases the applicability of these methods, for example, to model complex geologic structures, horizontal and multilateral wellbores, and complex hydraulic/natural fractures.

We present a comprehensive study of various velocity interpolation methods in polygons. These methods extend the widely used velocity interpolation algorithms, such as the Pollock's algorithm, to more complex geometries such as perpendicular bisection (PEBI) grids, unstructured triangular grids and grids with local refinement. We analyze important issues such as local conservation, velocity continuity, and orders of interpolation. Based on our analysis, we recommend a lower order locally conservative method for the most robust and numerically efficient calculation of streamline trajectories on unstructured grids. The proposed method is then applied to generate streamline visualizations for various grids.

Previous studies have demonstrated the use of the FMM and the diffusive time of flight for drainage volume visualization and pressure depletion estimation for unconventional reservoirs. In the current study, we first extend the FMM to corner point grids and anisotropic permeabilities. We then propose a new formulation of the diffusivity equation using the diffusive time of flight τ as a spatial coordinate.

This new τ-coordinate formulation reduces the problem from 3D to 1D in space. The basic formulation is extended by incorporating additional physical processes which are potentially important in shale gas reservoirs. The new formulation is validated by comparing with both analytical solution and traditional finite difference simulation. Our expectation is that the new formulation will become an efficient and versatile tool for pressure depletion and associated reservoir characterization applications.

DEDICATION

To my wife and parents

ACKNOWLEDGEMENTS

This dissertation would not have been possible without the guidance and help of my advisors, Dr. Datta-Gupta and Dr. King. I would like to express my utmost gratitude to them. They have taught me much more than just doing research.

I would like to thank my other committe members, Dr. Ehlig-Economides and Dr. Bangerth. They are both excellent teachers and I have learned many useful things not only from their classes but also from personal conversations with them.

Special thanks to Ms. Phaedra Hopcus and Mr. John Winkler who have done great services in the Department of Petroleum Engineering. Last but not least, I would like to thank many of my friends who worked with me during my study at Texas A&M University.

NOMENCLATURE

BHP	Bottom-hole Pressure
CV	Continuous Velocity
CVFE	Control Volume Finite Element
CVI	Corner Velocity Interpolation
EPM	Extended Pollock Method
FD	Finite Difference
FMM	Fast Marching Method
FV	Finite Volume
LC	Local Conservation
LGR	Local Grid Refinement
MFE	Mixed Finite Element
MPFA	Multipoint Flux Approximation
PDE	Partial Differential Equation
PEBI	Perpendicular Bisection
PSS	Pseudo-steady State
QR	Quadrilateral Refinement
TOF	Time of Flight
TPFA	Two Point Flux Approximation
TR	Triangular Refinement

TABLE OF CONTENTS

LIST OF FIGURES

FIGURE Page

LIST OF TABLES

TABLE Page

1. INTRODUCTION

Three-dimensional earth models play an increasingly central role in the petroleum industry. They are routinely used to plan new wells, calculate hydrocarbon reserves and forecast production. Usually due to sparse well coverage, earth models are often poorly constrained away from the well locations. This is where dynamic reservoir characterization could play an important role. Dynamic reservoir characterization is essentially solving an optimization problem, i.e. finding the "best" model(s) under certain constraints, which produces (by forward simulation) the closest calculated results compared to the observed dynamic data, e.g. production rate, gas oil ratio, and wellbore pressure. If the dynamic reservoir characterization is performed successfully, it is able to constrain the models, reduce uncertainties, and provide better predictions. The forward modeling technique to be used with the dynamic reservoir characterization should be selected according to specific problems. It is very important to strike a balance between accuracy and efficiency. The model has to be "accurate" enough in order to capture the principal physics. Efficiency is a big concern because the optimization usually involves not just one forward simulation but many. The traditional finite difference (FD) reservoir simulation may not be the best fit for all dynamic reservoir characterization applications. There are alternative methods that are able to capture most of the physics in a more intuitive and efficient manner. In this dissertation, we will discuss two of these alternative methods: the streamline method and the Fast Marching Method (FMM). The main focus of this dissertation is to systematically investigate various possible approaches of extending these methods to more complicated grid geometries, evaluate advantages and disadvantages of different approaches, and make recommendations for practitioners who

might want to implement these methods for industrial usage.

In the area of dynamic reservoir characterization, the application of streamline method has already been very successful and quite mature (*Datta-Gupta and King*, 2007). In recent years, due to the emerging next generation reservoir simulators as well as the new data exchange standard for reservoir characterization and modeling (*King et al.*, 2012), unstructured grids become more and more popular. In order to utilize their flexibility, especially for representing highly complex geologic structures and fluid flow near multilateral and fractured wellbore trajectories, the current streamline method has to be extended. In this work, we will address the fundamental problem of developing robust velocity interpolation models which are applicable in unstructured grids.

Although the theory of the FMM and its applications in many other areas have been quite mature (*Sethian*, 1999a), the FMM only becomes a hot topic in reservoir engineering recently in the context of the shale gas revolution (*Datta-Gupta et al.*, 2011). There are still many fundamental challenges to overcome in order to turn it into a useful and robust tool for dynamic reservoir characterization. Previous work by *Xie et al.* (2012a,b) has demonstrated the use of the FMM for drainage volume visualization and production forecasts in tight gas and shale gas reservoirs. These applications are based on regular square grid and isotropic permeabilities. In this work, we will extend these applications to more complex grids and anisotropic permeabilities. We will primarily concentrate on the corner point grid (CPG) due to its wide adoption in reservoir modeling.

The FMM is conceptually very closely related to the streamline method. One major advancement we have achieved in this dissertation is a completely novel way of formulating the pressure equation using the diffusive time of flight, τ, as a spatial coordinate calculated by the FMM. This is in close analogy with using the time of

flight along streamlines as a spatial variable for solving fluid transport. This new τ-coordinate formulation is able to reduce the pressure equation from three dimensional to only one dimensional in space. Compared with the previously proposed geometric approximation (*Xie et al.*, 2012a,b), the new formulation has several advantages. First, it is theoretically more general without the pseudo-steady state (PSS) assumption. Second, it is much easier to deal with complex well control. Third, it is much easier to be extended by incorporating additional physics, which might be important for shale gas reservoir production. Although we have obtained some promising results, this research is still in an early stage, and there are more work to be done in the future.

In the following subsection, we will briefly present some fundamental concepts and methods. The purpose is to give a background for the understanding of key issues and problems that will be fully addressed in later sections. After that, we will conclude this section by discussing the objectives of this research and introducing the outline of the following sections.

1.1 Fundamental Concepts and Methods

1.1.1 Streamline Tracing

Streamlines are instantaneous lines that are everywhere tangential to a velocity field (*Datta-Gupta and King*, 2007). Streamline tracing is the procedure to obtain the streamlines, and it is the very first step in order to apply the streamline method. The success of applying the streamline method will depend on the accuracy, efficiency, and robustness of the streamline tracing techniques used. The streamline tracing techniques we are going to discuss in this dissertation are based on inter-cell fluxes calculated by numerically solving the flow equations in a given mesh/grid. The major question we are trying to answer is that given these inter-cell fluxes how to

construct a suitable velocity field throughout the domain. Once the velocity field is constructed, the streamlines can be obtained by numerical integration. Here we will present the classic Pollock's algorithm (*Pollock*, 1988) as an example to show this process.

Pollock (1988)'s work was based on rectangular grids and the finite-difference numerical model. He used simple linear interpolation of the principal velocity components within a cell. Thus the principal velocity components can be expressed in the form

$$v_x = A_x(x - x_1) + v_{x1} \tag{1.1}$$

$$v_y = A_y(y - y_1) + v_{y1} \tag{1.2}$$

$$v_z = A_z(z - z_1) + v_{z1} \tag{1.3}$$

where A_x, A_y, and A_z are constants that correspond to the components of the velocity gradient within the cell

$$A_x = (v_{x2} - v_{x1})/\Delta x \tag{1.4}$$

$$A_y = (v_{y2} - v_{y1})/\Delta y \tag{1.5}$$

$$A_z = (v_{z2} - v_{z1})/\Delta z \tag{1.6}$$

The cell boundary velocities are linked with the inter-cell fluxes calculated in the finite-difference model. Once the velocity field is obtained, the streamlines can be described by the following differential equations

$$dt = \frac{dx}{v_x(x, y, z)} = \frac{dy}{v_y(x, y, z)} = \frac{dz}{v_z(x, y, z)} \tag{1.7}$$

For the velocity field given by Equations 1.1-1.3, Equation 1.7 can be analytically integrated from time t_1 to time $t_2 = t_1 + \Delta t$ as

$$x(t_2) = x(t_1) + \frac{1}{A_x}\left[v_x(t_1)\exp(A_x\Delta t) - v_{x1}\right] \tag{1.8}$$

$$y(t_2) = y(t_1) + \frac{1}{A_y}\left[v_y(t_1)\exp(A_y\Delta t) - v_{y1}\right] \tag{1.9}$$

$$z(t_2) = z(t_1) + \frac{1}{A_z}\left[v_z(t_1)\exp(A_z\Delta t) - v_{z1}\right] \tag{1.10}$$

According to these equations, given an initial position at time t_1, the coordinates at any future time t_2 can be computed analytically. To obtain where a streamline exits the cell, we can back solve for t_2 from each of the Equations 1.8-1.10 and the minimum value obtained will be the time of flight within the cell. Then the corresponding exit coordinates can be obtained. After that, the tracing can continue to the next cell until reaching a source or sink. The Pollock's algorithm produces a continuous velocity vector field within each individual grid cell that identically satisfies the differential conservation of mass equation everywhere within the cell (*Pollock*, 1988). This "locally conservative" property is very important and we will further discuss it in detail in section 2.

1.1.2 Asymptotic Solution of Diffusivity Equation

Asymptotic method is often used to capture some important characteristics of a complex problem and thus provides insight into the problem that may be obscured by its complicatedness. The asymptotic solution of diffusivity equation (*Virieux et al.*, 1994; *Vasco et al.*, 2000) enables us to capture the pressure "front" propagation in analogy to a wave front propagation. Here we start from the diffusivity equation for slightly compressible fluid which describes the transient pressure response in a

heterogeneous reservoir

$$\nabla \cdot \left(\frac{k(\mathbf{x})}{\mu} \nabla P(\mathbf{x}, t) \right) = \phi(\mathbf{x}) c_t \frac{\partial P(\mathbf{x}, t)}{\partial t} \tag{1.11}$$

Applying Fourier transform to this equation will lead to the following equation in the frequency domain

$$\nabla^2 \tilde{P}(\mathbf{x}, \omega) + \frac{\nabla k(\mathbf{x})}{k(\mathbf{x})} \cdot \nabla \tilde{P}(\mathbf{x}, \omega) + \frac{\phi(\mathbf{x}) \mu c_t}{k(\mathbf{x})} (i\omega) \tilde{P}(\mathbf{x}, \omega) = 0 \tag{1.12}$$

Here we choose an attempted solution of the form (*Virieux et al.*, 1994)

$$\tilde{P}(\mathbf{x}, \omega) = e^{-\sqrt{-i\omega}\tau(\mathbf{x})} \sum_{j=0}^{\infty} \frac{A_j(\mathbf{x})}{(\sqrt{-i\omega})^k} \tag{1.13}$$

Substituting this attempted solution into Equation 1.12 produces an expression with an infinite number of terms. By collecting terms of a given order in $\sqrt{-i\omega}$, we could obtain a series of equations:

$$(\sqrt{-i\omega})^2 : \qquad \nabla\tau(\mathbf{x}) \cdot \nabla\tau(\mathbf{x}) = \frac{\phi(\mathbf{x}) \mu c_t}{k(\mathbf{x})} \tag{1.14}$$

$$\sqrt{-i\omega} : \qquad A_0 \nabla^2 \tau + 2 \nabla A_0 \cdot \nabla \tau = 0 \tag{1.15}$$

$$(\sqrt{-i\omega})^{1-k} : \qquad \nabla^2 A_{k-1} - A_k \nabla^2 \tau + 2 \nabla A_k \cdot \nabla \tau = 0 \quad k \geq 1 \tag{1.16}$$

Equation 1.14, which is associated with the highest order $(\sqrt{-i\omega})^2$ terms, is called the Eikonal equation.

The physical meaning of the Eikonal equation can be obtained if we only consider the zeroth-order term in Equation 1.13 as the solution, i.e., in the high frequency limit,

$$\tilde{P}_{hf}(\mathbf{x}, \omega) = A_0(\mathbf{x}) e^{-\sqrt{-i\omega}\tau(\mathbf{x})} \tag{1.17}$$

If we convert this solution back into the time domain by inverse Fourier transformation, it can be shown that $\tau(\mathbf{x})$ is related to the time when the pressure disturbance is a maximum at point $\mathbf{x}$ (for an impulse point source at the origin). In three dimensional domain for example, we have $6t = \tau^2(\mathbf{x})$. For this reason, $\tau(\mathbf{x})$ is called the pseudo-phase (*Virieux et al.*, 1994) or the diffusive time of flight (*Datta-Gupta et al.*, 2011). The Eikonal equation is a statement that the diffusive time of flight is a function of $\phi\mu c_t/k$, or the inverse of the medium diffusivity. If we think of the medium diffusivity as the "velocity" of the propagating pressure front, then the Eikonal equation is analogous to Equation 1.7 for streamline calculation. However, there is a critical difference between the two: the diffusive time of flight can be calculated by the FMM efficiently without explicit tracing of trajectories, while streamline time of flight calculation requires streamline trajectory tracing.

It is noted that the derivation of the Eikonal equation does not require the medium to be homogeneous or smoothly varying. Therefore, the diffusive time of flight can also be defined by Equation 1.14 for heterogeneous and even non-smoothly varying medium. However, the physical meaning of $\tau(\mathbf{x})$ is only clear when the zeroth-order asymptotic solution is a valid approximation. This usually is only true if the background medium is homogeneous, nearly homogeneous or slightly heterogeneous with smoothly varying properties. It is observed that the Eikonal equation only depends on the inverse of diffusivity $\phi(\mathbf{x})\mu c_t/k(\mathbf{x})$, which appears in the third term of Equation 1.12. The second term of this equation contains the permeability gradient $\nabla k(\mathbf{x})$ and this term will become very important if the permeability changes drastically over short distances, e.g. in a channelized reservoir. Therefore, in highly heterogeneous and high-contrast medium, there are important and more complex physical characteristics of the pressure solution which cannot be captured by the Eikonal equation. For example, reflection and multiple arrival phenomena will become very important

near the sharp boundaries between high and low diffusivity medium (*Gupta*, 2012). These physics could only be captured by including higher order terms, which undermines the power of the asymptotic solution for problem reduction and simplification in the first place. In this dissertation, we assume slightly heterogeneous and smoothly varying medium for the derivation of the approximate pressure solution using the diffusive time of flight as a spatial variable. The improvement of this method for highly heterogeneous and high-contrast medium is still an active research area.

1.1.3 Depth of Investigation and Drainage Volume

Depth of investigation is an important concept in traditional pressure transient analysis. *Lee* (1982) proposed the definition to be the propagation distance of the maximum pressure draw-down for an impulse source. In 2D radial flow, the depth of investigation in field units is calculated by

$$r = \sqrt{\frac{kt}{948\phi\mu c_t}} \tag{1.18}$$

This equation is originally derived from the line-source analytical pressure transient solution in homogeneous reservoirs. More generally, for different flow patterns, the distance and time of the pressure front propagation can be written as

$$r = \sqrt{\beta\alpha t} \tag{1.19}$$

where α is the hydraulic diffusivity defined as $\alpha = k/(\phi\mu c_t)$, and β is a geometric factor related to the flow patterns. For linear, radial, and spherical flow, β is 2, 4, and 6 respectively (*Kim et al.*, 2009).

Drainage volume is a widely used concept in reservoir engineering to characterize the general connectivity of certain reservoir volume with a particular well or comple-

tion. It is a very practical term and often defined according to specific applications. For example, streamlines and time of flight might be useful to define the drainage volume in a water flooding application, while pressure depletion and depth of investigation might be more appropriate for a primary depletion application. In this dissertation, we will define the drainage volume using the diffusive time of flight calculated by solving the Eikonal equation. This can be achieved efficiently using the FMM. The drainage volume defined as such is basically an extension of the depth of investigation concept to heterogeneous reservoirs. This will be fully addressed in Section 3.

1.1.4 Shale Gas Reservoirs

Shale formations are traditionally well-known as possible source rock. In recently years, technologies such as horizontal well drilling and multistage hydraulic fracturing have made it possible to economically produce gas from some of these shale formations in very large scale, changing the entire landscape of the energy industry in the US. Because of the importance of shale gas, research around it becomes very popular recently. On one hand, traditional theories and models for gas flow in porous medium which were developed for conventional reservoirs have been applied to shale gas reservoirs with mixed results. On the other hand, people begin to look into the fundamental physical processes that are important in and might be unique to shale gas reservoirs. Although the process of gas release and production from shale gas sediments have not been very well understood, there are several physical processes which are commonly believed to play important roles in shale gas reservoirs, including reservoir compaction, gas adsorption, gas slippage, and gas diffusion. Therefore, it is important to be able to incorporate the additional physical processes in shale gas reservoirs into our new τ-coordinate formulation. This will be addressed in detail

in Section 4. Here we only briefly introduce these physical processes to provide some background information as they are not the main subject of this research.

Reservoir Compaction

Due to production from wells, the effective stress increases with the decrease in pore pressure. Increase in the effective stress compacts the reservoir rock and usually reduces reservoir porosity and/or the conductivity of natural fractures. This leads to a decrease in reservoir permeability. However, it is also possible that the increase in the effective stress results in shear failure of the reservoir rock and introduce secondary fractures (*Kim and Moridis*, 2012). In this case, these secondary fractures will increase the permeability significantly. Shale reservoirs are generally believed to be rather sensitive to these geomechanical effects. Either coupled or decoupled model can be used to incorporate the geomechanical effects into the flow simulation. The coupled model solves the geomechanical processes and the fluid flow simultaneously and thus are considered to be more accurate with a higher computational cost. The decoupled model uses pressure dependent reservoir constitutive properties, e.g. permeability and porosity, for the flow simulation part, while the relationships between these reservoir constitutive properties and the pore pressure are obtained by geomechanical analysis, modeling, or even empirical experiences.

Gas Adsorption

In shale gas reservoirs, the gas adsorption effect can be quite significant due to the high surface to volume ratio of the pore system in shales. The gas adsorption is usually modelled by the Langmuir isotherm (*Langmuir*, 1916):

$$V_{ads}(P) = \frac{V_L P}{P_L + P} \tag{1.20}$$

where V_{ads} is the amount of adsorbed gas at pressure P per unit volume (or mass) of shale. Parameters V_L and P_L are called the Langmuir volume and the Langmuir pressure respectively. The unit of V_{ads} is the same as the unit of the Langmuir volume V_L. In field units, V_L can be expressed in Mscf/ft^3, or thousand standard cubic feet of gas per cubic feet of shale. In equilibrium condition, when pressure drops, usually the amount of adsorbed gas as described by Equation 1.20 also drops, which indicates that some adsorbed gas is released from the pore surface to become free gas in the pore.

Gas Slippage Effect

In extremely low permeability reservoirs such as shale gas reservoirs, the gas molecules may slip along the pore surfaces and cause additional flux on top of the viscous flow expressed by Darcy's law (*Klinkenberg*, 1941; *Bravo*, 2007; *Javadpour*, 2009; *Shabro et al.*, 2011; *Swami and Settari*, 2012; *Fathi and Akkutlu*, 2013). This effect is usually modelled by an apparent permeability k_{app} which can be much larger than the Darcy permeability for nano-scale pore sizes.

Gas Diffusion from Kerogen

In addition to the adsorbed gas on the pore wall surface, some researchers have also studied the contribution of the diffused gas inside the kerogen in organic rich shale (*Javadpour et al.*, 2007; *Javadpour*, 2009; *Akkutlu and Fathi*, 2012; *Shabro et al.*, 2012). The diffusion of gas from the kerogen provides additional source to the gas production and may help maintain long term production. The gas diffusion is considered to be a relatively slow process compared to the advective flow in pores and fractures. Usually this process is formulated as dual/multi porosity models with specific transfer functions related to the intrinsic shale properties. Due to lack of experimental data, many critical model parameters in these studies are taken from

either coal bed methane data, or theoretical numbers, or speculations.

1.2 Objectives and Outline

Although the ultimate goal of this research is to do dynamic reservoir characterization, this dissertation mainly focuses on the forward modeling part of the entire problem. Hopefully future research will be able to build on the methods developed here and incorporate it organically into the entire dynamic reservoir characterization framework. The rest of this dissertation will be organized into three major sections followed by a summary. The objectives of each of the three major sections are as follows.

Section 2 will focus on the fundamental problem of developing robust velocity interpolation models which are applicable in unstructured grids. The objectives of this section include:

- Analyze the pros and cons of previously proposed velocity interpolation schemes, in particular the Extended Pollock Method (EPM) and the Corner Velocity Interpolation (CVI) method;
- Propose various alternative methods based on different choices of lower and higher order boundary flux interpolations, local conservation or non-conservation, velocity continuity or discontinuity;
- Evaluate the proposed schemes in terms of their accuracy, efficiency, and robustness;
- Make recommendations for future implementation;
- Apply the recommended scheme to both Perpendicular Bisection (PEBI) grids and grids with local refinements.

Section 3 primarily deals with the extension of the FMM to Corer Point Grids (CPG) and anisotropic permeabilities. Only a limited discussion is presented on unstructured grids as it is still an ongoing work and will be addressed in future research. The objectives of this section include:

- Develop the formulation of the Eikonal equation for CPG in anisotropic medium and the local discretized solution;
- Investigate the causality issue of the solution;
- Demonstrate the FMM for drainage volume calculation and visualization in synthetic shale gas reservoirs.

Section 4 will be dedicated to the new τ-coordinate formulation of the diffusivity equation. The objectives include:

- Rewrite the diffusivity equation using the diffusive time of flight τ as a spatial coordinate;
- Demonstrate that the new formulation reduces back to the original diffusivity equation for homogeneous medium;
- Incorporate the additional physical processes mentioned in Section 1.1.4 into the new formulation;
- Validate the new formulation by comparing its solution with either analytical solution or solution from a traditional finite difference simulation in various scenarios;
- Investigate the effects of gas adsorption and diffusion in shale gas reservoirs.

2. ROBUST STREAMLINE TRACING USING INTER-CELL FLUXES IN LOCALLY REFINED AND UNSTRUCTURED GRIDS*

2.1 Synopsis

Unstructured grids are an important topic in reservoir simulation and 3D geologic modeling due to their flexibility especially for representing highly complex geologic structures and fluid flow near multilateral and fractured wellbore trajectories. In recent years, this research topic has received even more attention in the context of the emerging next generation reservoir simulators as well as the new data exchange standard for reservoir characterization, earth and reservoir models (*King et al.*, 2012).

We present a comprehensive study of various velocity interpolation methods in polygons. These methods are often used as post-processing procedures for numerical schemes that do not directly calculate the velocity field but only provide cell boundary flux conditions, such as the finite volume schemes. These methods extend the widely used velocity interpolation algorithms, such as the Pollock's algorithm, to more complex geometries such as perpendicular bisection (PEBI) grids, unstructured triangular grids and grids with local refinement. Once the velocity field is interpolated, streamline trajectories and time of flight along the streamlines can be calculated for reservoir simulation, model calibration and water-flood management, for instance.

The velocity interpolation methods assume known lower order or higher order cell boundary fluxes, which satisfy global mass conservation and normal flux continuity. However, they differ in the interpolation of velocities within the interior of

*This material is reproduced with permission of John Wiley & Sons, Inc. from "Robust Streamline Tracing Using Inter-cell Fluxes in Locally Refined and Unstructured Grids" by Zhang, Y., King, M. J., and Datta-Gupta, A., 2012, *Water Resour. Res.*, 48(6), W06521

the cells. The interpolating velocity may be locally conservative or non-conservative, continuous or discontinuous, lower order or higher order. Results show that the interpolated velocity field has to be locally conservative in order to guarantee the correct volumetric transformation for the calculated streamlines and the time of flight. Velocity continuity is not as important as local conservation for the purpose of streamline applications. Compared to higher order interpolation for the streamline trajectories, lower order interpolation has the advantage of an analytic solution and an efficient implementation. Based on our analysis, we recommended a lower order locally conservative method for the most robust and numerically efficient calculation of streamline trajectories on unstructured grids (*Zhang et al.*, 2012).

2.2 Introduction

Streamline based methods are widely used for various subsurface flow modeling problems, especially for advection-dominated displacements. To apply these methods it is necessary to construct streamlines and calculate the time of flight (TOF) along each streamline in an accurate and robust manner. This is usually achieved in three steps. First, a simulator or a numerical method is used to obtain the cell boundary face fluxes. Second, a suitable velocity field is interpolated throughout the entire computational domain. Third, streamlines are integrated using the velocity field, and the time of flight calculated along those trajectories. Of these three steps, the third step is the most straight-forward and utilizes either analytic solutions or Runge-Kutta techniques for the trajectory calculation. The first step is outside the scope of the current study. However, we will discuss enough of the flux calculation to lay a solid foundation for the discussion of the velocity interpolation models, which is the main subject of this section.

Unstructured grids are an important topic in reservoir simulation and 3D geologic

modeling due to their flexibility especially for representing highly complex geologic structures and fluid flow near multilateral and fractured wellbore trajectories. In recent years, this research topic has received even more attention in the context of the emerging next generation reservoir simulators as well as the new data exchange standard for reservoir characterization, earth and reservoir models (*King et al.*, 2012). It is both theoretically important and practically necessary to develop velocity interpolation models which are applicable in unstructured grids. Some of the frequently encountered unstructured grids in field applications are shown in Figure 2.1 and will be discussed in detail later.

This section is organized as follows. We begin with a literature review of the numerical calculation of flux and of velocity models. The next sub-section is dedicated to a brief description of the problem to be solved, emphasizing the cell boundary conditions which then constrain the velocity interpolation discussions. Section 2.5 begins with an investigation of various velocity interpolation spaces in the unit square, and then discusses possible extensions of those velocity spaces to polygons. In Section 2.6, several alternative methods based on sub-cell refinement are proposed. The rest of this section evaluates the characteristics of the different velocity interpolation schemes and then demonstrates their application to several 2D and 3D reservoir modeling situations, including 2.5D PEBI grids, faulted grids, and grids with local refinement.

2.3 Literature Review

We start with a review of the numerical methods which have been proposed to solve the flow equations for various kinds of unstructured grids. These calculations determine the flux on the boundaries of our unstructured polygonal elements. The numerical methods themselves also offer insight into simpler velocity interpolation

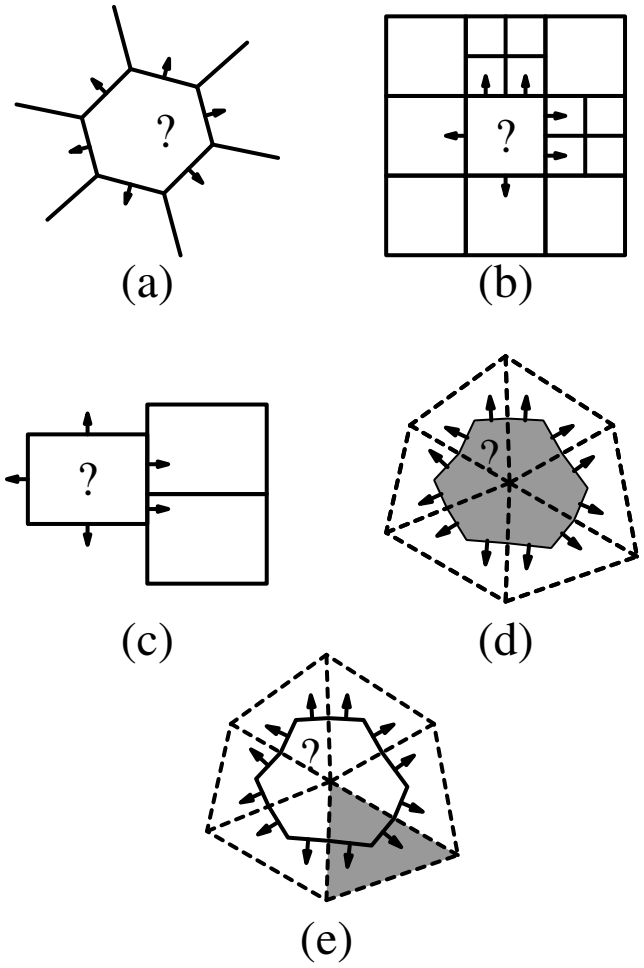

Figure 2.1: Velocity interpolation problem description in (a) PEBI cells, (b) LGR cells, (c) non-matching (faulted) cells, (d) point-distributed control volumes, (e) control volumes under CVFE scheme. Shaded areas in (d) and (e) have constant rock properties.

methods previously developed on triangular and quadrilateral grids. We have considered three different numerical approaches:

1. Finite Volume (FV),

2. Galerkin Finite Element (FE),

3. Mixed Finite Element (MFE).

The FV schemes can be further categorized into the cell-centered, the point-distributed, and the control volume finite element (CVFE) schemes. The common features of these schemes are:

1. the discretized system of equations is setup by applying mass conservation over the cells (called "mass conserving cells" in this section) of the grid or the dual grid, and

2. the face fluxes of these mass conserving cells are approximated in various ways from the pressures at the center of these mass conserving cells. We consider globally mass conservative schemes for which the flux is continuous across the face.

The distinction between the cell-centered and the point-distributed FV schemes is not essential, and they can be treated in a uniform manner as shown by *Aavatsmark et al.* (1998). Both the cell-centered and the point-distributed FV schemes define the rock properties as piecewise constant over the mass conserving cells, which may be polygons. In contrast, the CVFE schemes define the rock properties as piecewise constant over the triangular or quadrilateral cells, where pressure is interpolated by piecewise linear or bilinear functions (*Prakash*, 1987; *Forsyth*, 1990). For the CVFE schemes, the rock properties within a mass conserving cell (control volume) need

not be homogeneous. The flux approximation for the cell-centered and the point-distributed FV schemes can be either two-point or multi-point. Usually the two-point flux approximation (TPFA) is used for structured corner point grids or perpendicular bisection (PEBI) grids (K-orthogonal PEBI grids in general). For rigorous treatment of full tensor permeability and/or highly distorted grids, the multi-point flux approximation (MPFA) is necessary (*Aavatsmark et al.*, 1998; *Edwards and Rogers*, 1998; *Lee et al.*, 2002). For each interface between two mass conserving cells, TPFA calculates one flux on the interface while MPFA calculates two half face fluxes. For the CVFE schemes, the flux approximation is obtained from the piecewise linear or bilinear pressure interpolation in each triangular or quadrilateral cell.

The Galerkin FE schemes solve for pressure on the grid using a linear or bilinear interpolation over the triangular or quadrilateral cells. The rock properties are assumed to be piecewise constant over the same cells. The MFE schemes solve simultaneously for both pressure and velocity.

Of these numerical schemes, only the MFE schemes contain explicit velocity interpolation which may be used for streamline tracing. We will not discuss this particular application since it has already been extensively studied by other authors, e.g. *Darlow et al.* (1984) and *Matringe et al.* (2007). However, the velocity interpolation methods developed in the MFE schemes provide a foundation for the current paper. We will focus on the the other numerical schemes, for which the velocity field is not directly available but needs to be interpolated afterwards.

Pollock (1988) proposed a velocity interpolation method for rectangular cells constrained by the cell face fluxes. This was later extended to corner point cells by other authors (*Cordes and Kinzelbach*, 1992; *Prévost et al.*, 2001; *Jimenez et al.*, 2005) on the basis of the lowest order Raviat-Thomas (RT_0) space and an isoparametric mapping. We will call this the Extended Pollock Method (EPM). *Hægland et al.* (2007)

developed a Corner Velocity Interpolation (CVI) method for corner point cells constrained also by the cell face fluxes. The CVI method addressed the issue of reconstructing uniform flow, removing a grid orientation effect for corner point grids from the previous methods. *Matringe et al.* (2006) introduced the Brezzi-Douglas-Marini space of order one (BDM_1) for streamline tracing in order to improve accuracy. This velocity interpolation is of a higher order than the RT_0 space and has been shown to work with MPFA FV schemes which calculate half face fluxes for triangles or quadrilaterals (*Matringe et al.*, 2008).

All the above velocity interpolation methods have been developed for triangular or quadrilateral cells in 2D and tetrahedral or hexahedral cells in 3D. When the mass conserving cells are of these geometries just mentioned, they can be applied directly to interpolate the velocity field within each cell. However, the following two cases make things more complicated:

1. the face fluxes originally obtained for triangular or quadrilateral cells are not continuous across the cell faces;

2. the mass conserving cells, with which the face fluxes are associated, are not triangles or quadrilaterals but n-polygons ($n > 4$).

In the first case, post-processing is necessary in order to recover global mass conservation and flux continuity. For example, using the Galerkin FE numerical scheme the velocity obtained by directly taking the gradient of the pressure field will not satisfy flux continuity. This velocity field, if unprocessed, will give poor streamline tracing results due to spurious sources and sinks introduced on the cell faces. *Cordes and Kinzelbach* (1992) discussed this problem and proposed a post-processing procedure. The idea is to first introduce more degrees of freedom by dividing cells into sub-cells and then using mass conservation, flux continuity, and irrotational-

ity in a local "patch" to constrain the newly introduced degrees of freedom. For triangular based grids, the velocity interpolation they used was piecewise constant over sub-triangles. Such a velocity model does not have enough degrees of freedom to represent compressible flow, which is required in general. For quadrilateral based grids, sub-quadrilateral face fluxes are reconstructed first and then the velocity can be interpolated by the EPM. Later *Prévost et al.* (2001) pointed out that the sub-triangular construction cannot be applied to triangular based grids under the point-distributed FV schemes since the rock properties may no longer be constant within a triangular cell. They proposed to use sub-quadrilaterals rather than sub-triangles for triangular based grids, which leads to a construction similar to the CVFE scheme. They also demonstrated that for divergence free velocity fields their sub-quadrilateral construction will reproduce exactly the same exit point as the sub-triangular construction. However, they did not discuss the case of compressible flow. *Sun et al.* (2005) proposed a general velocity post-processing approach based on the Gauss-Seidel method to recover local mass conservation and flux continuity simultaneously. The method can work directly on the original grid of the Galerkin FE scheme instead of the dual grid, but it requires solving a global optimization problem by iteration. It also requires a priori knowledge of the source terms, which may be difficult to obtain accurately for compressible, multi-phase flow.

The second case (i.e. mass conserving and flux continuous n-polygons) is the focus of this section. It occurs when using cell-centered FV scheme for PEBI grids or grids with faults and/or local grid refinement (LGR). It also occurs when using point-distributed FV scheme or CVFE schemes for unstructured triangular or quadrilateral grids. There are basically two strategies to solve this problem:

1. finding direct extensions of the existing velocity interpolation spaces to n-

polygons;

2. dividing the n-polygons into sub-triangles or sub-quadrilaterals.

Recently *Rasmussen* (2010) attempted the first strategy by extending CVI to polygonal cells. The previous work of *Cordes and Kinzelbach* (1992) and *Prévost et al.* (2001) have already shed some light on the second strategy. The current paper will systematically investigate both strategies and propose the most robust and efficient methods to be used under different circumstances based on both theoretical analysis and numerical experiments.

2.4 Problem Description

Let us consider a polygonal shaped mass conserving cell which arises in the discretization of some FV scheme. The Galerkin FE scheme can be treated in the same way as CVFE scheme just by introducing control volumes. The numerical solution of the flow equations will provide fluxes on the cell interfaces. This flux information is global because the cell interface fluxes satisfy conservation for each mass conserving cell and continuity across neighboring cells. The velocity interpolation methods, on the other hand, only work locally within each mass conserving cell, consistent with these fluxes. This means that the global cell face flux information serves as *known* boundary conditions for the velocity interpolation of a particular mass conserving cell.

As just mentioned, the boundary conditions provide knowledge of the face fluxes. When we utilize lower order boundary conditions, we mean that flux along the boundary face is uniform, i.e. the normal component of the velocity is characterized by a single average value. When we utilize higher order boundary conditions, the normal component of the velocity varies linearly, i.e. it is characterized by two variables: the average and the slope of variation. (Note that in 3D there is a distinction between

the same boundary conditions in the physical cell and in the isoparametric reference cell, but in 2D they are equivalent (*Hægland et al.*, 2007).) In particular, a lower order boundary condition can be viewed as a constrained higher order boundary condition with zero slope of the linear variation. Thus a general discussion can be made assuming higher order boundary conditions; the results for lower order boundary conditions arise as a special case.

The boundary conditions can be equivalently expressed by corner velocities instead of fluxes for the non-degenerate cases. As shown in Figure 2.2, if the angle between two adjacent faces is different from π, the face fluxes can be used to uniquely define the corner velocities. When the angle between two adjacent faces is close to π (degenerate case), the corner velocity will not be well defined. The degenerate case may occur for grids with local grid refinement and faults, as well as CVFE grids. The unrobustness caused by the degeneracy of the physical cell will be addressed in section 2.5.2 and 2.5.3.

It is worth mentioning that *Matringe and Gerritsen* (2004) have proposed a local refinement tracing method where the boundary conditions on the subgrid are determined using the fluxes of the neighboring coarse blocks with a "slope limiter". This will generate a higher order boundary condition for the coarse blocks without using a higher order numerical scheme for the fluxes. If a similar method was developed for unstructured grids, it would be immediately applicable to our analysis since we start with the known boundary conditions.

The various situations that are frequently encountered in practice are depicted in Figure 2.1 and explained as follows. As mentioned earlier, TPFA calculates one average flux for each interface between two cells. This is most often seen in simulations using PEBI grids, grids with LGR's, and grids with faults as shown in Figure 2.1 (a), (b), and (c). The point-distributed FV schemes for unstructured grids usually

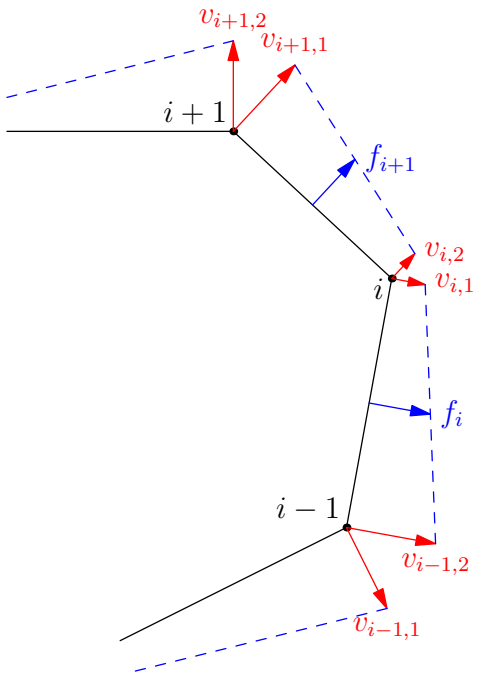

Figure 2.2: The degrees of freedom for a polygonal cell. The degrees of freedom may be associated with the average flux and the slope of linear variation of flux for each face (blue). Or equivalently they may be associated with the components of corner velocities (red).

require MPFA, which is able to calculate two half face fluxes. As shown in Figure 2.1(d), the interface between two mass conserving cells is part of a non-convex polygon and consists of two straight lines. Thus for the polygonal cell, only one average flux is known for each edge of the polygon. The situation of the CVFE schemes are similar to that of the point-distributed FV schemes as shown in Figure 2.1(e). The only difference is that the CVFE scheme is based on heterogeneous rock properties within the polygonal cell. Note that all the situations depicted in Figure 2.1 involve only lower order boundary conditions. Thus for practical purposes and simplicity, the test cases and examples in this section assume lower order boundary conditions. However, the theory and the methods developed in this section are not restricted to lower order boundary conditions.

Now that we have discussed the boundary conditions, the problem we are trying to solve becomes easier to state. The local velocity field within a cell is not determined uniquely by the boundary conditions. It also depends on the local velocity interpolation method used, which will make assumptions of the functional form of the local velocity field as well as certain properties that it should satisfy. As a basic requirement, the velocity interpolation method should provide sufficient degrees of freedom in order to be able to honor the boundary flux conditions; on the other hand, it should not introduce too many additional degrees of freedom without physically meaningful constraints on the velocity field to obtain a robust solution.

The following discussion will focus on 2D situations. The extension to 3D is straightforward in some cases but may require additional study for some classes of 3D unstructured grids.

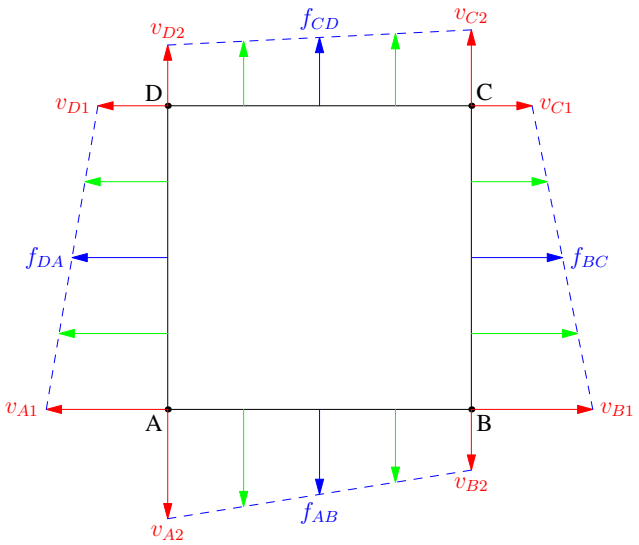

Figure 2.3: The degrees of freedom for the unit square.

2.5 Velocity Interpolation Spaces

In this section, we will discuss the first strategy mentioned in the literature review, namely finding direct extensions of the existing velocity interpolation spaces to n-polygons. We will begin with a discussion in the unit square.

2.5.1 Velocity Interpolation Spaces in the Unit Square

As shown by Figure 2.3, in the unit square the eight degrees of freedom can be equivalently associated with the eight half face fluxes or the eight corner velocity components. In order to treat the RT_0, CVI, and BDM_1 spaces in a uniform manner, we will use the eight corner velocity components as degrees of freedom in the following discussions.

RT_0 Space

The lowest order shape function associated with v_{C1} and v_{C2} in Figure 2.3 is

$$\begin{pmatrix} \alpha \\ 0 \end{pmatrix} \tag{2.1}$$

It is uniform on the face. The normal component of the velocity vanishes on all other faces (Figure 2.4(a)). The divergence of this shape function is simply 1. Such a velocity field is locally conservative, but is also sufficiently general to represent compressible fluid flow. The other three shape functions may be obtained by rotation and reflection symmetry. For example, by rotation symmetry, the shape function associated with v_{C2} and v_{D2} in Figure 2.3 is $\begin{pmatrix} 0 \\ \beta \end{pmatrix}$. Then the other two shape functions can be obtained by reflection symmetry, specifically substituting α with $1-\alpha$ and β with $1-\beta$ to obtain $\begin{pmatrix} 1-\alpha \\ 0 \end{pmatrix}$ and $\begin{pmatrix} 0 \\ 1-\beta \end{pmatrix}$. The velocity field that can be represented in this basis can be written as the linear combination of the four shape functions:

$$\begin{aligned} \mathbf{U}_{RT_0} = & f_{BC} \begin{pmatrix} \alpha \\ 0 \end{pmatrix} + f_{CD} \begin{pmatrix} 0 \\ \beta \end{pmatrix} + \\ & f_{DA} \begin{pmatrix} 1-\alpha \\ 0 \end{pmatrix} + f_{AB} \begin{pmatrix} 0 \\ 1-\beta \end{pmatrix} \end{aligned} \tag{2.2}$$

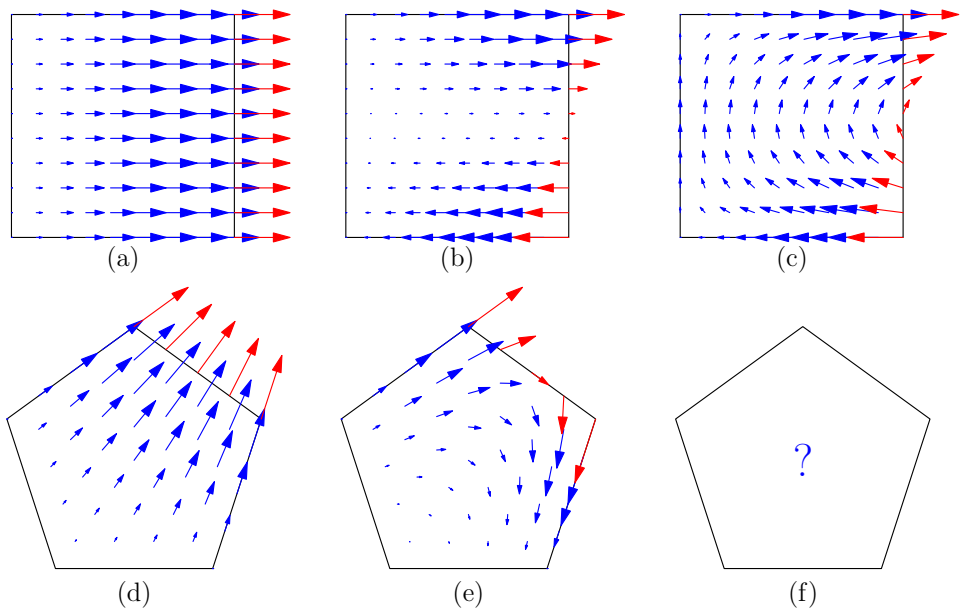

Figure 2.4: (a) A shape function of the RT_0 space in the unit square; (b) a higher order shape function of the CVI space in the unit square; (c) a higher order shape function of the BDM_1 space in the unit square; (d) a lower order shape function of the CVI space in the unit pentagon; (e) a higher order shape function of the CVI space in the unit pentagon; (f) the higher order shape function of the BDM_1 space in the unit pentagon is not known.

For the RT_0 space, we have $f_{BC} = v_{B1} = v_{C2}$ and similar relations on the other three boundary faces. The above velocity field can be simplified as

$$\mathbf{U}_{RT_0} = \begin{pmatrix} a_1 + b_1\alpha \\ a_2 + c_2\beta \end{pmatrix} \tag{2.3}$$

CVI Space

The CVI space consists of the RT_0 space with additional higher order shape functions. For instance, the higher order shape function, orthogonal to the RT_0

basis but associated with v_{C1} and v_{C2} in Figure 2.3, is

$$\begin{pmatrix} \alpha(\beta - \frac{1}{2}) \\ 0 \end{pmatrix} \tag{2.4}$$

Figure 2.4(b) shows this shape function. The total flux through the face vanishes but the local velocity does not. The divergence of this shape function is calculated to be $\beta - \frac{1}{2}$, which is not constant in the cell. This means that this interpolation space is not locally conservative. The upper half of the cell acts as a source while the lower half of the cell is a sink. The other three higher order shape functions can be obtained easily by reflection and rotation symmetry. The velocity field interpolated is the linear combination of all the shape functions:

$$\mathbf{U}_{CVI} = \begin{pmatrix} v_{C1}\alpha\beta + v_{B1}\alpha(1-\beta) - \\ v_{D1}(1-\alpha)\beta - v_{A1}(1-\alpha)(1-\beta) \\ \\ v_{C2}\alpha\beta - v_{B2}\alpha(1-\beta) + \\ v_{D2}(1-\alpha)\beta - v_{A2}(1-\alpha)(1-\beta) \end{pmatrix} \tag{2.5}$$

This can be rearranged into the following with only linear and bilinear terms:

$$\mathbf{U}_{CVI} = \begin{pmatrix} a_1 + b_1\alpha + c_1\beta + d_1\alpha\beta \\ a_2 + b_2\alpha + c_2\beta + d_2\alpha\beta \end{pmatrix} \tag{2.6}$$

BDM_1 Space

Similar to the CVI basis, the higher order shape function associated with v_{C1} and v_{C2} in Figure 2.3 is:

$$\begin{pmatrix} \alpha(\beta - \frac{1}{2}) \\ \frac{1}{2}\beta(1-\beta) \end{pmatrix} \tag{2.7}$$

Figure 2.4(c) shows this shape function. The divergence of this shape function is identically zero; this interpolation space is locally conservative. Compared with CVI space, the addition of the quadratic term $\frac{1}{2}\beta(1-\beta)$, which vanishes at the four corners, makes the interior velocity field locally conservative. The other three higher order shape functions can be obtained easily by reflection and rotation symmetry. The velocity field interpolated is the linear combination of all the shape functions:

$$\mathbf{U}_{BDM_1} = \begin{pmatrix} v_{C1}\alpha\beta + v_{B1}\alpha(1-\beta) - \\ v_{D1}(1-\alpha)\beta - v_{A1}(1-\alpha)(1-\beta) + \\ \frac{1}{2}(v_{C2} + v_{B2} - v_{D2} - v_{A2})\alpha(1-\alpha) \\ \\ v_{C2}\alpha\beta - v_{B2}\alpha(1-\beta) + \\ v_{D2}(1-\alpha)\beta - v_{A2}(1-\alpha)(1-\beta) + \\ \frac{1}{2}(v_{C1} - v_{B1} + v_{D1} - v_{A1})\beta(1-\beta) \end{pmatrix} \tag{2.8}$$

This can be rearranged into the following with linear, bilinear, and quadratic terms:

$$\mathbf{U}_{BDM_1} = \begin{pmatrix} a_1 + b_1\alpha + c_1\beta + d_1\alpha\beta + \frac{1}{2}d_2\alpha(1-\alpha) \\ a_2 + b_2\alpha + c_2\beta + d_2\alpha\beta + \frac{1}{2}d_1\beta(1-\beta) \end{pmatrix} \tag{2.9}$$

$$= \mathbf{U}_{CVI} + \begin{pmatrix} \frac{1}{2}d_2\alpha(1-\alpha) \\ \frac{1}{2}d_1\beta(1-\beta) \end{pmatrix} \tag{2.10}$$

The BDM_1 space can be viewed as the CVI space plus an extra term which has zero contribution at the corners but cancels out the variation of divergence in the interior.

2.5.2 Isoparametric Mapping

An isoparametric mapping is used to define a corner point simulation grid as a mapping from a unit square (or cube in 3D) to a general cell defined by the location of its corners in 2D or 3D. The following discussion is quite general. It can be applied to n-polygons and is not restricted to the unit square. Suppose that the corners of the reference cell are $\hat{\mathbf{x}}_i (i = 1, 2, \cdots, n)$, and the isoparametric mapping maps the reference cell corner $\hat{\mathbf{x}}_i$ to the corner $\mathbf{x}_i$ of the physical cell. A point $\hat{\mathbf{x}}$ in the reference cell can be written as

$$\hat{\mathbf{x}} = \sum_{i=1}^{n} \hat{\phi}_i(\hat{\mathbf{x}}) \hat{\mathbf{x}}_i \tag{2.11}$$

where $\hat{\phi}_i$ are generalized barycentric coordinates (*Wachspress*, 1975; *Floater et al.*, 2006). Then the point image of $\hat{\mathbf{x}}$ in the physical cell can be written as

$$\mathbf{x} = \sum_{i=1}^{n} \hat{\phi}_i(\hat{\mathbf{x}}) \mathbf{x}_i \tag{2.12}$$

The above equation can be seen as the coordinate transformation from $\hat{\mathbf{x}}$ to $\mathbf{x}$ (see Figure 2.5 as an example for pentagons). The velocity transformation usually adopted is called the Piola transformation, which has the property of preserving boundary flux (*Brezzi and Fortin*, 1991). According to the Piola transformation, the velocity $\hat{\mathbf{u}}$ at point $\hat{\mathbf{x}}$ in the reference cell can be transformed to the velocity $\mathbf{u}$ at point $\mathbf{x}$ in the physical cell by

$$\mathbf{u} = \frac{1}{\det(\mathbf{J})} \mathbf{J} \hat{\mathbf{u}} \tag{2.13}$$

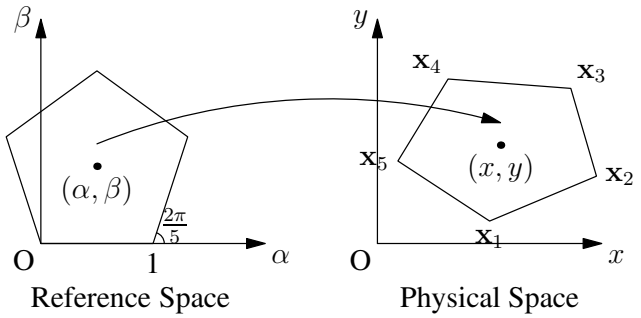

Figure 2.5: Isoparametric mapping for a pentagon.

where the Jacobian matrix $\mathbf{J}$ is defined as

$$\mathbf{J} = \frac{\partial \mathbf{x}}{\partial \hat{\mathbf{x}}} = \frac{\partial(x, y)}{\partial(\alpha, \beta)} \tag{2.14}$$

and is calculated from Equation 2.12.

The equations of motion for streamline trajectories in the physical cell are

$$\phi \frac{d\mathbf{x}}{dt} = \mathbf{u} \tag{2.15}$$

Converting into the reference cell we have

$$\phi \frac{d\mathbf{x}}{dt} = \phi \mathbf{J} \frac{d\hat{\mathbf{x}}}{dt} = \mathbf{u} = \frac{1}{\det(\mathbf{J})} \mathbf{J}\hat{\mathbf{u}} \tag{2.16}$$

or,

$$\phi \det(\mathbf{J}) \frac{d\hat{\mathbf{x}}}{dt} = \hat{\mathbf{u}} \tag{2.17}$$

We can introduce the time variable in the reference cell T, related to the physical time of flight using

$$t = \phi \int \det(\mathbf{J}) dT \tag{2.18}$$

In the reference cell, the trajectory is now easy to calculate

$$\frac{d\hat{\mathbf{x}}}{dT} = \hat{\mathbf{u}} \tag{2.19}$$

The Jacobian is a known function in the reference space. Once the trajectory in reference space is calculated as a function of T, then Equation 2.18 can be integrated to determine the actual time of flight across the polygonal cell. Using Equations 2.12, 2.18, and 2.19 is more robust than using Equations 2.13 and 2.15 for streamline tracing. The reason is that if the physical cell is degenerate or non-convex, the Jacobian may become zero or negative, and consequently Equation 2.13 may not be well defined. However, Equations 2.12, 2.18, and 2.19 will still remain applicable. The interpolation of velocity in the reference space, together with the technique shown here, makes the RT_0 and BDM_1 velocity interpolation methods robust for both non-convex and degenerate quadrilaterals.

2.5.3 Velocity Interpolation in Polygons

In this section we will seek direct extensions of the previously discussed continuous velocity spaces, i.e. the CVI space and the BDM_1 space, to n-polygons ($n > 4$). Such extensions should produce continuous velocity field interpolations in n-polygons just as they do for triangles and quadrilaterals. This is desirable for cells with homogeneous rock properties, which is almost always the case for triangles and quadrilaterals but only true for polygons under the cell-centered or the point-distributed FV schemes.

CVI in Polygons

Rasmussen (2010) recently proposed an extension of the CVI method to convex polygons. The interpolation can be written as

$$\mathbf{u} = \sum_{i=1}^{n} \phi_i \mathbf{u}_i \tag{2.20}$$

where the weights ϕ_i are given by generalized barycentric coordinates in the convex n-polygon, e.g. the Wachspress coordinates (*Wachspress*, 1975). The interpolation is directly carried out in the physical cell without the application of an isoparametric mapping. The limitation of this extension is that it cannot be applied to degenerate or non-convex polygons. First, in degenerate or non-convex polygons the generalized barycentric coordinates ϕ_i are not well defined. Second, in degenerate cells, some corner velocities may not be well defined, as shown in section 2.4. We must point out that Rasmussen's CVI method does *not* reduce to Hægland's CVI method (*Hægland et al.*, 2007) for the case of $n = 4$.

The original CVI method proposed by *Hægland et al.* (2007) for quadrilaterals can be expressed as

$$\mathbf{u} = \sum_{i=1}^{4} \hat{\phi}_i \mathbf{u}_i \tag{2.21}$$

A direct extension of this equation to n-polygons should be

$$\mathbf{u} = \sum_{i=1}^{n} \hat{\phi}_i \mathbf{u}_i \tag{2.22}$$

Note that the weighting functions $\hat{\phi}_i$ are the generalized barycentric coordinates in the reference cell rather than the physical cell. Please compare Equation 2.20 with Equation 2.22 to see why Rasmussen's extension does not reduce to Hægland's

CVI method. Because the reference cell is always a convex polygon, the weighting functions $\hat{\phi}_i$ are always well defined even if the physical cells are degenerate or non-convex. This is why Hægland's CVI method does not require the cell to be convex. However, this method still fails when the polygon has degenerate adjacent faces because of the inability to calculate the corner velocity from the face flux just as with Rasmussen's method. In addition, to apply Equation 2.22, it is necessary to map points from the physical cell back to the reference cell, i.e. solve for $\hat{x}$ from Equation 2.12. This requires numerical iterations which is computationally expensive.

We propose a new robust CVI method which is applicable for both degenerate and non-convex polygons. This new method interpolates the velocity field in the reference cell rather than in the physical cell:

$$\hat{\mathbf{u}} = \sum_{i=1}^{n} \hat{\phi}_i \hat{\mathbf{u}}_i \tag{2.23}$$

Using the isoparametric mapping technique developed in section 2.5.2, we will trace streamline trajectories in the reference cell and then map them to the physical cell. Because the velocity interpolation and integration are both carried out in the reference cell, this method will be robust regardless of the geometry of the physical cell. Moreover, unlike Hægland's CVI method, this method does not require the expensive back-mapping from the physical cell to the reference cell.

We have presented three different CVI methods for polygons. Rassmussen's method has the simplest form without any notion of isoparametric mapping, but it cannot be applied to degenerate and non-convex polygons. Hægland's method interpolates velocity in the physical cell but calculates the weights in the reference cell. It is not robust for degenerate polygons and requires expensive back-mapping from the physical cell to the reference cell. We propose a new robust method ap-

plicable for both degenerate and non-convex polygons which avoids the expensive back-mapping. Both the Rasmussen and the Hægland methods will preserve a uniform velocity, which is the intent of their constructions. The isoparametric extension of the CVI method, Equation 2.23, need not have this property. Uniform velocities will be preserved if the Jacobian of the isoparametric mapping belongs to the space spanned by the nodal basis functions, $\{\hat{\phi}_i\}$. Otherwise the direction of uniform velocities is preserved, but not the magnitude.

There are two major drawbacks of all three CVI methods. First, they are not locally conservative, the consequences of which will be discussed in Section 2.7.1. Second, in general, the numerical computation of the trajectory cannot be obtained analytically and requires a more expensive numerical integration.

BDM_1 in Polygons

As we have already shown in the unit square (section 2.5.1), the BDM_1 space can be seen as the CVI space with an additional velocity term which has zero contribution at the corners but cancels out the variation of divergence in the interior. Figure 2.4 (a) and (b) show the shape functions of the CVI space and BDM_1 space in the unit square. The mass conserving term provides a circulation in the BDM_1 space which is not present in the CVI space. As an example, Figure 2.4 (d) and (e) show the lower order and the higher order shape functions of the CVI space in the unit pentagon. They are similar to (b) in that the velocity direction is maintained but the magnitude of the velocity reduces away from the corners. For n-polygons, the basis functions are rational functions of $n-1$ polynomials. The divergence of such a velocity field is not constant. By analogy, the shape function of the BDM_1 space in the unit pentagon should have an extra term which has zero contribution at all five corners but cancels out the variation of divergence in the interior of the pentagon. For pentagon and

n-polygons ($n > 4$) in general, such a velocity field has not been constructed and is unlikely to have a simple analytical expression. In other words, a direct extension of BDM_1 to arbitrary polygons is not known.

2.6 Sub-cell Refinement Methods

The CVI schemes provide a method for smooth interpolation of properties within polygons. However, if we wish to work with conservative velocity fields, then no solution is known for n-polygons once $n > 4$. In such a case, we may refine the polygon into either triangles or quadrilaterals, and then use conservative schemes on the sub-cells. The problem then becomes one of flux reconstruction on the sub-cells, knowing the flux on the boundary of the polygon. This is the approach that we will study in this section.

In Section 2.4 we discussed the various situations where polygonal cells arise. For the situations shown in Figure 1 (d) and (e), the n-polygon has already been naturally refined into quadrilaterals by the faces of the triangular grid cells, although a triangular refinement may also be constructed. For the situations shown in Figure 1 (a) (b) and (c), there is no natural refinement and the n-polygonal cell can be either refined into n quadrilaterals or n triangles (see Figure 6 as an example). We will focus our discussion on a 2D PEBI cell to illustrate both quadrilateral refinement (QR) and triangular refinement (TR) (Figure 2.6). Instead of seeking a direct interpolation of velocity from the known boundary conditions to every point inside the polygon, the strategy is to divide and conquer by interpolating in each sub-cell separately. The boundary conditions for each sub-cell then have to be constructed from the boundary conditions on the polygon.

Let us consider quadrilateral refinement first. As in our discussion of shape functions, let us suppose each quadrilateral is associated with 8 degrees of freedom

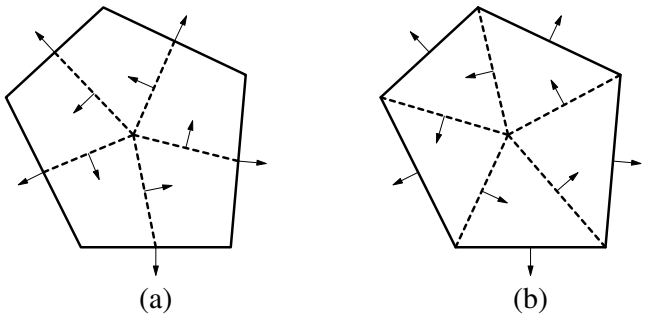

Figure 2.6: Sub-cell refinement with (a) quadrilaterals and (b) triangles. Arrows show the positive flux directions.

in general. Thus there are $8n$ degrees of freedom in the representation. The normal projection of the velocities on the boundary of the polygon are known. This means that for the 2 faces of each quadrilateral which are on the boundary of the polygon, 4 degrees of freedom are specified. Flux continuity across the newly introduced n internal faces will constrain another $2n$ degrees of freedom. Therefore, there are $2n$ degrees of freedom remaining. If we choose to constrain the velocity model to the lowest order, then the variation of the normal velocity on each internal face vanishes, providing n additional constraints and reducing the problem to n degrees of freedom.

For triangular refinement, each triangle has 6 degrees of freedom, with $6n$ degrees of freedom in total. There are 4 degrees specified on the polygon boundary for each triangle. Total flux continuity across the newly introduced internal faces will constrain another n degrees of freedom, reducing the problem to n degrees of freedom.

According to this analysis, only the case of quadrilateral refinement with higher order (BDM_1) internal face fluxes provides $2n$ degrees of freedom. Otherwise, only n degrees of freedom are available. For the schemes with n degrees of freedom, we will show that there is a competition between continuity of the solution and whether the velocity field is locally conservative. The higher order quadrilateral refinement,

with $2n$ degrees of freedom, is able to satisfy both requirements. This is explained in more detail in the remainder of this section.

2.6.1 Local Conservation (LC)

First we will discuss in general the constraints which are imposed by the requirement of local conservation on the remaining degrees of freedom. There is no restriction of our construction to incompressible flow. The total source of the polygonal cell is given by

$$S = \sum_{i=1}^{n} Q_i^e \tag{2.24}$$

where the Q_i^e are the known polygon boundary face fluxes. The positive directions are outwardly directed, as shown in Figure 2.6. Assuming a constant velocity divergence, i.e. local conservation, then the source term for sub-cell i should be

$$s_i = S\frac{(c_t)_i\phi_i A_i}{\sum_{l=1}^{n}(c_t)_l\phi_l A_l} \tag{2.25}$$

where $(c_t)_i$, ϕ_i, and A_i are the total compressibility, the porosity and the area of sub-cell i. Therefore, the conservation residual for each sub-cell is

$$\begin{aligned} R_i = Q_{i+1} - Q_i + Q_{i+1}^{e1} + Q_i^{e2} - s_{i+1} \\ (i = 1, 2, \cdots, n, cyclic) \end{aligned} \tag{2.26}$$

for quadrilateral refinement, and

$$R_i = Q_{i+1} - Q_i + Q_i^e - s_i \quad (i = 1, 2, \cdots, n, cyclic) \tag{2.27}$$

for triangular refinement. The Q_i^{e1} and Q_i^{e2} are the half face fluxes for the ith polygonal boundary face (we have $Q_i^{e1} + Q_i^{e2} = Q_i^e$); the Q_i are the fluxes of the

internal faces whose positive directions are counterclockwise as shown in Figure 2.6. Because $\sum_i R_i = 0$, identically, local conservation provides only $n-1$ independent constraints:

$$R_i = 0 \ (i = 1, 2, \ldots, n-1) \tag{2.28}$$

2.6.2 The Closure Constraint

Local conservation only provides $n-1$ constraints (Equation 2.28). An additional closure constraint is needed in order to complete the solution of the Q_i. There are three existing options to formulate the closure constraint, which will be summarized as follows.

Option 1

This option assumes irrotationality of the velocity field:

$$\nabla \times \mathbf{u} = 0 \tag{2.29}$$

The above equation can be formulated in a weak sense

$$\oint \mathbf{u} \cdot \hat{\mathbf{t}} \, dl = 0 \tag{2.30}$$

The closed loop for the integration is usually chosen to run through the cell and face centers. This option is simple to implement because it does not refer to any rock properties.

Option 2

This option assumes the existence of a local potential function, the pressure P, which means

$$\nabla \times \nabla P = 0 \tag{2.31}$$

In combination with Darcy's Law, this equation can be formulated in a weak sense as

$$\oint \mathbf{u} \cdot \mathbf{K}^{-1} \cdot \hat{\mathbf{t}}\, dl = 0 \tag{2.32}$$

with the same closed loop as before. This was first used by *Cordes and Kinzelbach* (1992) and later by *Prévost et al.* (2001) and often referred to as the "irrotationality" condition in the literature. It reduces to the first option for constant scalar rock permeability. If the heterogeneity or the anisotropy of the permeability is significant, Equation 2.32 should be applied in preference to Equation 2.30.

Option 3

This option, proposed by *Datta-Gupta and King* (2007), is equivalent to a finite difference form of Equation 2.32. It utilizes a local pressure solution, which provides easy extension to 3D and to compressible flow. A similar construction has recently been applied by *Kachuma* (2010) to trace streamlines in non-matching grids across faults. If the principal axes of the permeability tensor are aligned with the sub-grid axes, then a two point flux approximation is adequate. Otherwise a multi-point flux approximation should be considered. Let P_i be the pressure at the center of each sub-cell, and let T_i be the two-point transmissibility between sub-cell i and $i+1$. Then the inner face flux from sub-cell i to $i+1$ is related to the pressure difference according to

$$Q_i = T_i(P_i - P_{i+1}) \tag{2.33}$$

Divide by T_i and sum over i, and the total pressure drop must vanish, which gives

$$\sum_{i=1}^{n} \frac{Q_i}{T_i} = 0 \tag{2.34}$$

Equation 2.34 is used as the final constraint to supplement Equation 2.28.

2.6.3 Higher-order Quadrilateral Refinement, $BDM_1(QR)$

As we have already mentioned, higher order quadrilateral refinement, $\mathrm{BDM}_1(\mathrm{QR})$, with $2n$ degrees of freedom, is able to satisfy local conservation and produce smooth velocity fields at the same time. We will first impose the $n-1$ local conservation constraints discussed in Section 2.6.1 and one closure constraint discussed in Section 2.6.2. The remaining n degrees of freedom can be further reduced to only 2 if we impose a single velocity at the center point, shared by all the sub-quadrilaterals. We calculate this center velocity using one of the CVI schemes discussed in Section 2.5.3, usually Equation 2.23. Like the CVI methods, this scheme provides a smooth interpolation of properties within polygons. Unlike the CVI methods, it produces locally conservative velocity fields, which are advantageous in many applications, as we will show.

This scheme is the best technical solution as it satisfies all of our stated requirements. However, it has two disadvantages. First, it requires numerical calculation of the streamline trajectories. This is in contrast to lower order schemes where the trajectories may be integrated analytically. Second, it imposes a continuous solution when this may not be appropriate. If either the sub-grid boundary conditions or the sub-grid properties are heterogeneous, then the lower order scheme may provide a more physically reasonable solution. For both these reasons, we continue our analysis by examining lower order velocity interpolation schemes.

2.6.4 Lower-order Quadrilateral Refinement, $RT_0(QR)$

As discussed earlier, the lower order schemes, based on the RT_0 basis, imposes a uniform normal velocity across each internal face and thus reduces the problem from $2n$ to n degrees of freedom. If we choose to satisfy the $n-1$ local conservation constraints first, the remaining degree of freedom is not sufficient to provide a smooth

velocity field. Otherwise, if we choose to satisfy continuity of the solution first by imposing a single velocity at the center point shared by all the sub-quadrilaterals, the n degrees of freedom will be reduced to only 2, which are not sufficient to satisfy the $n-1$ local conservation constraints. The competition between the two requirements leads to either a local conservation method or a continuous velocity method as follows.

Local Conservation (LC)

If the polygonal cell properties are only piecewise constant on the sub-quadrilaterals, or if the flux boundary conditions are also heterogeneous, then the requirement of smooth velocities becomes unnecessary. In this case, a lower order scheme is adequate to satisfy local conservation, without constraining the solution to be too smooth. We may also choose to work with a lower order scheme in order to simplify the implementation and increase numerical efficiency. Specifically, if the polygonal boundary flux conditions are themselves of lower order, then utilizing a high order velocity for interpolation shows no advantage in the tests we have performed. Also, use of the RT_0 interpolation in each sub-quadrilateral provides an analytic solution for both streamline trajectory and the time of flight calculation.

We first apply the $n-1$ local conservation constraints. The remaining degree of freedom may be constrained by any of the closure constraints discussed previously in Section 2.6.2. In addition to these three options, we propose an additional option (option 4). The last degree of freedom (e.g. Q_1) can be resolved by minimizing the velocity variance at the center node, i.e., maximizing velocity continuity.

$$\min_{Q_1} \left\{ \sum_{i=1}^{n} \|v_{ci}(Q_1) - \bar{v}_c\|^2 \right\} \tag{2.35}$$

where v_{ci} is the velocity at the center point in the ith sub-cell and $\bar{v}_c$ is the average of these velocities. As with option 1, this is expected to work best on problems with

no sub-cell heterogeneity. For higher order quadrilateral refinement, this residual vanishes, although not for the lower order scheme.

Continuous Velocity (CV)

We impose a single velocity at the center point shared by all the sub-quadrilaterals. This reduces the n degrees of freedom to only 2. The velocity at the center point can then be specified by applying one of the CVI methods (option 1), as was done for higher order quadrilateral refinement. Alternatively, one can construct the center velocity by minimizing the conservation error (option 2), which is expressed as

$$\min_{\mathbf{u}_c} \left\{ \sum_{i=1}^{n} R_i^2 \right\} \tag{2.36}$$

2.6.5 Triangular Refinement, BDM$_1$(TR)

Triangular refinement is based on the BDM_1 basis, but is more tightly constrained by the boundary velocities than quadrilateral refinement, providing only n degrees of freedom. Hence, the analysis of triangular refinement is similar to that of lower order quadrilateral refinement. Therefore, either keep local conservation or the continuous velocity constraint can be applied with triangular refinement, but the satisfaction of both requirements is not possible with triangular refinement.

2.6.6 Summary

At this point we have described a large number of possible interpolation schemes, as summarized in Table 2.1. The four major categories are continuous velocity interpolation (CVI), higher order quadrilateral refinement (BDM_1(QR)), lower order quadrilateral refinement (RT_0(QR)), and triangular refinement (BDM_1(TR)). Additional categories distinguish between local conservation (LC) and continuous velocity

Table 2.1: Descriptions of the velocity interpolation schemes

Schemes	CVI	BDM_1 (QR)	RT_0 (QR,LC)	RT_0 (QR,CV)	BDM_1 (TR,LC)	BDM_1 (TR,CV)
Cell Refinement	None	Quad.	Quad.	Quad.	Tri.	Tri.
Basis	CVI	BDM_1	RT_0	RT_0	BDM_1	BDM_1
Continuous Velocity	Yes	Yes	No	Yes	No	Yes
Local Conservation	No	Yes	Yes	No	Yes	No
# of Options	3	3	4	2	4	2

(CV), and as discussed, each scheme may require specific closure options. We will now test the performance of these schemes against an increasingly complex series of test cases, in the next section.

2.7 Results and Discussions

2.7.1 Single Polygonal Cell

The single polygonal cell used for the test is a regular convex octagon, with incompressible flow coming in from three adjacent boundary faces and going out of the remaining five boundary faces. We will impose uniform (lower order) flux on each face. The flux is 5 for each inflow boundary face, and 3 for each outflow boundary face. The launching points of the streamlines are at the three inflow boundary faces and distributed uniformly.

The three different CVI schemes (see Section 2.5.3) are in this case identical because of the regularity of the test cell. They will generally give slightly different results for irregular convex polygons, but their major difference is in the robustness for degenerate and non-convex polygons, which has already been discussed.

Different options of the closure constraint should produce almost identical results if the cell permeability is a scalar constant. However, if the cell permeability is anisotropic ($k_x \neq k_y$), the anisotropy will contribute to the formulation of options 2

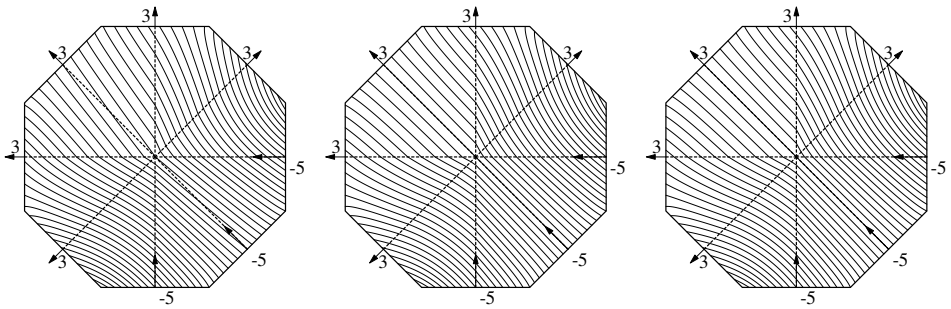

Figure 2.7: The streamline trajectories of the RT_0(QR,LC) with (a) option 3 with $k_y = 10k_x$, (b) option 3 with $k_y = k_x$, (c) option 4.

and 3, but not to options 1 and 4. As an example, Figure 2.7 shows the streamline trajectories using the RT_0(QR,LC) scheme with (a) option 3 with $k_y = 10k_x$, (b) option 3 with $k_y = k_x$, and (c) option 4. Even with strong anisotropy, we see negligible differences between the different closure constraints for these conservative methods. Because of the existence of an underlying stream-function, which is identical on the boundary of the polygon for all of these three cases, the exit point of each trajectory is uniquely specified by its entry point. However, if the cell permeability is not constant, i.e. the sub-cells have strong contrasts in permeability, then the face fluxes will not be uniformly distributed and either option 2 or 3 should be used for velocity reconstruction as then neither velocity irrotationality nor a requirement of velocity continuity would have a physical motivation.

In Figure 2.8 we examine the slightly more complicated case of interpolation on an irregular convex polygon. For the RT_0(QR,CV) method, the two options of interpolating the center point velocity produce only slightly different results. The regular octagon example reveals no difference at all due to its symmetry. Here a non-regular pentagon is used instead to show that these is only a minor difference between

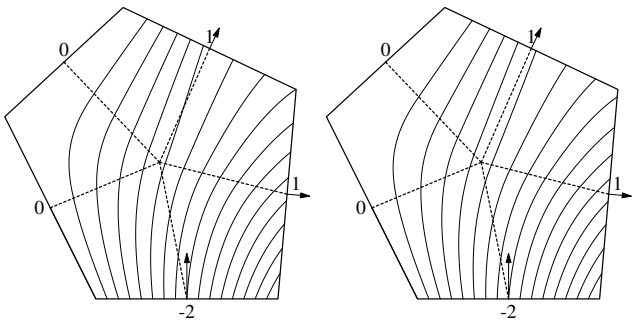

Figure 2.8: The streamline trajectories using the RT_0(QR,CV) scheme in a non-regular pentagon with (a) option 1 and (b) option 2. The arrows and numbers associated indicate the lower order boundary fluxes.

the closure options. However, unlike the conservative schemes, the exit points of the trajectories will now vary for different options of the RT_0(QR,CV) method, and will also differ from the RT_0(QR,LC) exit points. As this deviation will accumulate, we expect less accurate streamline trajectories as we trace across more cells.

In Figure 2.9 we now contrast a wider range of methods. For the locally conservative methods we close the equations using minimum velocity variance (option 4). For the continuous velocity schemes we utilize CVI to determine the center point velocity (option 1). Figure 2.9 shows the streamline trajectories for the methods discussed in this section. The CVI method requires no cell refinement; the continuous velocity and the locally conservative schemes may use either lower order quadrilateral refinement or triangular refinement. The CVI, the BDM_1(QR), the RT_0(QR,CV), and the BDM_1(TR,CV) methods produce smooth streamlines. The RT_0(QR,LC) and the BDM_1(TR,LC) produces streamlines with kinks or refractions at the inner faces due to discontinuous tangential velocities. For the BDM_1(QR), the RT_0(QR,LC), and the BDM_1(TR,LC) methods, which are locally conservative, the

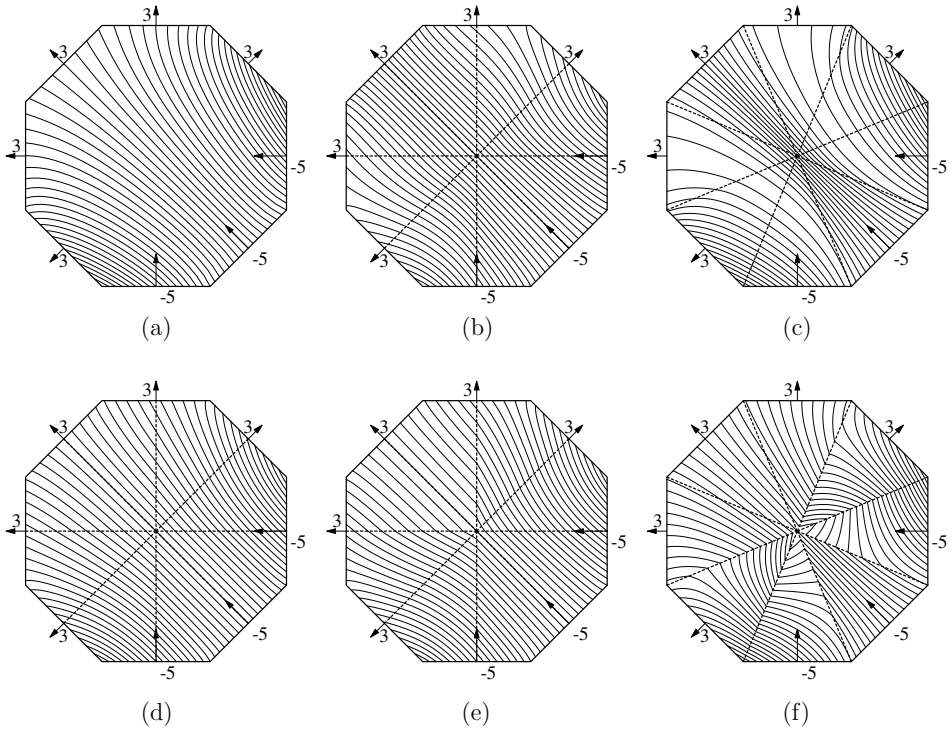

Figure 2.9: Single cell streamline tracing results for (a) CVI, (b) RT_0(QR,CV), (c) BDM_1(TR,CV), (d) BDM_1(QR), (e) RT_0(QR,LC), (f) BDM_1(TR,LC).

streamlines are distributed uniformly on the outflow boundary faces, and their exit points are uniquely determined by the entry points. For the CVI, the RT_0(QR,CV), and the BDM_1(TR,CV) methods, which do not satisfy local conservation, streamlines are distributed erratically and their exit points are not uniquely determined by the entry points.

The consequences of not satisfying local conservation can be illustrated by the example shown in Figure 2.10. The directions of flux on the boundary faces of the quadrilateral are indicated by the thick arrows and the flow rates across the boundary faces are the same Q as shown in Figure 2.10(a). Therefore, there is no net flow coming in or going out of the cell. However, the velocity field calculated by the CVI

method shows negative divergence in the upper region and positive divergence in the lower region separated by the dotted line. Although the integral of the divergence in the entire cell is still zero, locally there are volume sources introduced in the lower region and volume sinks introduced in the upper region. Let us consider a streamtube shown in Figure 2.10(b) in the lower region of the cell starting between points A and B. Because the flux on each boundary face is constant, the streamtube carries a flow rate of $Q/10$ when it enters the cell. But because artificial sources are introduced in the lower region, the streamtube will carry more and more fluid as it passes through the cell, and delivers more than $Q/10$ at the exit boundary between points A' and B'. For incompressible fluid, such a result violates mass balance. Under the same situation, the locally conservative RT_0 velocity interpolation scheme will generate a divergence free velocity field. As shown in Figure 2.10(c), the streamtube starting between the same points A and B will always carry a flow rate of $Q/10$ and the distance between the exit points is exactly one tenth of the boundary length. When tracing streamlines in multiple cells, the error created in a single cell as shown in Figure 2.10(b) may accumulate or cancel in the succession of cells that are penetrated by the streamlines, depending on the specific geometries of those cells. In contrast, in a locally conservative scheme, the flow carried by a streamtube will always be preserved regardless of cell geometries. Looking from the other side of the same problem, if we assume each streamline carries the same amount of flow, then for a non-conservative scheme, the fluxes obtained by counting the number of streamlines passing through each outflow face will be inconsistent with the value specified as the boundary condition.

Another important observation from Figure 2.9 is that quadrilateral refinement and triangular refinement produce quite different results under the same method. Quadrilateral refinement provides systematically more regular results. We believe

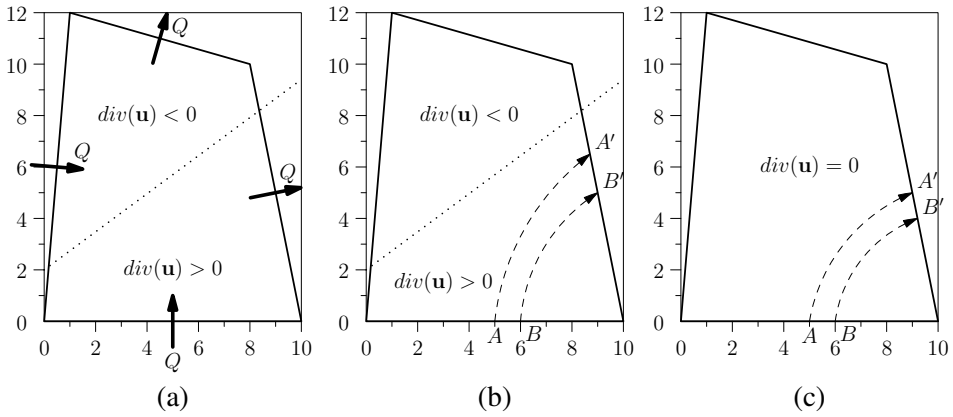

Figure 2.10: (a) The divergence of the velocity field obtained by the CVI method in a quadrilateral is negative in the upper region and positive in the lower region divided by the dotted line. (b) Using the CVI method, a streamtube between streamlines AA' and BB' is shown. The flow rate between AB is $Q/10$, while the flow rate between $A'B'$ is larger than $Q/10$. (c) With the locally conservative RT_0 velocity interpolation, the streamtube starting between AB is shown. The flow rate between the points A' and B' is $Q/10$, which is same as the flow rate entering AB.

that these results are due to the more continuous boundary conditions with quadrilateral refinement, as each adjacent boundary quadrilateral face shares a common boundary flux. In contrast, triangular refinement has no such continuity in boundary conditions, with each triangle having an independent boundary condition with polygonal boundary face. This difference is also reflected in the count of degrees of freedom, as discussed in the beginning of Section 2.6. The triangular refinement constructions have only n degrees of freedom in the interior of the cell, even with higher order boundary conditions on the inner faces. This is why triangular refinement does not have sufficient degrees of freedom to satisfy both local conservation and velocity continuity. BDM_1(QR) is the only method that satisfies both local conservation and velocity continuity. The result of BDM_1(QR) surpasses the other methods in the combined regularity and smoothness of the streamline trajectories.

2.7.2 Quarter 5-Spot Pattern Flood

The 2D quarter 5-spot pattern flood is one of the most frequently used test cases for streamline tracing. We use a PEBI grid of 24 polygonal cells in the unit square with homogeneous rock properties. The injector and the producer are placed at the lower left corner and the upper right corner of the unit square respectively. For this particular case, the face fluxes of all cells can be calculated using the analytic stream-function for the quarter 5-spot (*Datta-Gupta and King*, 2007). Lower order flux boundary conditions are assumed on each cell for all the velocity interpolation methods to be applied.

Figure 2.11 shows the streamline trajectories initiated uniformly from the injector cell with methods corresponding to those used in Figure 2.9. The dashed streamlines are the references obtained from the analytic streamfunction. The results of time of flight are summarized in Table 2.2(a). According to Table 2.2(a), the CVI and BDM_1(TR,CV) methods have better performance. However, the continuous velocity schemes tend to avoid the extremes in velocity, and do not adequately sample the lower velocity portions of the flood pattern, especially in the two stagnation corners. In contrast, the conservation schemes are constrained in such a way as to better sample these regions. To avoid such bias, another set of test results are calculated with the streamlines initiated uniformly from the line connecting the upper left and lower right corners in the domain. This new set of initiation points provides a better match between the calculated and the reference trajectories for all the methods but not to the same degree. The time of flight error analysis is shown in Table 2.2(b). In this case, the RT_0(QR,LC), BDM_1(TR,LC), and CVI methods have better performance.

From these two numerical experiments, we find it difficult to provide a quanti-

Table 2.2: The time of flight results in the homogeneous quarter 5-spot case. Velocity interpolation schemes are compared based on particular streamlines launched from the same points.

(a) Streamlines originated at the injector

Schemes	Ref.	CVI	BDM_1 (QR)	RT_0 (QR,LC)	RT_0 (QR,CV)	BDM_1 (TR,LC)	BDM_1 (TR,CV)
Min TOF (a.u.)	0.6031	0.6015	0.6031	0.6054	0.6174	0.6099	0.6019
Max TOF (a.u.)	1.5288	1.4780	1.7239	1.6828	1.2988	1.6698	1.5428
Avg TOF (a.u.)	0.8480	0.8289	0.9004	0.8992	0.8031	0.9028	0.8408
Avg. TOF Err.%	-	2.26	6.18	6.03	5.30	6.45	0.85

(b) Streamlines originated on a line from upper left to lower right in the domain

Schemes	Ref.	CVI	BDM_1 (QR)	RT_0 (QR,LC)	RT_0 (QR,CV)	BDM_1 (TR,LC)	BDM_1 (TR,CV)
Min TOF (a.u.)	0.6184	0.6114	0.6105	0.6131	0.6169	0.6171	0.6133
Max TOF (a.u.)	2.1662	2.1985	2.2797	2.2282	2.3396	2.2015	2.2045
Avg TOF (a.u.)	1.1327	1.1433	1.1502	1.1397	1.1827	1.1438	1.1588
Avg. TOF Err.%	-	0.93	1.54	0.61	4.42	0.98	2.30

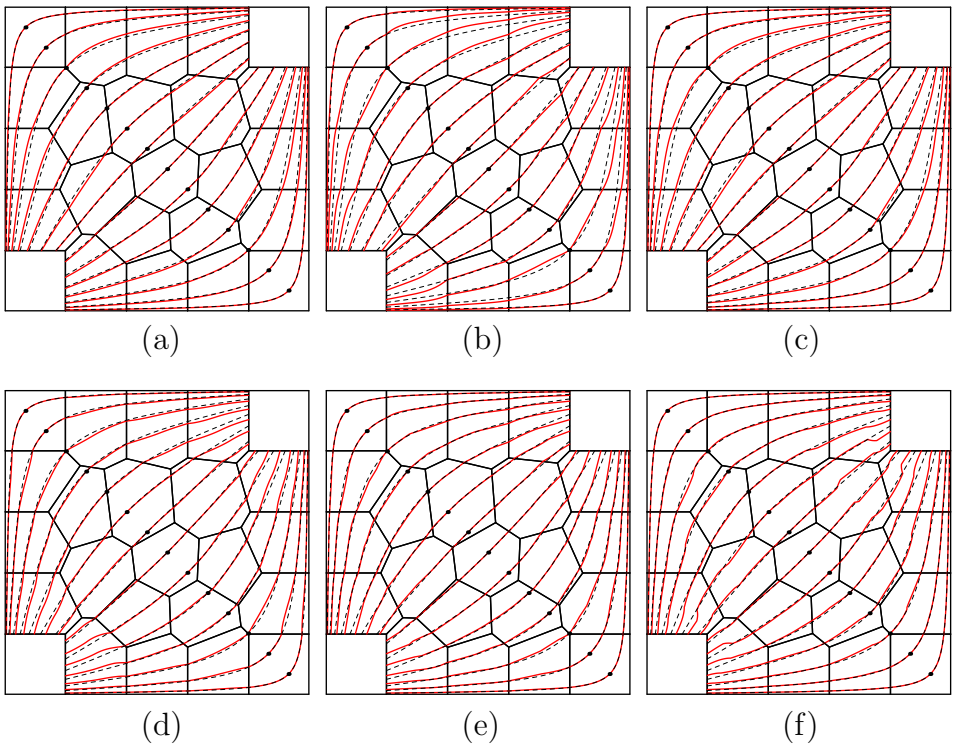

Figure 2.11: Streamline tracing results of the homogeneous quarter 5-spot case. Solid red lines show the streamlines obtained by corresponding methods; dotted black lines show the reference streamlines for comparison. (a) CVI, (b) RT_0(QR,CV), (c) BDM_1(TR,CV), (d) BDM_1(QR), (e) RT_0(QR,LC), (f) BDM_1(TR,LC).

tative comparison for the different schemes by sampling specific streamlines. The results are quite variable depending on the specific points in the domain where the streamlines are initiated. In the comparison of Table 2.2 (a) and (b), we see that the magnitudes of the errors and the ranking between schemes varies depending upon the selection of launching points. Qualitatively, we realize that continuous velocity schemes systematically under-sample the stagnation region compared to the locally conservative schemes, but quantitatively it is difficult to draw conclusions in this fashion. Instead, in order to avoid the bias generated by sampling specific streamlines, we will seek a quantitative error analysis based upon a convergence study of the various schemes.

A less biased "global" error analysis may be obtained by recognizing the relationship between volume, flux and time of flight. This transformation is important in correctly developing the equations for streamline simulation, as without them, mass (or volume) is not conserved. As discussed in *Datta-Gupta and King* (2007), there is a transformation in volume elements between physical space and streamline coordinates

$$\phi \mathrm{d}x\mathrm{d}y\mathrm{d}z = \mathrm{d}\tau\mathrm{d}\psi\mathrm{d}\chi = \mathrm{d}\tau\mathrm{d}Q \tag{2.37}$$

where τ is the time of flight, and ψ and χ are the bi-streamfunctions. This relationship holds for incompressible flow, and may be readily generalized to compressible flow. However, we will use an incompressible test case in the convergence analysis. The volume integral gives

$$\begin{aligned} PV &= \iiint \phi \mathrm{d}x\mathrm{d}y\mathrm{d}z = \iint \tau(\psi,\chi)\mathrm{d}\psi\mathrm{d}\chi = \int \tau \mathrm{d}Q \\ &\approx \sum_{i=1}^{N} \tau_i \Delta Q_i \end{aligned} \tag{2.38}$$

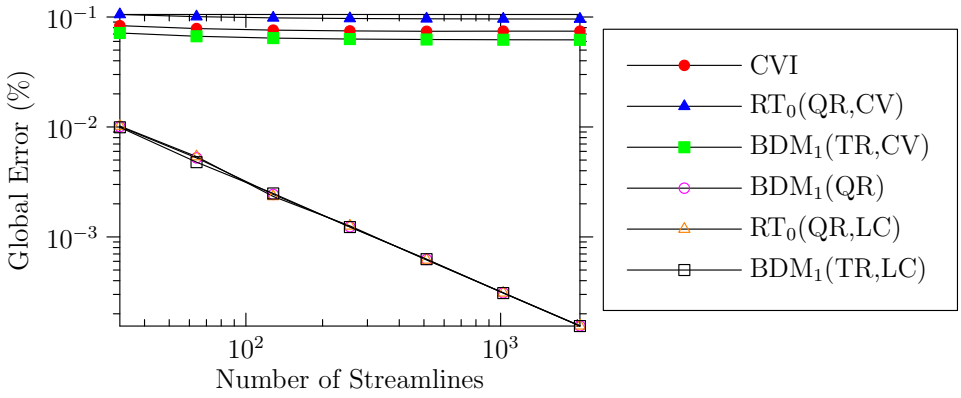

Figure 2.12: Global volumetric error of the homogeneous quarter 5-spot case. The locally conservative schemes demonstrate convergence while the non-conservative schemes do not.

Thus we may evaluate the global volumetric error using

$$E = \frac{\left|\sum_{i=1}^{N} \tau_i \Delta Q_i - PV\right|}{PV} \tag{2.39}$$

Figure 2.12 shows the global volumetric error plotted against the number of streamlines for various methods for the flow patterns shown in Figure 2.11. It is clear to see that the three locally conservative methods converge while the other three methods do not, with an error of approximately 10%. This lack of convergence is a major pitfall of the CVI method and the continuous velocity methods. The global error indicates that the conservative velocity fields are all first order convergent. This is the same order of convergence demonstrated on regular Cartesian grids (*Datta-Gupta and King*, 2007). The order of the convergence is dominated by the low velocity stagnation regions. A local error analysis indicated that the convergence is second order away from such regions, and we would expect the same convergence here on polygons.

The CVI method and the continuous velocity methods produce visually appealing streamline trajectories in Figure 2.11. However, it should be recognized that this is a homogeneous case, for which the underlying analytic solution is smooth. We believe that a high degree of heterogeneity, which is often the case in practical applications, favors the methods which honor local conservation. To illustrate this point, we use the same PEBI grid as in Figure 2.11 but assign a heterogeneous permeability field of 1 md in two cells near the center and 1000 md otherwise (Figure 2.13). Again, we place an injector at the lower left cell and a producer at the upper right cell. Flow equations are solved using the cell-centered finite volume scheme with a two point flux approximation assuming single phase incompressible fluid. Lower order cell boundary fluxes are identical for each calculation, while the streamlines are traced using various velocity interpolation methods. The launching points are uniformly distributed along the two boundary faces of the injector. The calculated streamline trajectories are shown in Figure 2.13. In this case, we encounter nonphysical termination of some streamlines for the CVI method. In addition, the streamline trajectories obtained by CVI and the continuous velocity methods show spurious high concentrations along some streaks as if they were channels, which is purely artificial. In contrast, there is a region near the producer where almost no streamlines are found. This is verified by using as many as 2048 streamlines in the domain. In the discussion of the homogeneous case (Figure 2.11) we pointed out that the continuous velocity schemes tend to under-sample the low velocity stagnation region. In the heterogeneous case, this effect is more apparent since the stagnation regions are on the interior of the domain, as would be the case with all real full field or multi-well applications. Similar failure cases were also shown by *Sun et al.* (2005) for some other non-conservative situations. In contrast, the $\mathrm{BDM}_1(\mathrm{QR})$ and the locally conservative methods are constrained in such a way as to better sample the stag-

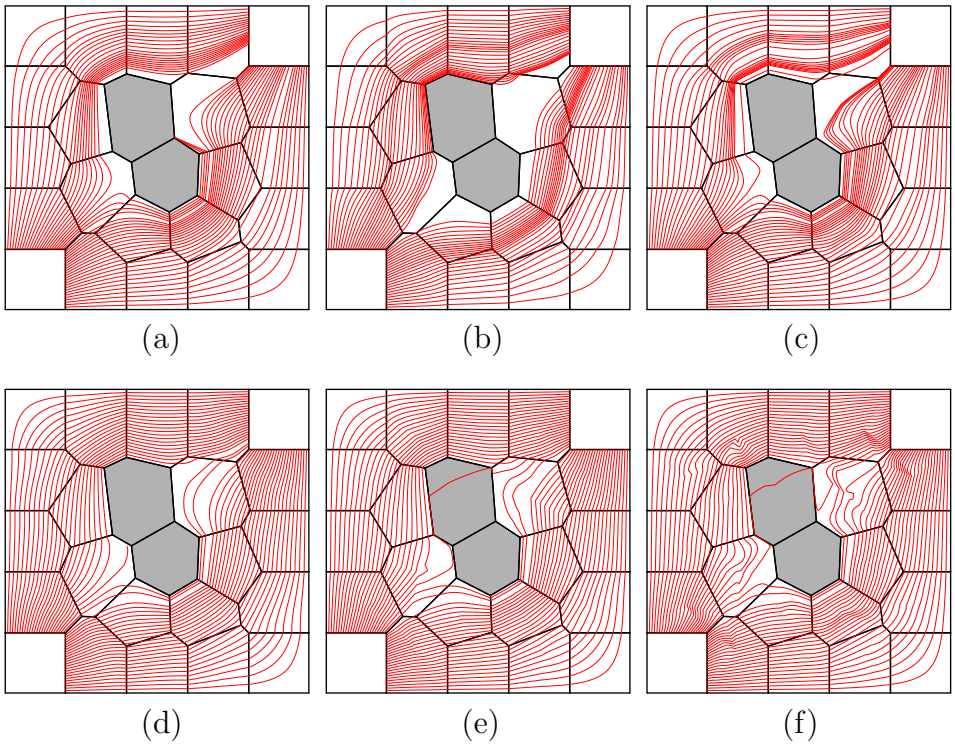

Figure 2.13: Streamline tracing results of the heterogeneous quarter 5-spot case. The permeability of the two cells shaded in grey is 1 md. All other cells have 1000 md permeability. Solid red lines show the streamlines obtained by corresponding methods: (a) CVI, (b) RT_0(QR,CV), (c) BDM_1(TR,CV), (d) BDM_1(QR), (e) RT_0(QR,LC), (f) BDM_1(TR,LC).

nation regions and produce much more reasonable streamline trajectories. Due to local conservation, these methods share the same exit point at the cell boundaries. Their primary difference is in the smoothness of streamline trajectories inside each cell: BDM_1(QR) is the smoothest while BDM_1(TR,LC) is the most tortuous.

Up to now there are no obvious failures displayed for the BDM_1(QR) and the locally conservative methods. Although BDM_1(TR,LC) may produce very tortuous streamlines within a cell, it is still acceptable from a field-level point of view because usually the details of the streamline trajectories inside a cell are not of much concern

for field applications. For these methods, we argue that the major error appears to come from the grid discretization rather than from the velocity interpolation methods. As we have already discussed in section 2.4, the cell boundary flux conditions are obtained by solving the flow equations according to some numerical scheme. A better numerical scheme and/or a better/finer grid will produce a more accurate representation of the boundary fluxes. For the conservative methods, this is the primary factor concerning the accuracy of the interpolated velocity field.

2.7.3 Robustness, Simplicity and Efficiency

Robustness, simplicity, and efficiency should not be overlooked for evaluating various velocity interpolation methods especially for large scale practical applications. Of all the methods presented in this paper, the non-conservative methods show the most issues with robustness, especially as heterogeneity increases. CVI is the most complicated method to implement and the most expensive in term of numerical calculation. The other methods, based on sub-cell refinement, ultimately reduce to simpler tracing problems in quadrilaterals or triangles using either the lower order RT_0 space or the higher order BDM_1 space. The RT_0 space can be analytically integrated leading to simple implementation and numerical efficiency. The BDM_1 space requires the numerical solution of an ordinary differential equation usually by Runge-Kutta integration. It is also necessary to devise a robust and efficient calculation of when a streamline exits from each sub-cell. In contrast, for the RT_0 space, these calculations may be solved analytically. Only if the polygonal cell boundary flux conditions are of higher order and if the sub-cell problem has no heterogeneity, should the BDM_1 space be considered. Even then, using RT_0 with half cell boundary face fluxes, is expected to give a comparable solution, with the efficiency of an analytic solution. In summary, the RT_0(QR,LC) method is our recommended approach.

Since it is based on the RT_0 basis it has the efficiency of an analytic treatment. Because it is conservative, we have none of the issues of robustness experienced by the non-conservative schemes. We will examine a number of applications of the RT_0(QR,LC) scheme in the next section.

2.8 Applications

2.8.1 2D LGR Grids

The 2D cell as shown in Figure 2.1 (b) can be simply considered as a degenerate polygonal cell. Therefore, the methods discussed in this section can be easily applied. As an example, we show a simple quarter 5-spot case with nested LGRs (Figure 2.14). The injector and the producer are located at the lower left corner and the upper right corner respectively. The streamline trajectories shown in the figure are calculated using the LCM with quadrilateral refinement.

2.8.2 3D LGR Grids

It is not trivial to apply the unstructured streamline tracing methods developed in 2D scenarios to 3D LGR grids. Here we follow the approach of *Jimenez et al.* (2010) using a boundary layer approximation, which reduces the 3D problem to a sequence of 2D calculations. As an example, consider a coarse cell with four LGR cells adjacent to one of its faces. The boundary layer for that face is depicted in Figure 2.15, where the thickness of the boundary layer is ε. The boundary layer is within the coarse cell and provides a region in which the uniform flux on the coarse cell face is redistributed to match the individual fluxes coming from each of the refined cell local grid faces. The flux from the coarse cell on the $-x$ side of the boundary layer is allocated proportionally to the area of each fine cell, while the fluxes on the $+x$ side of the boundary layer are known from the fine fluxes obtained for the LGR cells. The only problem still unsolved is how to trace streamlines across

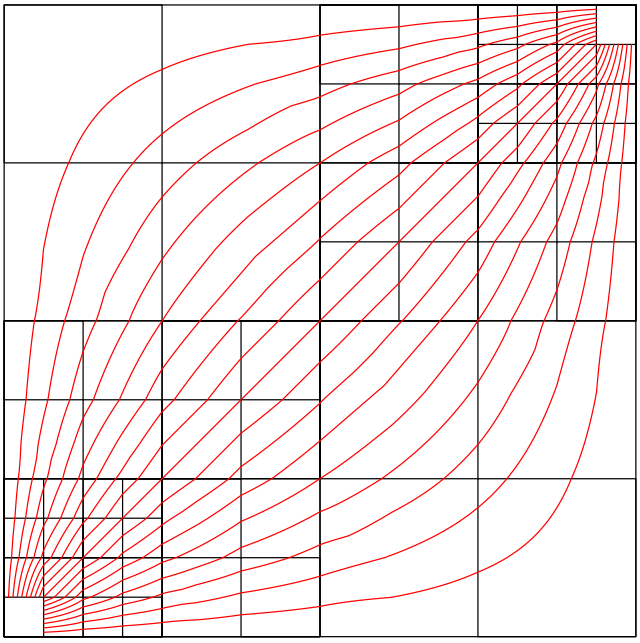

Figure 2.14: Streamline tracing example using the RT_0(QR,LC) method on a grid with local refinement.

this boundary layer. This problem will be simplified if we allow the boundary layer thickness to approach zero, in which case the boundary fluxes in directions other than $-x$ and $+x$ will vanish. The local problem will appear to be that of two dimensional incompressible flow, with heterogeneous source and sink terms, irrespective of the actual fluid properties.

As illustrated in Figure 2.16(a), suppose the total flux through the boundary layer on the coarse cell side is 1, while on the other side, three out of four local fine cell faces have zero flux and the last one has flux 1. If the boundary layer thickness $\varepsilon \to 0$, the situation becomes equivalent to a closed boundary 2D problem as shown in Figure 2.16(b). The differences of fluxes on the $-x$ side and the $+x$ side can be treated equivalently as sources or sinks in the 2D problem for each of the four cells as shown by the red numbers. The next step is to solve this 2D local flow problem.

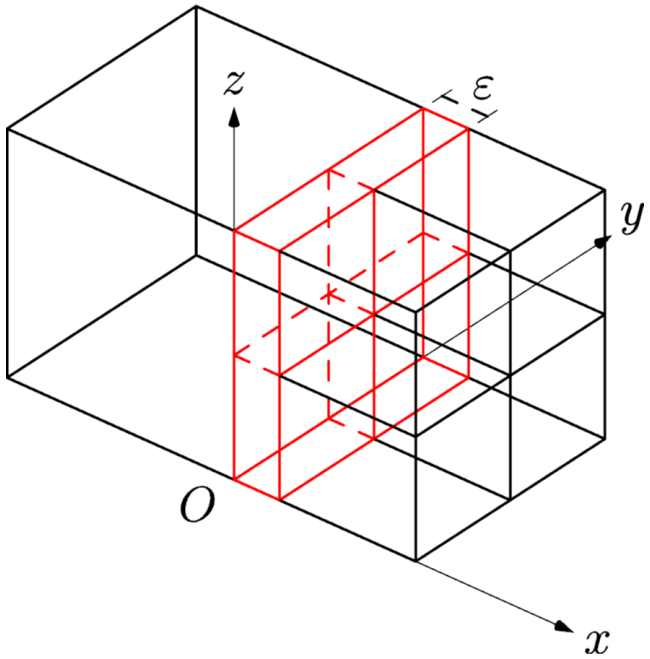

Figure 2.15: A global cell with four LGR cells adjacent to one of its face. The boundary layer is outlined in red.

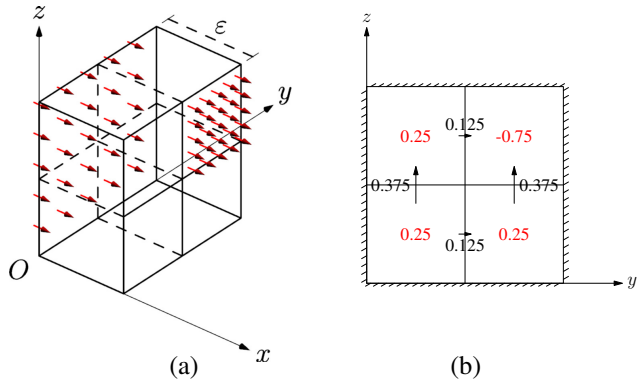

Figure 2.16: (a) Flow rates are shown for the boundary layer. On the $-x$ side the total flux is 1. On the $+x$ side, the fluxes across three LGR faces are zero, and only one LGR face has a flux of 1. All other boundary faces have zero flux. (b) As $\varepsilon \to 0$, the boundary layer reduces to a 2D closed boundary problem. The red number is the equivalent source (positive) or sink (negative) term for each fine 2D cell. The black arrows show the calculated inner face fluxes using the RT_0(QR,LC) method.

The situation of this particular application favors the requirement of local conservation rather than velocity continuity. The reasons are that the boundary flux distribution should be honored rigorously and, the heterogeneity of the refined cell rock properties makes the velocity continuity requirement unnecessary. For tracing within the boundary layer, we require that the integral of the flux associated with the streamlines honor the boundary flux and the exit point of a streamline. Because the detailed path of the streamline is not required, the locally conservative methods with either option 1 or 4 may be applied for simplicity, as these two options do not require information about rock properties. The values and directions of the inner face fluxes are calculated and shown in Figure 2.16(b) with black numbers and arrows. Once the inner face fluxes are determined, streamlines can be traced in the boundary layer by ordinary Pollock interpolation in the unit cube, as shown in Figure 2.17. As the thickness of the boundary layer decreases and finally approaches zero, the traced streamlines ultimately become only slips on the 2D boundary face, which conserve flux on both the coarse cell and the local cell faces. The incremental time of flight in the boundary layer will vanish. The example shows tracing from the coarse side to the fine side of the boundary layer. The reversed trajectories are identical. Once the boundary layer is crossed, tracing can be continued within either a coarse or a fine cell.

2.8.3 Multilateral Well With Nested LGR

The method developed for 3D grids with LGR is applied to a synthetic example which contains a multilateral well. Two-level nested LGR is used near the well in order to reduce the grid size and increase the model resolution of the wellbore trajectories. Figure 2.18(a) and (b) shows the region of LGR and the two branches of the multilateral well. Figure 2.18(c) shows the streamlines for only one of the

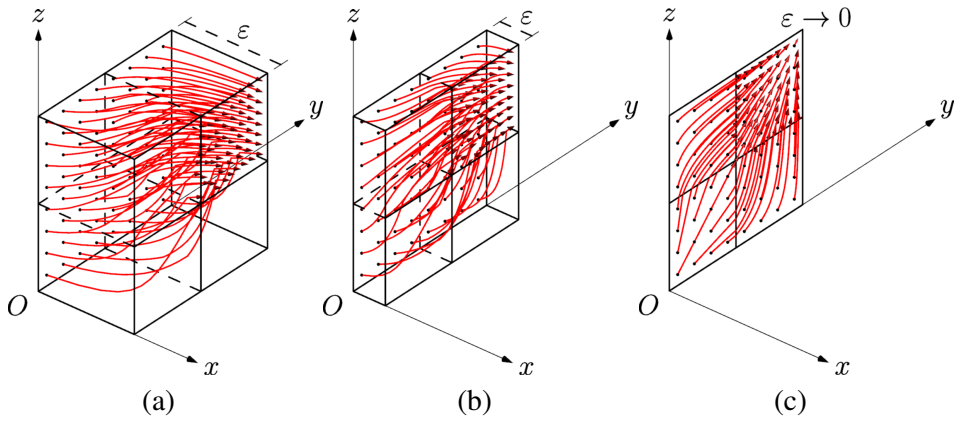

Figure 2.17: Streamline tracing for 3D LGR boundary layer. The thickness of the boundary layer decreases from (a) to (c). In (c) $\varepsilon \to 0$, and thus the streamlines simply slip on the boundary face.

two branches of the multilateral well. Different colors represent streamlines originated from different well completions. Thanks to the higher resolution achieved by the nested LGR, the streamlines we obtained can potentially be used to optimize water flooding efficiency especially in the case of smart completions which enables open/shut-in for each completions individually.

2.8.4 2.5D PEBI Grids

The 2.5D polygonal example shown in Figure 2.19 has one injector and one producer in a three layered reservoir. The grid is refined near the wells. In this example the flow in the k direction is simply treated separately from the i and j directions and the traced streamlines are shown in Figure 2.19. The rock properties within each PEBI cell is a scalar constant and thus the RT_0(QR,LC) method with minimum velocity variance is applied for this application. This pattern flood demonstrates that there is no difficulty in extending the 2D few cell results to larger reservoir models.

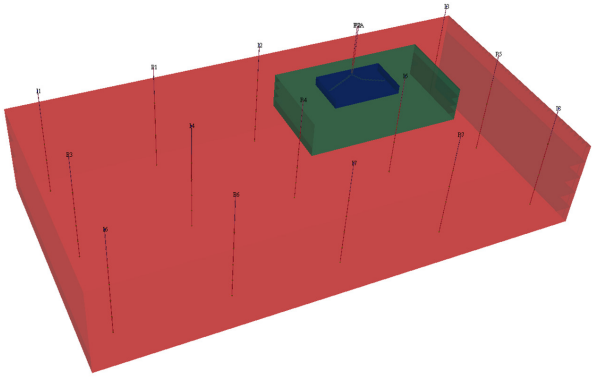

(a)

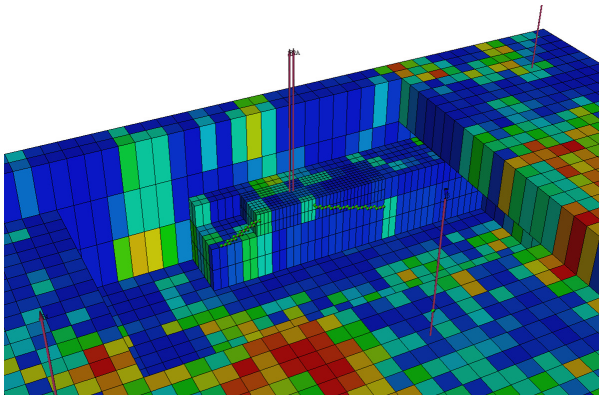

(b)

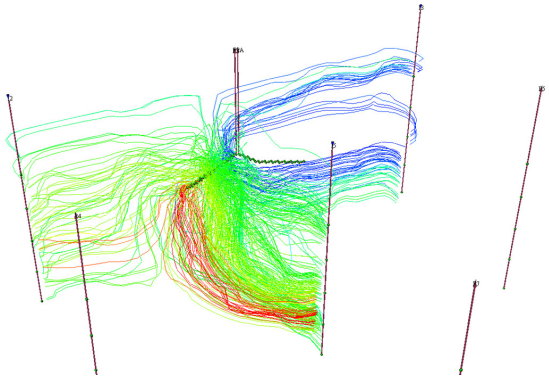

(c)

Figure 2.18: (a) Synthetic reservoir model with one producer having two lateral branches. The green region is the first level of LGR and the blue region is the second level of LGR. (b) Close view near the multilateral well showing the two levels of LGR and the wellbore trajectories. (c) Streamlines for only one of the two branches of the multilateral well. Different colors represent streamlines originated from different well completions.

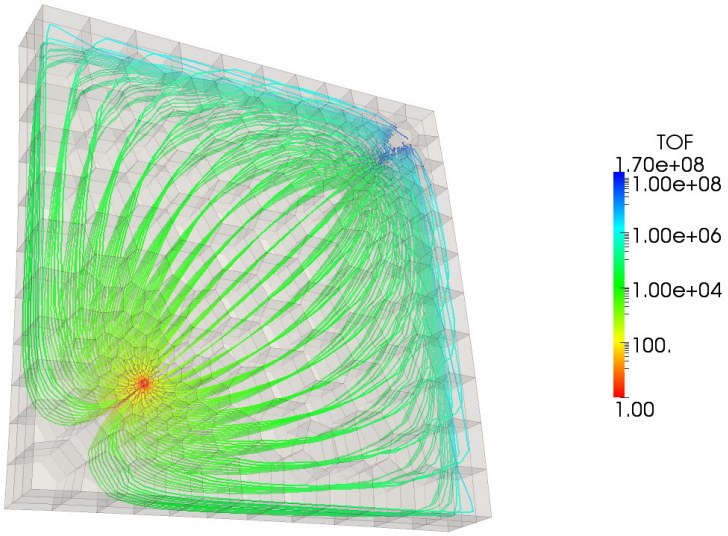

Figure 2.19: Streamline tracing example using the RT_0(QR,LC) method in a 3 layer 2.5D PEBI grid.

2.9 Conclusions

We have presented a comprehensive study of the velocity interpolation methods in n-polygons. These methods are often used as post-processing after the cell boundary fluxes are calculated for numerical schemes that do not directly calculate the velocity field, such as the FV schemes.

We have discussed the relationship between the CVI and the BDM_1 velocity interpolation spaces. Both provide $2n$ degrees of freedom in general n-polygons, but the BDM_1 scheme includes additional higher order terms to honor mass conservation. We have described three versions of the CVI method in n-polygons. Their major difference concerns robustness when dealing with non-convex and degenerate polygons. Based on the technique of isoparametric mapping, the version we propose is the only one that is robust for both non-convex and degenerate polygons. Al-

though it is rather straight-forward to extend the CVI space to n-polygons, a direct extension of the locally conservative BDM_1 space to n-polygons seems difficult, and has not been demonstrated.

Sub-cell refinement, using either quadrilaterals or triangles, provides an effective way to simplify the problem. Local conservation or velocity continuity or both may be used as constraints on the degrees of freedom introduced inside the n-polygonal cell. Only the higher order BDM_1(QR) method satisfies both requirements. The BDM_1(QR) method can be viewed as an indirect extension of the BDM_1 space to n-polygons.

Numerical experiments have provided strong evidence of the necessity of local conservation for a velocity interpolation method to produce robust physical results. An error analysis of comparing particular streamlines with the "true" streamlines are shown to be ambiguous in nature. Instead, a global volumetric error analysis shows that only the locally conservative schemes are convergent. Moreover, the heterogeneous quarter 5-spot case demonstrates failure modes for both the CVI and the continuous velocity methods.

The primary difference between the locally conservative methods is the smoothness of streamline trajectories inside each cell, and in their numerical efficiency. BDM_1(QR) is the smoothest while BDM_1(TR,LC) with triangular refinement is the most tortuous. RT_0(QR,LC) utilizes the RT_0 basis and has an analytic solution for the streamline trajectories while both BDM_1(QR) and BDM_1(TR,LC) utilize the more expensive BDM_1 basis. Therefore, robustness, simplicity and numerical efficiency seem to be decisive factors in term of looking for the best method to be applied in large scale field applications. In summary, we would only consider the BDM_1(QR) method for constant sub-cell permeability and high order cell boundary flux conditions, but even then, a piecewise implementation of RT_0(QR,LC) may be more than

adequate; otherwise we recommend the RT_0(QR,LC) method, which is robust, easy to implement, and highly efficient. The option for closing the locally conservative methods may be selected based on how much sub-cell constitutive information is available and how much effort is deemed to be worthwhile in incorporating sub-cell heterogeneity information.

3. FAST-MARCHING METHODS FOR COMPLEX GRIDS AND ANISOTROPIC PERMEABILITIES: APPLICATION IN UNCONVENTIONAL RESERVOIRS*

3.1 Synopsis

Unconventional reservoirs are characterized by sufficiently low permeabilities so that the pressure depletion from a producing well may not propagate far from the well during the life of a development. This is in contrast to conventional plays where the pressure transients may probe the entire reservoir in weeks to months. The concept of depth of investigation and its application to unconventional reservoirs provide the understanding necessary to describe and optimize the interaction between complex multi-stage fractured wells, reservoir heterogeneity, drainage volumes, pressure depletion, well rates, and the estimated ultimate recovery.

Previous studies have performed unconventional reservoir analysis using more conventional reservoir simulation techniques. High resolution local PEBI grids and global corner point grids have been used to represent complex fracture geometry and conductivity and estimate subsequent well performance. However, these techniques do not provide the more geometric understanding provided by the depth of investigation and drainage volumes. The application of the depth of investigation to heterogeneous reservoirs can be obtained from an asymptotic expansion of the diffusivity equation leading to the Eikonal equation which describes the propagation of the pressure front. This equation is solved using a Fast Marching Method to cal-

*Part of this section is reproduced with permission from "Extension of Fast-Marching Methods to Corner Point and Unstructured Simulation Grids for Optimization of Unconventional Reservoir Developments" by M.J. King, Y. Zhang, A. Datta-Gupta, paper SPE 163637 presented at SPE Reservoir Simulation Symposium held in The Woodlands, Texas, USA, February 18-20, 2013. Copyright 2013 by Society of Petroleum Engineers.

culate a diffusive time of flight at every location within the domain. The diffusive time of flight is directly related to pressure front propagation. Unlike in a reservoir simulator, this frontal propagation is determined in a single non-iterative calculation, which is extremely fast.

In the current study, we extend the Fast Marching Method for solution of the Eikonal equation to complex simulation grids including corner point and unstructured grids. This allows the rapid approximation of reservoir simulation results without the need for flow simulation, and also provides the time-evolution of the well drainage volume for visualization. Understanding the drainage volume alone is useful for well spacing and multi-stage fracture spacing optimization. Additional potential applications include well trajectory and hydraulic fracture location optimization, reservoir model screening and ranking, matrix/fracture parameter estimation, uncertainty analysis and production data integration.

3.2 Introduction

Unconventional resources such as shale gas have taken a significant share in the energy supply in the US and the world energy market (*Holdich*, 2010). The advent and growth of the development of these resources have been driven largely by the advances in technologies such as horizontal well drilling and multistage hydraulic fracturing. However, engineers today still face great challenges in understanding the fundamental mechanisms involved in the production of unconventional reservoirs, from the pore scale to the field scale. Further technology advancement in this area will enable the industry to optimize the unconventional reservoir development by bringing down costs, minimizing risks, and increasing production.

Several recent studies have performed unconventional reservoir analysis using more conventional reservoir simulation techniques (*Cipolla et al.*, 2009, 2011a,b, 2012;

Fan et al., 2010; *Freeman et al.*, 2010). The advantage of using the traditional numerical simulation is that it can rigorously account for complex fracture geometry, reservoir heterogeneity, rock compaction, pressure dependence of reservoir fluid properties, gas absorption effects, and many other physical processes. The disadvantage is that such numerical simulation can be very time consuming, particularly when the high levels of grid refinement are used to accurately model complex fracture geometry, flow in the vicinity of the hydraulic fractures, and interaction with natural fracture networks. Because of uncertainties usually encountered in the development of unconventional reservoirs, building and calibrating such detailed numerical models can be difficult and time consuming.

Another approach more frequently applied in practice is the use of various analytical techniques, including the decline curve analysis (*Fetkovich*, 1980; *Valko and Lee*, 2010) and the pressure/rate transient analysis (*Ilk et al.*, 2010; *Song and Ehlig-Economides*, 2011; *Clarkson et al.*, 2012). The decline curve analysis is often used for production forecasts and reserves estimation. The predictive power relies heavily on the quantity and quality of completion and production data in a particular field as well as the experience gathered during the field development. There is no physical model associated with the decline curve analysis. The pressure/rate transient analysis incorporates simplified completion and reservoir models, such as homogeneous reservoir with fully-penetrated, equally-spaced, symmetric rectangular and planer hydraulic fractures. A small number of model parameters, e.g. fracture permeability and fracture half length, can easily be calibrated from the observed flow regimes and then well production can be predicted based on the calibrated model. These techniques are very useful especially when there is very limited subsurface information. However, the analytical models become inadequate when we have a better understanding of the reservoir heterogeneity and the complex hydraulic fracture geometry

through integration of geological, geophysical, and engineering data.

We propose a novel approach based on the fast marching methods (FMM) for unconventional reservoir analysis (*Datta-Gupta et al.*, 2011; *Xie et al.*, 2012a,b; *Sethian*, 1996). Our proposed approach stands midway between the two approaches discussed above, i.e. conventional numerical simulation and simplified analytical models. As the development of a particular field progresses, more and more data is brought in and the reservoir analysis also needs to evolve from purely analytical in the early stages to full-field numerical simulation in a mature stage. The FMM approach may serves as a bridge for this transition and a screening tool to select models for the more expensive traditional reservoir simulation. There are two characteristics of the FMM approach that make it well suited for such a purpose. First, the FMM approach is extremely fast. A million-cell model can be simulated in minutes. Second, it is a numerical model capable of handling the same degree of geometrical complexity and reservoir heterogeneity as in traditional reservoir simulation. Previous studies by *Datta-Gupta et al.* (2011) and *Xie et al.* (2012a,b) have demonstrated the speed of the FMM approach and how it can provide the understanding necessary to describe and optimize the interaction between complex multi-stage fractured wells, reservoir heterogeneity, drainage volumes, pressure depletion, well rates, and the estimated ultimate recovery. However, these applications are restricted to regular square grid and isotropic permeabilities. The scope of this section is to extend the FMM approach to complex grids and anisotropic permeabilities.

This section is structured as follows. First, we will introduce the background including the Eikonal equation and the basic theory of the fast marching methods. In the methodology section, we will derive the formulation and discretization of the Eikonal equation in corner point grids with anisotropic permeabilities. Next, we will discuss the causality issue. In this discussion smoothly varying medium and non-

smoothly varying medium are dealt with separately. Finally, we will show the results and the applications of the fast marching methods in unconventional reservoirs.

3.3 Background

Unconventional reservoirs are characterized by sufficiently low permeabilities such that the pressure depletion from a producing well may not propagate far from the well during the life of the development. This is in contrast to conventional plays, where the pressure transients may probe the entire reservoir in weeks to months. As a result, the concept of depth of investigation, and its application to heterogeneous reservoirs (*Datta-Gupta et al.*, 2011), is now not just important for traditional well test analysis. Instead, it becomes an important parameter to characterize the production of unconventional wells, since the boundary effects may never be seen during the lifetime of a well and all production may be obtained during the transient flow regime. The traditional depth of investigation for homogeneous reservoir has already been discussed in Section 1.1.3. In the presence of reservoir heterogeneity, *Vasco et al.* (2000) and *Kulkarni et al.* (2000) derived the Eikonal equation for the pressure front propagation and introduced the concept of the diffusive time of flight using the asymptotic ray theory from geometric optics and seismology. Similar concept was developed earlier in the context of diffusive electromagnetic imaging by *Virieux et al.* (1994). By applying asymptotic expansion to the diffusivity equation, it can be shown that in the high frequency limit the pressure front propagation in an isotropic medium can be described by the Eikonal equation (see Section 1.1.2 for details)

$$\sqrt{\alpha}\|\nabla\tau(\vec{x})\| = 1 \tag{3.1}$$

In this equation, the unknown $\tau(x)$ is called the diffusive time of flight. Along a ray path, τ can be calculated from the following integral

$$\tau(r) = \int_0^r \frac{1}{\sqrt{\alpha}} dr' \tag{3.2}$$

The ray path should satisfy Fermat's principle, which means that it is the one which minimizes the line integral of τ (*Sun and Fomel*, 1998). For the purpose of characterizing the pressure front propagation, τ is conceptually a measure of distance rather than time and is analogous to r in Equation 1.19. In fact, the contours of τ are related to the propagation time t of the pressure front through the following equation (*Vasco et al.*, 2000; *Kim et al.*, 2009):

$$\tau = \sqrt{\beta t} \tag{3.3}$$

The reservoir heterogeneity is embedded in the variable τ. It must be pointed out that by extending Equation 1.19 to Equation 3.3 we bring reservoir heterogeneity into the picture, but we lost the exact meaning of the factor β. In a heterogeneous case, there is no global flow pattern any more, and thus, β should be understood in an averaged sense and is related to the geometry of the pressure front which can be of arbitrary shape and changing with time. This will be addressed by future research.

Fast marching method can be used to efficiently solve Equation 3.1 to compute the pressure front propagation. It is a single-pass method which utilizes the fact that the value of $\tau(\vec{x})$ for the first-order PDE depends only on the value of τ along the characteristic(s) passing through the point $\vec{x}$ (*Sethian*, 1996). Thus, the solution of τ can be constructed in an orderly one-pass fashion from smaller values of τ to larger values. The basic framework of fast marching method comprises the following steps

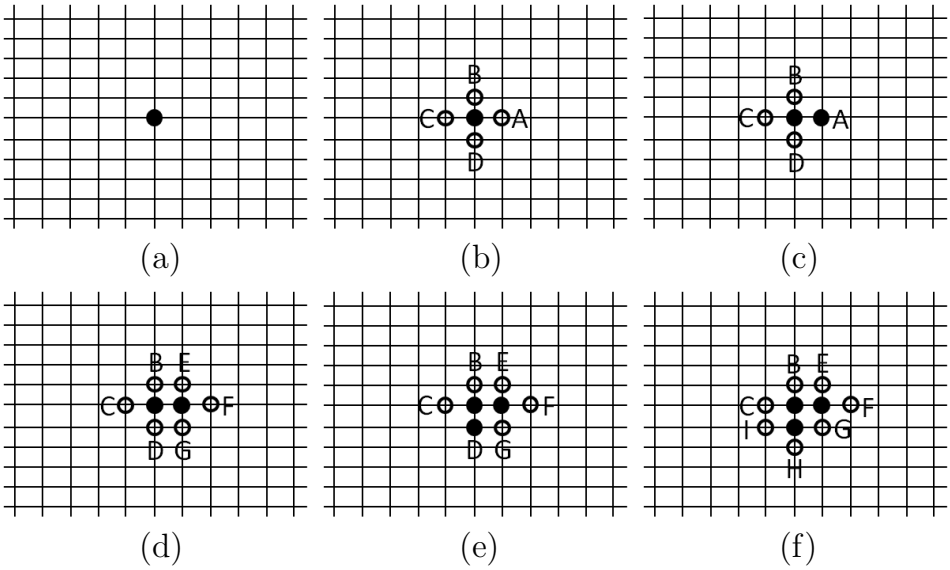

Figure 3.1: Illustration of FMM in 5-stencil Cartesian grid (*Xie et al.*, 2012a).

(*Sethian*, 1999b):

1. Label all grid nodes as *unknown*;

2. Assign τ values (usually zero) to the nodes corresponding to the initial position of the propagating front and label them as *accepted*;

3. For each node that is *accepted*, locate its immediate neighboring nodes that are *unknown* and label them as *considered*;

4. For each node labelled *considered*, update its τ value based on its accepted neighbors using the minimum of local solutions of Equation 3.1 discussed later;

5. Once all nodes labelled *considered* have been locally updated, we pick the node which has the minimum τ value among them and label it as *accepted*;

6. Go to step 3 until all nodes are *accepted*.

In a 5-stencil Cartesian grid, these steps can be illustrated in Figure 3.1. We put one point as the initial position of the propagating front and label it as accepted (solid) as shown in (a). Then its immediate neighbors A, B, C, and D are marked as considered (circle) as shown in (b). After the τ values of A, B, C and D have been updated, we pick the smallest one (suppose it is A) and mark it as accepted as shown in (c). Then its neighbors E, G and F are added into the considered as shown in (d). These steps will repeat for the next accepted point (suppose it is D) as shown in (e) and (f). Local update of τ value using Equation 3.1 for the 5-stencil Cartesian grid can be written with the standard finite difference notation as (*Sethian*, 1996):

$$\max\left(D_{ij}^{-x}\tau, -D_{ij}^{+x}\tau, 0\right)^2 + \max\left(D_{ij}^{-y}\tau, -D_{ij}^{+y}\tau, 0\right)^2 = \frac{1}{\alpha} \tag{3.4}$$

Here the standard finite difference operator D for $\pm x$ directions can be written as $D_{ij}^{-x} = (\tau_{i,j} - \tau_{i-1,j})/\Delta x$ and $D_{ij}^{+x} = (\tau_{i+1,j} - \tau_{i,j})/\Delta x$. Similar equations hold for $\pm y$ directions. In Equation 3.4, τ values at unknown points are regarded as infinity and the "max" function is used to guarantee the "upwind" criteria. Equation 3.4 leads to a quadratic equation and its maximum positive root gives the τ value at point (i, j). Alternatively, we can calculate τ values from each of the four quadrants (bottom-left, bottom-right, top-left, and top-right) by ordinary finite difference formulation and then take the minimum τ value obtained.

3.4 Methodology

Equation 3.1 describes an isotropic case, in which the speed of the front propagation only depends on the location with isotropic permeability distribution. For more general front propagation problems, the front propagation speed will also depend on the direction in which the front is travelling. For anisotropic permeability, the Eikonal equation can be written using the permeability tensor $\bar{\bar{k}}$ as (*Datta-Gupta*

and King, 2007):

$$\vec{\nabla}\tau(\vec{x}) \cdot \bar{\bar{k}} \cdot \vec{\nabla}\tau(\vec{x}) = \phi\mu c_t \tag{3.5}$$

In this section, we will discuss the solution of Equation 3.5 in corner point grids.

Corner point grids are widely used in reservoir simulation due to its flexibility in conforming to the geologic structures and horizons (*Ponting*, 1989). The equations which describe the corner point cell geometry and associated tangent and normal vectors are given in the Appendix A for reference. In analogy to the derivation of flow equations in corner point cells, we perform the isoparametric mapping as discussed in Appendix A. If we assume that the principle directions of the permeability tensor are aligned with the cell edges (tangent vectors), following the derivation in Appendix A, Equation 3.5 can be written in the following form

$$\sum_{i=1}^{3} \frac{k_i}{t_i^2} \left(\frac{\partial \tau}{\partial \hat{x}_i} \right)^2 = \phi\mu c_t \tag{3.6}$$

Here k_i and t_i are the permeabilities and length of tangent vectors in I, J, and K directions. The gradient of τ in Equation 3.6 is now taken in the unit cube under the reference coordinate variables $\hat{x}_i$.

For discretization of Equation 3.6, we will assume that the distortion of the corner point grid is locally mild, so that we can simply use the tangent vector at the center of the cell as an approximation. Here we choose the 5-stencil scheme (or 7-stencil scheme for 3D) for discretization. Extensions to more complicated 9-stencil scheme (or 27-stencil scheme for 3D) can also be used (see later discussion of unstructured grid). Because the rock properties are usually associated with cells in reservoir models, the pressure front propagation speed will change between two cell centers where the τ values are to be calculated. In analogy to transmissibility calculations

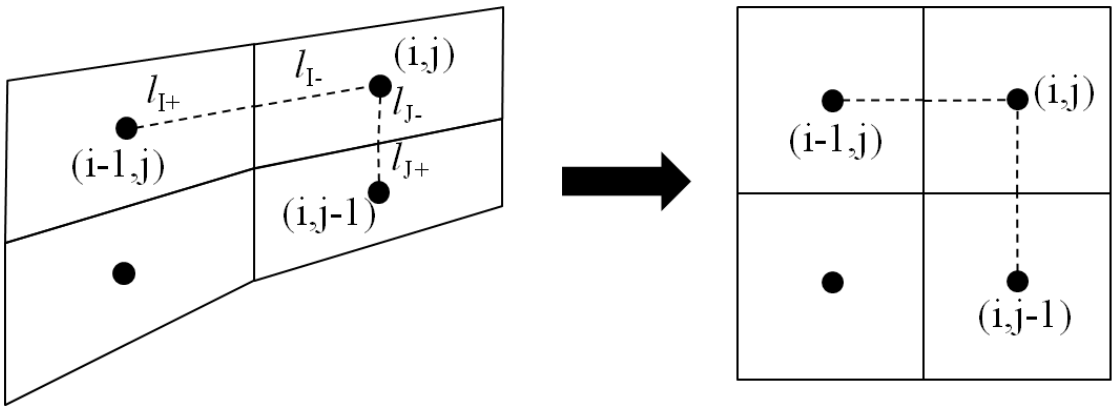

Figure 3.2: 2D example of corner point grid isoparametric mapping and discretization for Equation 3.5.

for solving flow equations, we combine properties from the two half cells to get an average speed for pressure front in each principle direction I, J or K. Figure 3.2 shows an example of 2D isoparametric mapping and the lower left quarter for cell (i, j) in the 5-stencil scheme. The discretization of Equation 3.6 can be written for this case as

$$\frac{(\tau_{i,j} - \tau_{i-1,j})^2}{s_I^2} + \frac{(\tau_{i,j} - \tau_{i,j-1})^2}{s_J^2} = 1 \tag{3.7}$$

where s_I and s_J are the average "slowness" (inverse to pressure front propagation speed) in the reference grid

$$S_I = \frac{l_{I+}(i-1,j)}{\sqrt{\alpha_I(i-1,j)}} + \frac{l_{I-}(i,j)}{\sqrt{\alpha_I(i,j)}} \tag{3.8}$$

$$S_J = \frac{l_{J+}(i,j-1)}{\sqrt{\alpha_J(i,j-1)}} + \frac{l_{J-}(i,j)}{\sqrt{\alpha_J(i,j)}} \tag{3.9}$$

Here α_I and α_J are diffusivity in I and J directions respectively. l_{I+}, l_{I-}, l_{J+}, and l_{J-} are distances from cell centers to face centers as illustrated in Figure 3.2. The same local solution has to be performed for the same cell (i, j) based on the other

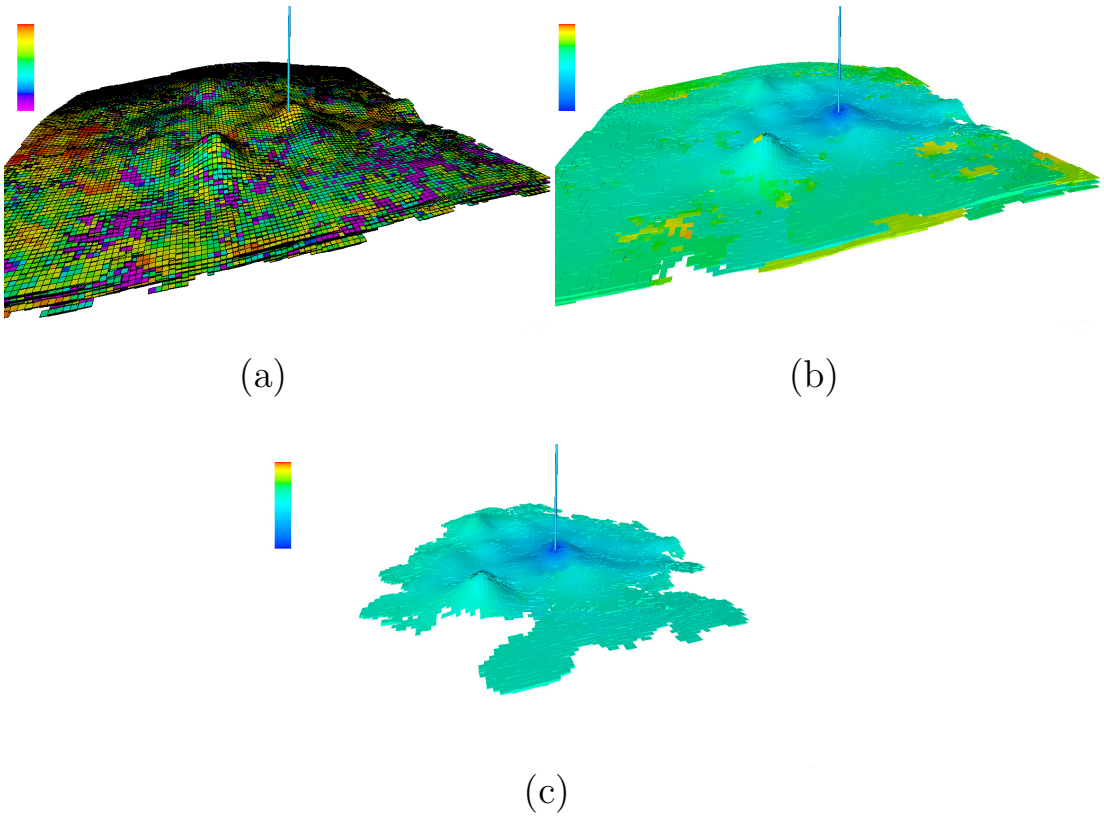

Figure 3.3: Synthetic example showing fast marching method in corner point grid. (a) Permeability field in a synthetic reservoir model with a single vertical well. (b) Calculated diffusive time of flight (cells with infinity values are not shown). (c) Cells with the diffusive time of flight smaller than a specified cut-off value showing the shape of the drainage volume at a particular time.

three pairs of neighbors and then the smallest τ value obtained from these solutions should be used as the updated value for cell (i, j). Extension of Equations 3.7, 3.8 and 3.9 to 3D are straightforward and eight local solutions need to be performed for each cell.

For illustration purposes, Figure 3.3 shows application in a 3D corner point grid. Figure 3.3(a) shows a heterogeneous permeability field with a vertical well. Figure 3.3(b) shows the calculated diffusive time of flight. Figure 3.3(c) shows the cells with diffusive time of flight smaller than a specified cutoff value. The diffusive time of

flight can be related to physical time using Equation 3.3. Then, the results in Figure 3.3(c) will approximate the drainage volume at that time.

3.5 Causality Issue

3.5.1 Smoothly Varying Medium

To motivate our work, we discuss here why the isotropic fast marching method will not produce acceptable results for general anisotropic cases. Figure 3.4 shows one simple 2D example to illustrate this point for a monotonically outward propagating front from a point source using the isotropic fast marching method in a 5-stencil square grid. Figure 3.4(a) shows the solution for an isotropic case. Figure 3.4(b) shows the solution for an anisotropic case with the major axis of anisotropy 45 degrees counterclockwise to the x axis. The solution for the anisotropic case is clearly not acceptable. The correct solution for the front propagation is shown in Figure 3.4(c) and will be discussed later. The reason for the incorrect solution is the violation of the so-called "causality condition"(*Sethian and Vladimirsky*, 2001) as illustrated by Figure 3.5. The τ value at C is to be updated from its immediate neighbors A and B only if the angle ACB contains the characteristic direction $\vec{\xi}$. In Figure 3.5, solid dots represent points that have been accepted and circles represent points that have not been accepted. For isotropic case as shown in Figure 3.5(a), because the gradient direction $\nabla\tau$ is always aligned with the characteristic direction $\vec{\xi}$ and lies within the angle ACB, both the τ values at A and B have already been accepted before the τ value at C is calculated. The causality condition ($\tau_A < \tau_C$ and $\tau_B < \tau_C$) is always satisfied ensuring a good approximation of the characteristic direction and an accurate estimation of the τ value at C. For anisotropic cases in general, the gradient direction is not the same as the characteristic direction as illustrated by Figure 3.5(b). Figure 3.5(c) shows a possible "bad case" where the characteristic

direction and the gradient direction do not lie in the same cell. In this case, the τ value at point B has not yet been accepted before the calculation of the τ value at point C. In another word, we have $\tau_B > \tau_C$, which does not satisfy the causality condition. Therefore, the characteristic direction can only be estimated as from A to C, which is far from the true characteristic direction. Following this estimated characteristic direction, the updated τ value at point C will be inaccurate. Moreover, this error will accumulate as the front propagates. Figure 3.5(d) shows a possible "good case" where the characteristic direction and the the gradient direction are in the same cell. This case is similar to Figure 3.5(a) in that both the τ values at A and B have already been accepted before the τ value at C is calculated. From these examples the causality condition can be generalized as follows: *at a certain node the line extending backwards along the characteristic direction must be enclosed by two neighboring nodes which have already been accepted* (*Sethian and Vladimirsky*, 2000). Because the characteristic direction and the gradient direction are not known beforehand, we need to deal with the possible "bad case" for general anisotropic situations.

There are two approaches to deal with this issue. One approach, known as the expanded neighborhood method, was proposed by *Sethian and Vladimirsky* (2000). The basic idea of the expanded neighborhood method is to enlarge the neighborhood which supports the calculation of τ value for a particular point. For example, in Figure 3.5(c) if we enlarge the neighborhood by including point B', then the local triangle $AB'C$ which contains the characteristic direction will have two accepted points enclosing the characteristic direction available for the calculation of τ value at C and produce acceptable results. The size of the neighborhood required to always produce acceptable results is bounded and its relation to the anisotropy ratio is given by *Sethian and Vladimirsky* (2001). The other approach, which is called

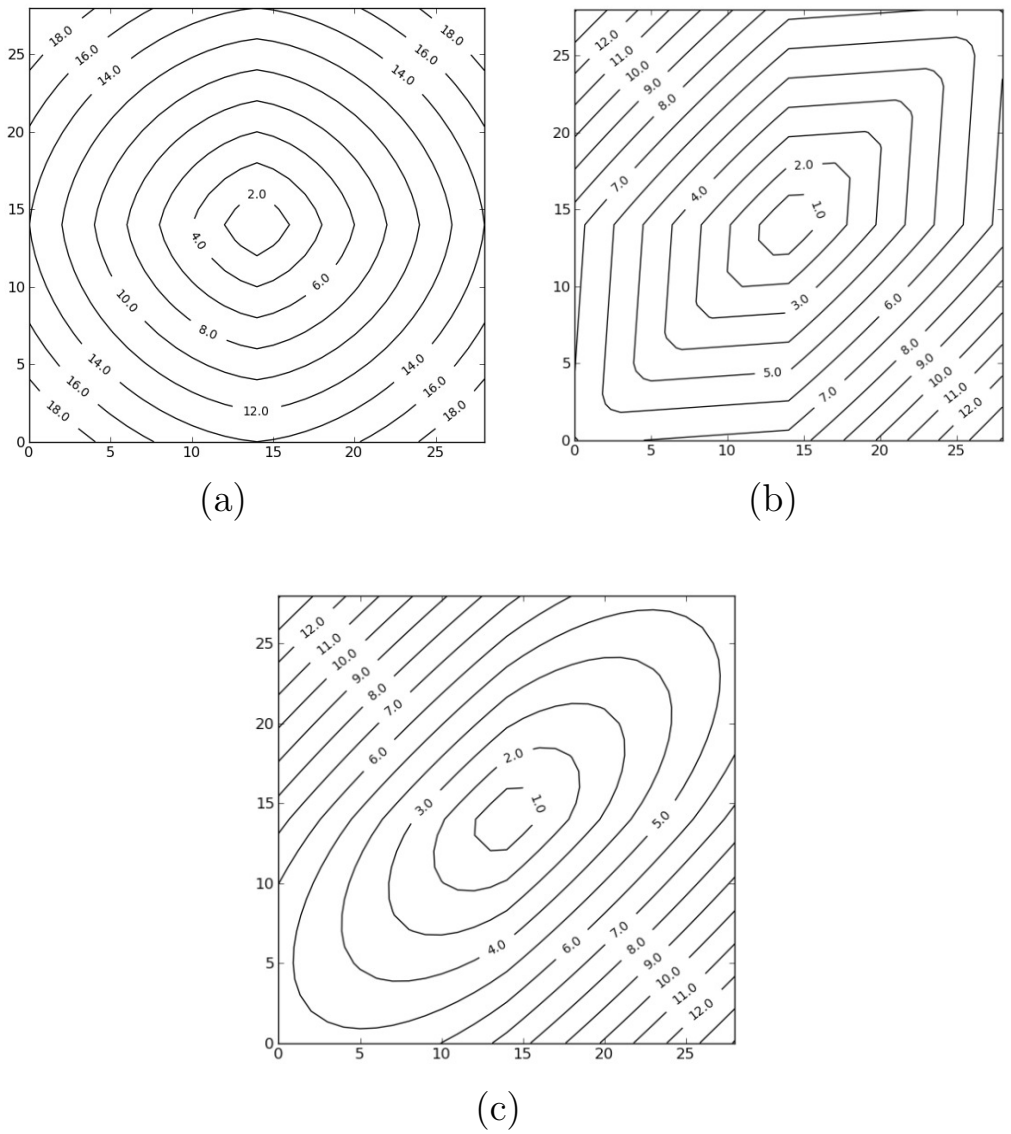

Figure 3.4: Results for a monotonically outward propagating front from a point source. (a) Isotropic permeability case using isotropic fast marching method. (b) Anisotropic permeability case using isotropic fast marching method. (c) Anisotropic permeability case using recursive fast marching method. The major axis of anisotropy is 45 degrees counterclockwise to the x axis for case (b) and (c).

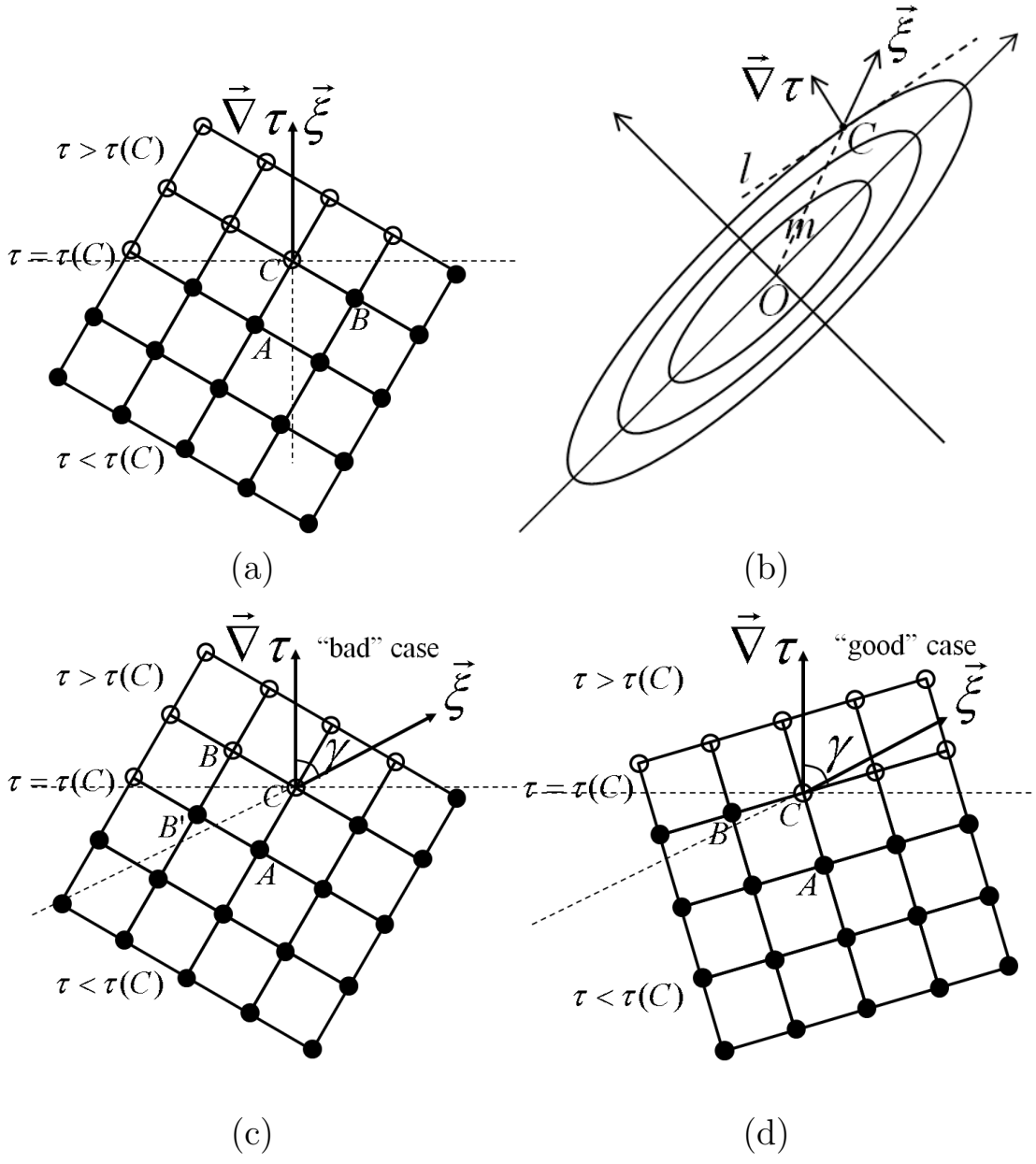

Figure 3.5: Illustration of the causality issues for isotropic and anisotropic cases.

the recursive fast marching method, was proposed by *Konukoglu et al.* (2007). This method contains a recursive correction step inside the main loop of the ordinary fast marching algorithm. The recursive construction allows one to build the entire "dependency graph" for any nodes and makes sure that the causality relationship is satisfied for the final accepted values. Figure 3.4(c) shows the solution of the same case as Figure 3.4(b) but using the recursive fast marching method leading to more accurate estimation of the front propagation.

Our formulation of the anisotropic fast marching in corner point grid discussed in the previous section will guarantee causality relationship so that the "bad case" shown in Figure 3.5(c) will not occur. For this, we must satisfy the underlying assumption in our formulation that the principle directions of anisotropy are aligned with local cell edges (*Alton and Mitchell*, 2008). As illustrated in Figure 3.6, suppose the speed of front propagation is given by the anisotropy ellipse which has major axis F_1 and minor axis F_2, both aligned with the grid. Suppose the characteristic direction at point C is known. We can show that the gradient direction will lie in the same cell as the characteristic direction. First, as shown in Figure 3.6(a), we take an arbitrary point S close and upwind to point C along the characteristic direction. We know that the shortest travel time to point C should come from point S. The local level line $\tau = \tau(S)$ at point S is denoted as L in Figure 3.6(b). We draw an ellipse of anisotropy centered at point C and passing through point S. It is shown in Figure 3.6(b) that the line L has to be tangent to the ellipse. This can be proved by contradiction. If the level line $\tau = \tau(S)$ at point S is not tangent to the ellipse (for example, line L'), suppose that it intersects the ellipse at another point P. Then the point S', which is the midpoint between S and P, will be inside the ellipse. Thus the travel time from S' to C will be smaller than from S to C. This is in contradiction with the assumption that SC is along the characteristic direction $\vec{\xi}$. Therefore, the line

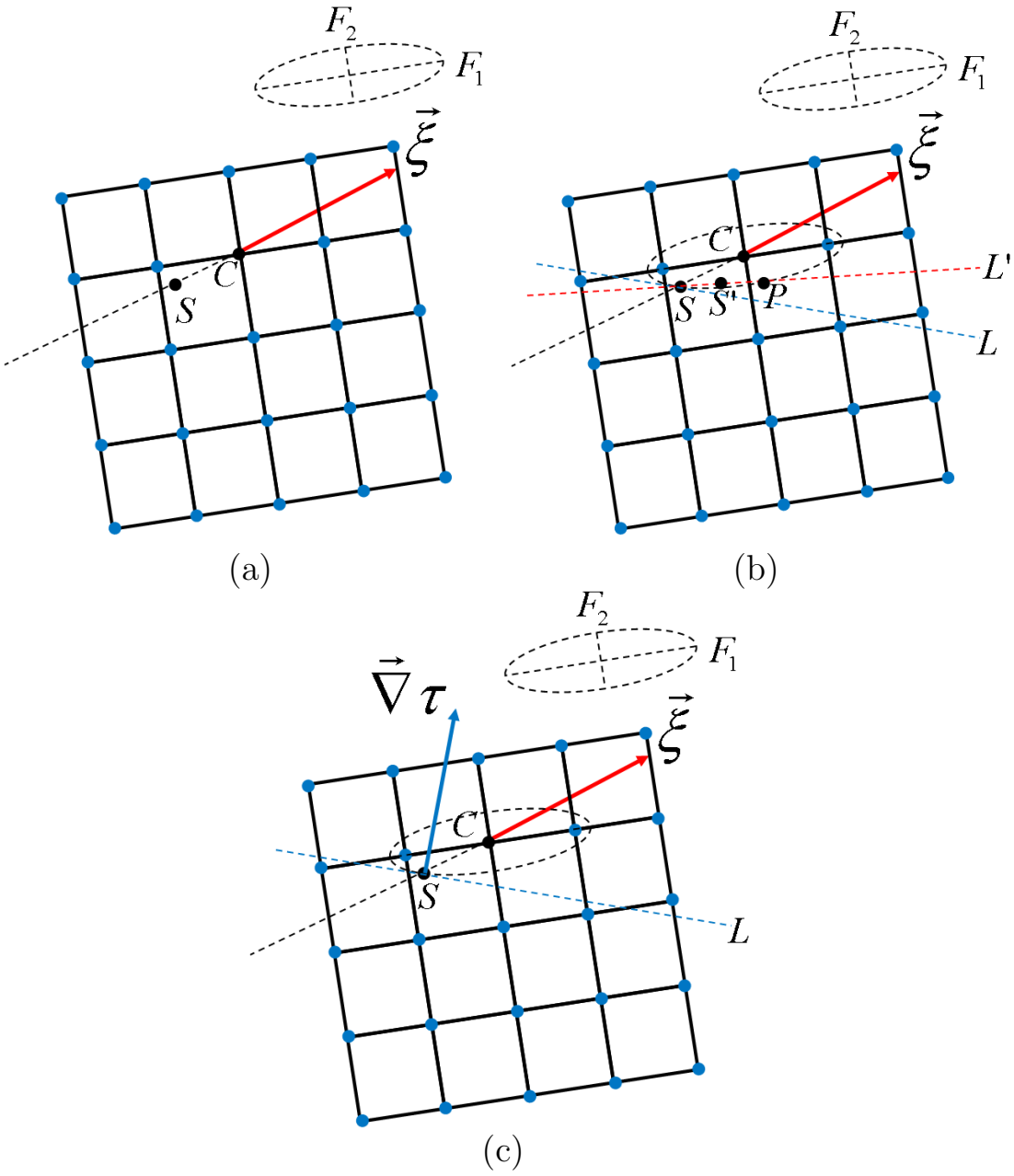

Figure 3.6: Illustration of the guarantee of causality relationship if the principle direction of anisotropy is aligned with the grid.

L must be tangent to the ellipse. The gradient direction $\nabla\tau$ will be perpendicular to the line L and thus will lie within the same cell as the characteristic direction $\vec{\xi}$. As point S moves infinitely close to point C, the gradient direction shown in Figure 3.6(c) becomes the gradient direction at point C. Therefore, we will have the "good" case as shown in Figure 3.4(d). Thus, as long as the principle directions of anisotropy are aligned with local cell edges, the causality condition will be satisfied by our proposed formulation.

3.5.2 Non-smoothly Varying Medium

The discussion in Section 3.5.1 rely on the assumption that the medium has smoothly-varying properties. However, for our discretized problem, it is possible to have dramatic change in permeability when going from one cell to its neighboring cells. This gives rise to additional concern for the "causality issue" because the travel time updated based on a cell's immediate neighbors in a 5-stencil scheme in 2D (or 7-stencil scheme in 3D) may not be the smallest possible if the diagonal neighboring cells are also taken into consideration. In this section, we will investigate this issue by doing some numerical experiments.

A 2D regular grid is used to simplify our discussion. First we enumerate all possible patterns of high permeability (100 md) sand grid block and low permeability (0.0001 md) non-sand grid block in a 2 by 2 local calculation scenario. We take the upper right corner grid block as the one to be updated in this local calculation. Assuming all other parameters are constant, we can simply calculate the direct travel time from the centers of its two immediate neighbors (bottom and left) and the center of its diagonal neighbor (bottom left) to the center of this grid block. The calculation is done in arbitrary units since we only concern with the relative value of the travel time. The results are shown in Figure 3.7. Out of the twelve different

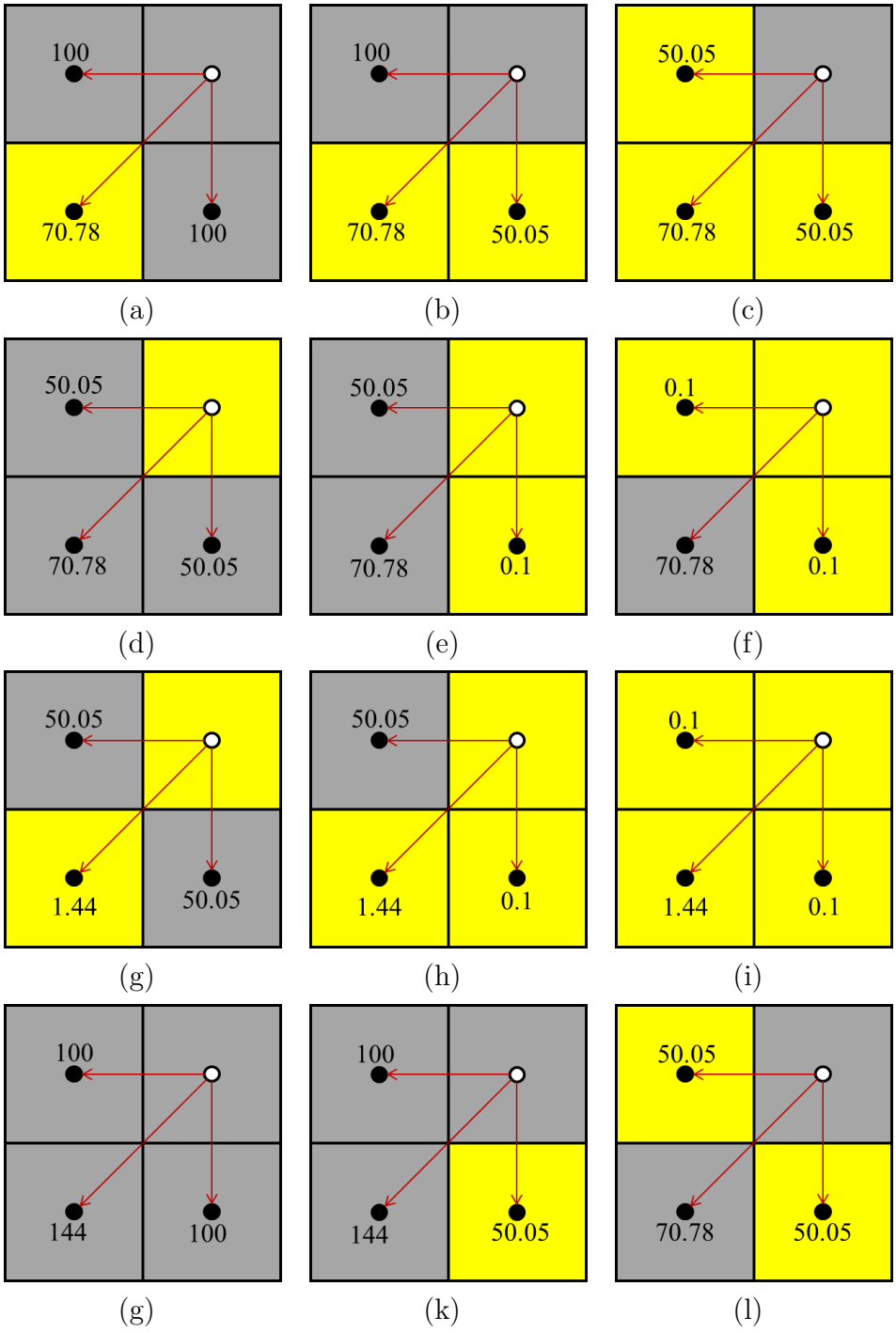

Figure 3.7: All twelve different high/low permeability patterns for 2 by 2 local solution. The upper right grid block is under consideration. The direct travel time from its neighbors are calculated and shown in the figures. In (a), (b), (g), and (h) the diagonal arrival time is smaller than at least one of immediate neighbors' travel time.

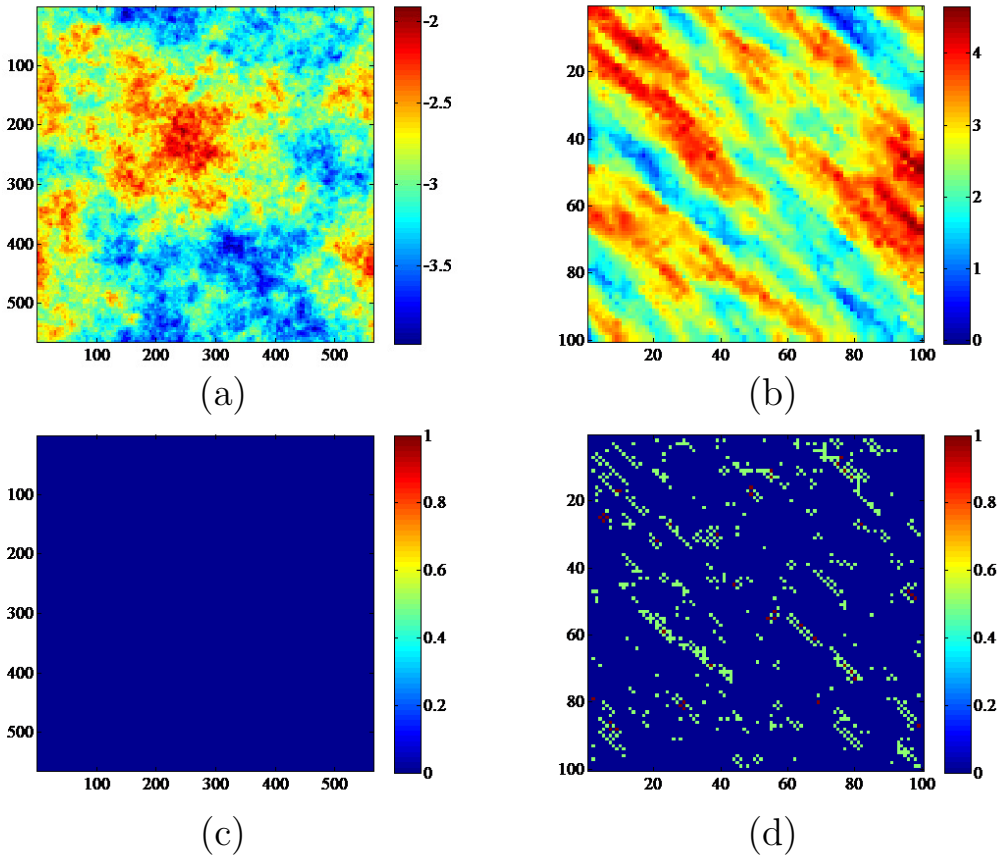

Figure 3.8: (a) $\log(k)$ of a heterogeneous permeability field which is relatively smooth; (b) $\log(k)$ of a heterogeneous permeability field with high contrast and channelized feature; (c) indicator numbers showing possible local "causality issue" for (a); (d) indicator numbers showing possible local "causality issue" for (b).

possible sand/non-sand patterns, only four situations will have the diagonal travel time smaller than at least one of the two immediate neighbors' travel time. These situations are (a), (b), (g), and (h). In situations (a) and (g), the front will arrive through the diagonal before both the immediate neighbors. If we allow flow between diagonal blocks, the 5-stencil FMM will produce relatively large error, especially for situation (g). If direct diagonal flow is not allowed, then the 5-stencil FMM is actually desirable in order to be consistent with finite difference simulation. In situations (b) and (h), the diagonal travel time is only smaller than one of the immediate neighbors' travel time. In general, the 5-stencil FMM might overestimate the travel time due to the local violation of causality.

Next we try to identify possible local violation of "causality issue" by doing the above local calculation for each grid block of a heterogeneous permeability field. For each grid block, we calculate the travel time from the grid block to its immediate neighbors (left, right, top, bottom) and its diagonal neighbors (top-left, top-right, bottom-left, bottom-right). For each diagonal neighbor, we compare its travel time with the two adjacent immediate neighbors' travel time. If the diagonal neighbor's travel time is smaller than both of the immediate neighbors' travel time, we will increase the grid block's indicator number by 1. If the diagonal neighbor's travel time is smaller than only one of the immediate neighbors' travel time, we will increase the grid block's indicator number by 0.5. A plot of the indicator numbers for all the grid blocks will show which grid blocks may have potential causality issue. We tested two heterogeneous permeability fields as shown in Figure 3.8. The first one varies relatively smoothly. The second one has local high contrast and channelized features (Figure 3.8(a) and (b)). For the first permeability field, no potential causality issue is discovered through this method (Figure 3.8(c)). But for the second permeability field, there are some grid blocks that have been identified with potential causality

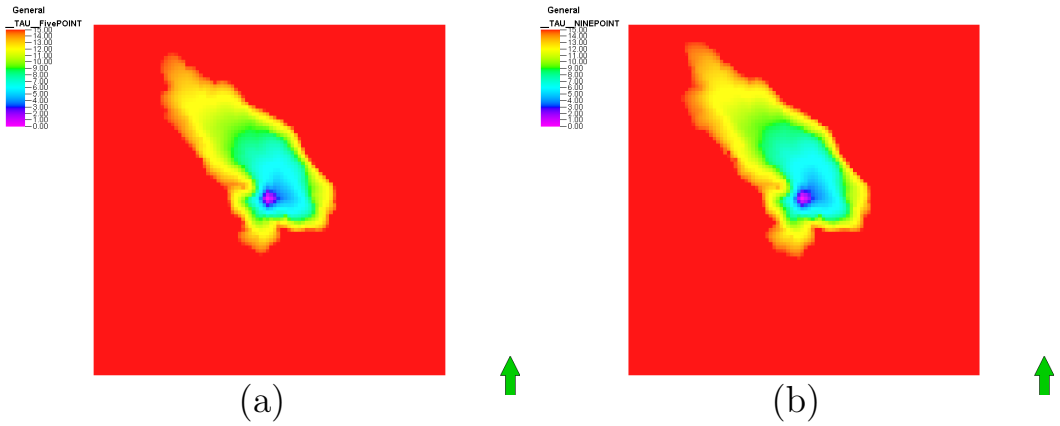

Figure 3.9: Diffusive time of flight calculated for the permeability field shown in Figure 3.8(b) using FMM based on (a) 5-stencil scheme and (b) 9-stencil scheme. The well is place in the center of the permeability field. The color bar is the same for both sub-figures and is capped by the same maximum value.

issue (Figure 3.8(d)). These grid blocks are located at the interface between the high permeability streaks and the low permeability regions. This shows that high contrast in permeability may potentially cause "causality issue".

Based on the permeability field shown in Figure 3.8(b) we have done some numerical experiment to show the effect of the "causality issue" on the diffusive time of flight calculation using the FMM. Figure 3.9 compares the results obtained using the 5-stencil scheme versus the 9-stencil scheme. Because the 9-stencil scheme takes the diagonal grid block into the local calculation, it is much less affected by the "causality issue". The diffusive time of flight calculated by the 5-stencil scheme is slightly larger than the values calculated by the 9-stencil scheme. Another way to reduce the "causality issue" is to refine and smooth the permeability field as shown in Figure 3.10. Figure 3.10(a) shows the same permeability field as Figure 3.8(b) but with much finer grid. We can see that the indicator numbers will be nonzero for a much smaller portion of the total grid blocks as shown in Figure 3.10(c). By

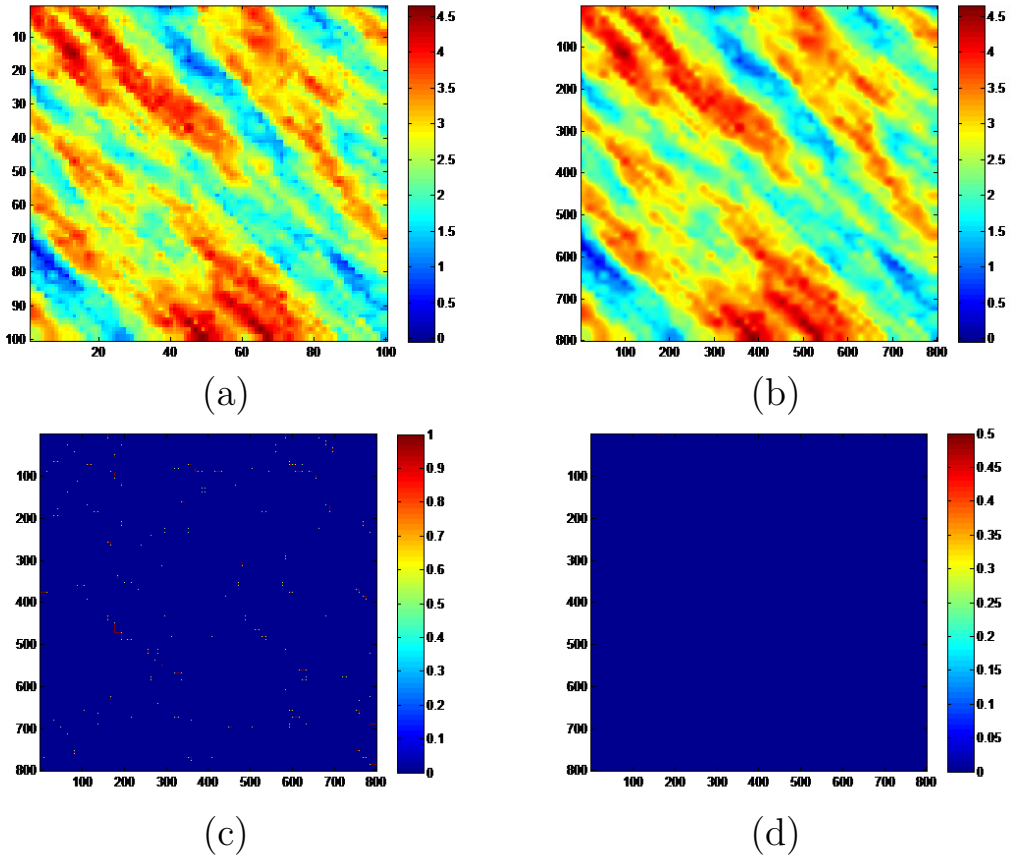

Figure 3.10: (a) Refined permeability field (800×800) based on the permeability field shown in Figure 3.8(b). Each original grid block is refined into 8×8 smaller grid blocks which retain the same permeability as the original coarse grid block. (b) Smoothed permeability field from (a) using a running 5-stencil average. (c) Indicator numbers showing possible causality issue for (a). (d) Indicator numbers showing possible causality issue for (b).

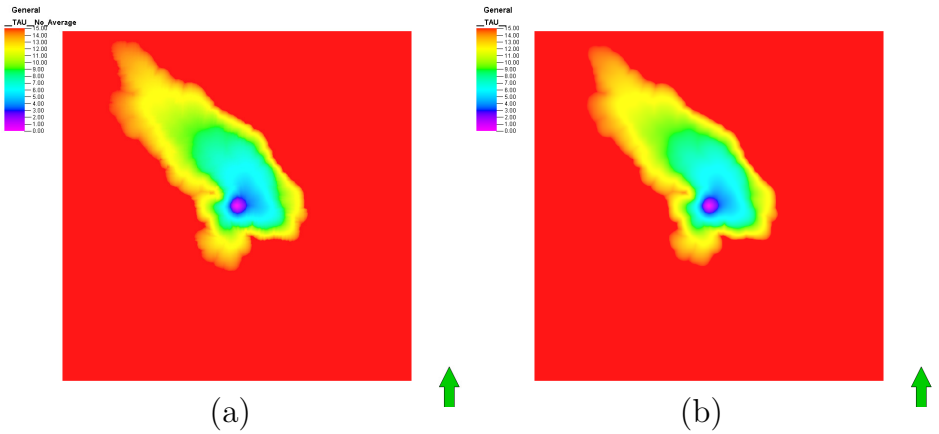

Figure 3.11: Diffusive time of flight calculated using the 5-stencil FMM scheme for (a) permeability field in Figure 3.10(a) and (b) permeability in Figure 3.10(b).

further smoothing the permeability field (Figure 3.10(b)) the indicator numbers of the permeability field can be completely removed (Figure 3.10(d)). The diffusive time of flight calculated by the 5-stencil FMM scheme is shown in Figure 3.11 for the permeability field in Figure 3.10. It is observed that refining and smoothing the permeability field produce similar results compared to using the 9-stencil scheme for the coarse grid.

Another way of dealing with the causality issue is to use the cell vertexes as the solution nodes instead of the cell centers. For a particular cell vertex, each local solution of the Eikonal Equation is always inside a particular cell volume with uniform cell properties. This guarantees "causality" because the nearest neighboring nodes always give the smallest travel time within that particular cell volume. Also because the averaging of properties between cells is avoided, the minimum possible travel time can always been found for the cell corners even if there is locally high permeability contrast between adjacent cells. Once the solution for all vertexes is obtained, the cell center solution can be locally solved within each cell based on

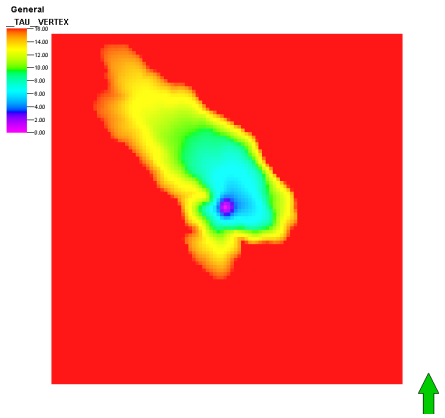

Figure 3.12: Diffusive time of flight calculated using the cell vertex based scheme for the permeability field in Figure 3.8(b).

the solution at its vertexes. Figure 3.12 shows the diffusive time of flight calculated using the cell vertex based approach for the permeability field shown in Figure 3.8(b). Comparing Figure 3.9 and 3.11 with Figure 3.12, it can be seen that the cell vertex based approach is also effective to avoid the "causality issue".

In general we observe the grid blocks where possible violation of the "causality issue" might happen are only located at the boundary of high and low permeability contrast. The fraction of these grid blocks are usually small and can be greatly reduced by grid refinement. The "causality issue" can also be avoided by using the cell vertex based approach. In highly heterogeneous and high-contrast permeability fields, the effect of the "causality issue" is not a significant concern compared with missing the higher order terms in the asymptotic solution as discussed in Section 1.1.2.

3.6 FMM in Unstructured Grids

The basic framework of FMM for unstructured grids is exactly the same as structured grids (*Sethian and Vladimirsky*, 2000). The only difference is how we get the

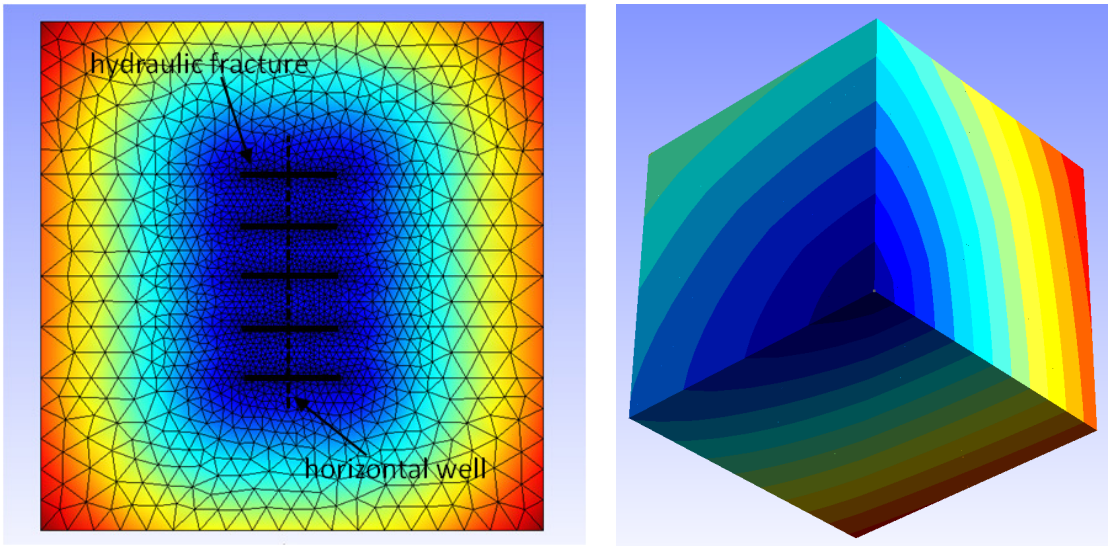

(a) (b)

Figure 3.13: Fast marching examples using unstructured triangular mesh (a) 2D example with isotropic permeability; (b) 3D example with anisotropic permeability (aspect ratio is 3:2:1).

local updates. Appendix B describes two general local solvers which treat 5-stencil Cartesian grid, 9-stencil Cartesian grid, and unstructured grids in a uniform manner (*Qian et al.*, 2007). Figure 3.13 shows two illustrative examples using triangular mesh in 2D and 3D. Figure 3.13(a) shows the calculated diffusive time of flight in a homogeneous isotropic field with a horizontal well completed by five transverse hydraulic fractures. Figure 3.13(b) shows the point source solution for an anisotropic case in 3D.

3.7 Results and Applications

One of the most immediate and effective use of the method is for reservoir drainage volume calculations and visualization. Figure 3.14(a) shows a reservoir model with matrix permeability ranges from 1 nanodarcy to 0.001 millidarcy. The k_z/k_x ratio is 0.1 and $k_x = k_y$ for this case. The reservoir is $4000ft \times 2000ft \times 120ft$

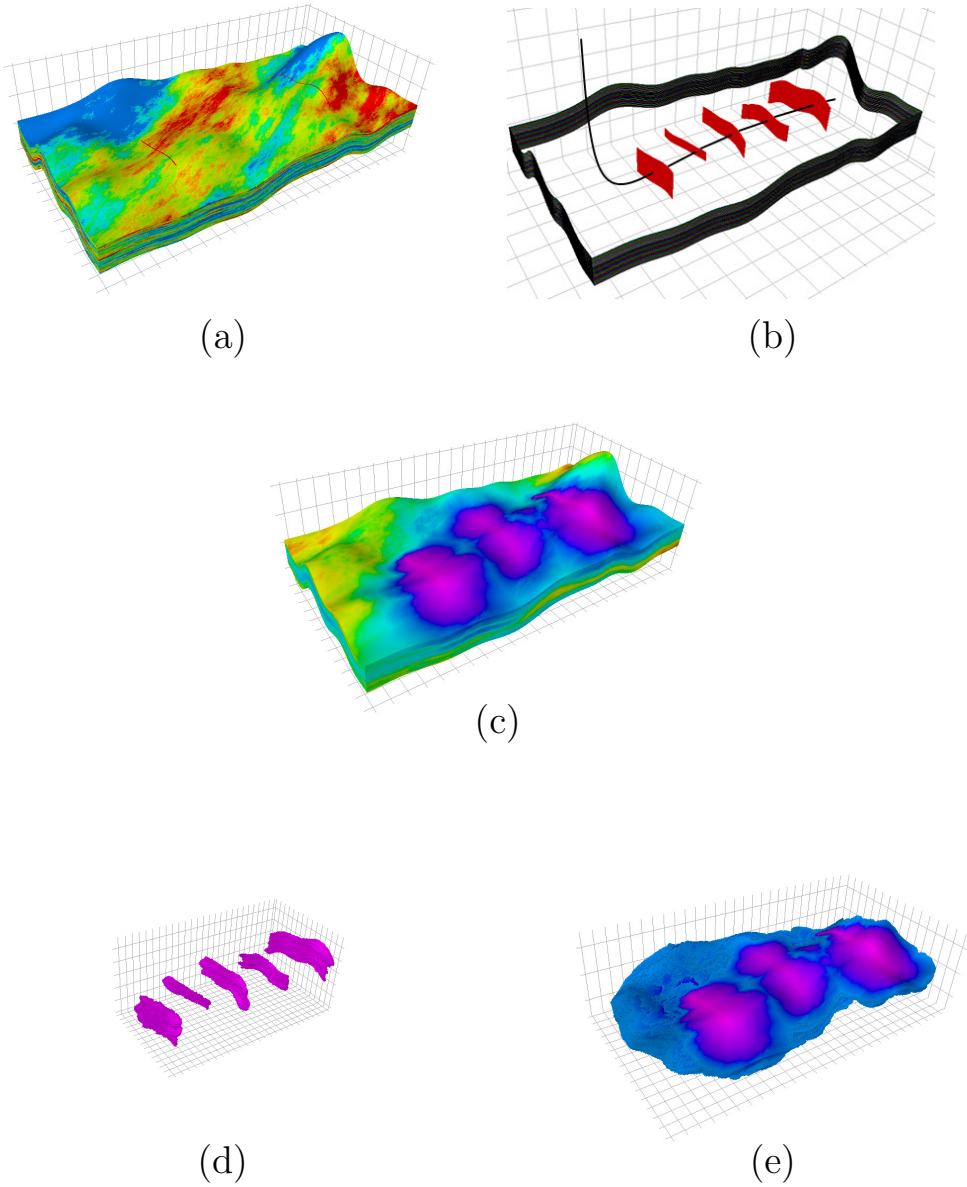

Figure 3.14: A synthetic example of a heterogeneous reservoir with five transverse hydraulic fractures. (a) permeability field; (b) the geometry of five transverse fractures; (c) calculated diffusive time of flight; (d) drainage volume in 1 month; (e) drainage volume in 30 years.

and contains $400 \times 200 \times 30$ corner point cells. There are 5 transverse hydraulic fractures intersecting a horizontal well as shown in Figure 3.14(b). These fractures have different half length, height and location in the reservoir. Moreover, using corner point grid enables us to simulate even non-planer fractures such as in this example. The permeability of the hydraulic fractures is set to be 10 millidarcy, while porosity, viscosity, and compressibility are taken to be constant values of 0.1, $0.1cp$, and $3 \times 10^{-5} psi^{-1}$ respectively. Figure 3.14(c) shows the result of the calculated diffusive time of flight using the fast marching approach. By transforming the diffusive time of flight to physical time, we are able to visualize the drainage volume for any given time. For example, Figure 3.14(d) and (e) show the drainage volume at 1 month and 30 years respectively. The fast marching calculation for this 2.5 million cell example takes about 15 minutes using a laptop computer. In contrast, finite difference simulation for such multi- million cell model is likely to take much longer computation time.

3.8 Conclusions

In this section, we have derived the formulation of the FMM in corner point grids, which is one of the most widely used grids for reservoir models. We have discussed the causality issue associated with permeability anisotropy for smoothly varying medium. If the principle directions of the permeability are aligned with the cell edges, which is usually the assumption for reservoir simulation models, the proposed FMM formulation for corner point grids will satisfy the causality relationship. For non-smoothly varying medium, we have done some numerical experiments to study the effect of possible local violation of causality at the boundary of high permeability contrast. We have also shown that the FMM approach can be applied to unstructured grid, which is gaining increased acceptance.

The concept of depth of investigation is important to characterize the production in unconventional reservoirs, because the boundary effects will rarely be seen during the lifetime of a well and all the production is obtained during the transient flow regime. This is why the FMM approach can be effectively applied to unconventional reservoirs. As we have demonstrated, it is straightforward to use the FMM for drainage volume calculations and visualization for unconventional reservoirs and wells with multi-stage hydraulic fractures. Furthermore, we will show in the next section methods to associate the reservoir pressure with the evolving drainage volume and provide an easy way for well performance characterization and forecasting.

4. PRESSURE SOLUTION BASED ON DIFFUSIVE TIME OF FLIGHT

4.1 Synopsis

Streamline method underpins the petroleum industry's use of streamline simulation and streamline-based reservoir calibration, management and optimization for convection dominated flow such as water-flood. In the streamline method, the use of the convective time of flight as a spatial variable along streamlines effectively reduces the calculation to only one dimension. Furthermore, the convective time of flight greatly simplifies the calculation of reservoir parameter sensitivity and facilitates data integration and reservoir management optimization applications. For pressure depletion and associated reservoir processes, our expectation is that the adoption of the diffusive time of flight will allow similar advancements in methods and applications. In this section, we will explore the use of the diffusive time of flight as a spatial coordinate for development of an effective one dimensional equation from the pressure diffusivity equation.

Our analysis in previous sections has demonstrated that reservoir heterogeneity information can be integrated into the drainage volume and the diffusive time of flight calculation as illustrated in Figure 4.1. Recent published work has emphasized the calculation of each of these quantities, and a specific pseudo-steady state (PSS) geometric approximation to the pressure and rate (*Xie et al.*, 2012a,b). Compared with the PSS geometric approximation, the new method is much more general theoretically in the sense that additional physics can be easily incorporated elegantly into the formulation as necessary. Another advantage is that both pressure and rate boundary conditions can be used without significant change of the formulation and calculation procedures. Finally, the new formulation does not assume PSS condition

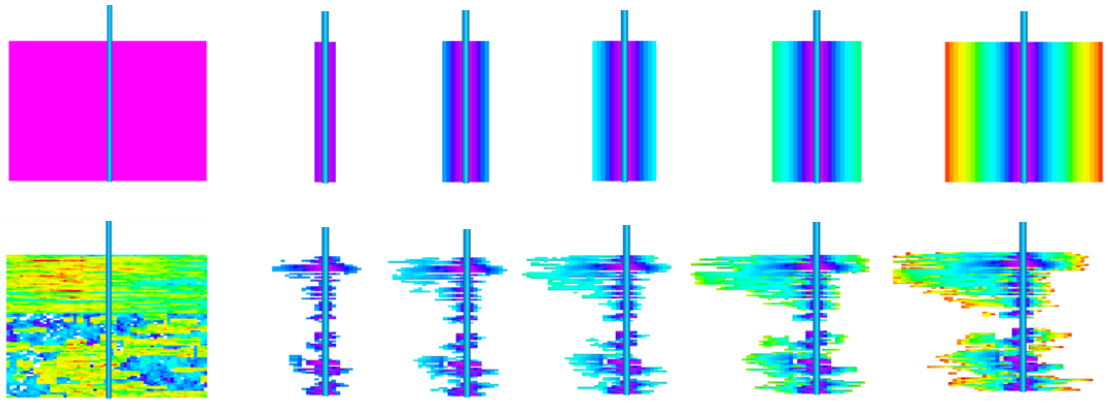

Figure 4.1: Illustration of the diffusive time of flight in a homogeneous reservoir (upper) and in a heterogeneous reservoir (lower).

and produces more accurate results for pressure distributions.

This novel method has many potential applications. It can be used to predict reservoir pressures and rates, especially to optimize multi-stage fracture design in tight and unconventional reservoirs, to optimize well spacing and timing in conventional reservoirs, and to rank and/or calibrate reservoir models against field performance data.

4.2 Background

Xie et al. (2012a) proposed a pseudo-steady state geometric approximation for pressure calculation based on the drainage volume and diffusive time of flight. To derive this approximation, we first express the diffusivity equation in a mixed form by introducing the Darcy flux Q:

$$A(r)\phi c_t \frac{\partial P}{\partial t} = \frac{\partial Q}{\partial r} \tag{4.1}$$

and

$$Q = \frac{kA(r)}{\mu}\frac{\partial P}{\partial r} \tag{4.2}$$

Here, $A = 2\pi rh$ is the surface area for cylindrical flow, and similarly, $A = 4\pi r^2$ is the surface area for spherical flow, and A is a constant for linear flow. The sign convention used here is that Q is positive for producers (inwardly directed flux) and ΔP is the pressure draw-down. Following the chain rule, we have

$$\frac{\partial Q}{\partial r} = \frac{\partial Q}{\partial V_p}\frac{\partial V_p}{\partial r} = \frac{\partial Q}{\partial V_p}\phi A(r) \tag{4.3}$$

Expressed in terms of the pore volume, Equation 4.1 can be rewritten as

$$c_t\frac{\partial P}{\partial t} = \frac{\partial Q}{\partial V_p} \tag{4.4}$$

The geometric approximation assumes that the Darcy flux is negligible beyond the drainage volume and that within the drainage volume the pressure is approximated by a pseudo-steady state solution (*Nordbotten et al.*, 2004; *Agarwal*, 2010; *Xie et al.*, 2012a). Based on these assumptions, we have

$$\frac{\partial P}{\partial t} \cong \frac{\partial \bar{P}}{\partial t} = \frac{Q_w}{c_t V_p(t)} \tag{4.5}$$

where Q_w is the well flow rate. Therefore, we can get the well pressure draw-down transient diagnostic plot by

$$\frac{dP_w}{d\ln t} = t\frac{dP_w}{dt} = \frac{Q_w t}{c_t V_p(t)} \tag{4.6}$$

Equation 4.5 can be integrated to get approximate pressure distribution and bottom-hole pressure (BHP). Equation 4.6 is especially useful for flow regime diagnostics.

The above derivation is under the constant flow rate boundary condition. The constant wellbore pressure boundary condition requires a different formulation as shown by *Xie et al.* (2012b).

In order to use Equation 4.5 and 4.6, we need to get the drainage pore volume as a function of time. However, from the FMM calculation what we obtain is the drainage pore volume as a function of the diffusive time of flight τ. Therefore, it is necessary to convert the diffusive time of flight τ to real time t. As discussed in section 3.3, this conversion can be done straightforwardly for homogeneous case as shown by Equation 3.3. However, for heterogeneous case, there is no clear global flow pattern and the τ to t conversion does not have a simple solution.

We argue that it is more natural and beneficial to treat τ as a spatial variable rather than a time variable. This leads us to seek a new formulation of the diffusivity equation using τ as a spatial variable. The new formulation is expected to reduce exactly back to the original diffusivity equation for 1D, 2D, and 3D homogeneous cases. This makes sure that we have a sound starting point to extend to heterogeneous reservoirs. We will demonstrate that the τ-coordinate formulation is able to provide a reasonable approximation for heterogeneous reservoirs with much less computational cost than solving the 3D diffusivity equation directly. In addition, we will attempt to incorporate additional physical processes into the formulation, which is potentially important in shale gas reservoir applications.

4.3 Methodology

4.3.1 Basic Formulation

In this section, we will show the basic formulation for slightly compressible fluid and isotropic medium. Extension to anisotropy and compressible fluid cases are discussed in detail in Appendix C. We make the following assumptions:

1. Darcy flow

2. No gravity effects

3. Isotropic properties

4. Fluid has small, constant compressibility

5. No geomechanical effects

Under these assumptions, the diffusivity equation is

$$\nabla \cdot \left(\frac{k}{\mu} \nabla P \right) = \phi c_t \frac{\partial P}{\partial t} \tag{4.7}$$

Our goal is to rewrite Equation 4.7 from a 3D equation to a 1D equation in space using the diffusive time of flight τ as the new spatial coordinate variable. To simplify the notation, we introduce the diffusivity $\alpha = k/\phi\mu c_t$. Then Equation 4.7 can be written as

$$\nabla \cdot (\phi c_t \alpha \nabla P) = \phi c_t \frac{\partial P}{\partial t} \tag{4.8}$$

The diffusive time of flight τ is calculated in isotropic medium according to the Eikonal equation

$$\|\nabla \tau\| = \frac{1}{\sqrt{\alpha}} \tag{4.9}$$

To reduce the diffusivity equation to only one dimensional in space, we will assume that the pressure only depends on τ in space. This is equivalent to assume that the pressure gradient direction aligns with the τ gradient direction, or the contour surfaces of pressure P are also the contour surfaces of τ. Based on this assumption, we can write

$$\nabla P \approx \frac{\partial P}{\partial \tau} \nabla \tau = \frac{\partial P}{\partial \tau} \frac{1}{\sqrt{\alpha}} \hat{\mathbf{n}}_\tau \tag{4.10}$$

Here we have incorporated the Eikonal equation (Equation 4.9) into the formulation and $\hat{\mathbf{n}}_\tau$ is the unit normal vector to the contour of τ. Substituting Equation 4.10 into Equation 4.8, we have

$$\nabla \cdot \left(\phi c_t \sqrt{\alpha} \frac{\partial P}{\partial \tau} \hat{\mathbf{n}}_\tau \right) = \phi c_t \frac{\partial P}{\partial t} \tag{4.11}$$

The divergence operator in 3D Cartesian space is written as

$$\nabla \cdot \vec{\mathbf{F}} = \frac{\partial F_x}{\partial x} + \frac{\partial F_y}{\partial y} + \frac{\partial F_z}{\partial z} \tag{4.12}$$

We would like to do a coordinate transformation from (x, y, z) to (τ, ψ, χ), where τ is the diffusive time of flight and the other two coordinates ψ and χ are defined on the contour surfaces of τ and are orthogonal to each other and to τ. The divergence operator in the (τ, ψ, χ) coordinate system can be written as

$$\nabla \cdot \vec{\mathbf{F}} = \frac{1}{h_\tau h_\psi h_\chi} \left(\frac{\partial (h_\psi h_\chi F_\tau)}{\partial \tau} + \frac{\partial (h_\tau h_\chi F_\psi)}{\partial \psi} + \frac{\partial (h_\tau h_\psi F_\chi)}{\partial \chi} \right) \tag{4.13}$$

Here h_τ, h_ψ, and h_χ are the length of the covariant vectors. For example, h_τ is the length of the covariant vector $\vec{\mathbf{t}}_\tau$,

$$\vec{\mathbf{t}}_\tau = \frac{\partial \vec{\mathbf{x}}}{\partial \tau} = \left(\frac{\partial x}{\partial \tau}, \frac{\partial y}{\partial \tau}, \frac{\partial z}{\partial \tau} \right) \tag{4.14}$$

The definitions of the other two covariant vectors are similar. If we write the divergence operator in Equation 4.11 according to Equation 4.13, we will have

$$\frac{1}{h_\tau h_\psi h_\chi} \frac{\partial}{\partial \tau} \left(\phi c_t h_\psi h_\chi \sqrt{\alpha} \frac{\partial P}{\partial \tau} \right) = \phi c_t \frac{\partial P}{\partial t} \tag{4.15}$$

The differential terms in ψ and χ do not appear because the vector function to be taken the the divergence has only τ direction component. It can be obtained from Equations 4.9 and 4.14 that $h_\tau = \sqrt{\alpha}$. The product $h_\tau h_\psi h_\chi$ is simply the Jacobian J of the coordinate transformation. Therefore, Equation 4.15 reduces to

$$\frac{\partial}{\partial \tau}\left(J\phi\frac{\partial P}{\partial \tau}\right) = J\phi\frac{\partial P}{\partial t} \tag{4.16}$$

The Jacobian J and the porosity ϕ are functions of (τ, ψ, χ) in general. In order to further reduce Equation 4.16 to only depend on τ, we integrate both sides over the other two coordinates ψ and χ which are orthogonal to τ. Because the pressure P is assumed to be only a function of τ and t, it can be taken out of that integral. Thus Equation 4.16 reduces to

$$\frac{\partial}{\partial \tau}\left(w(\tau)\frac{\partial P}{\partial \tau}\right) = w(\tau)\frac{\partial P}{\partial t} \tag{4.17}$$

where

$$w(\tau) = \iint \phi J(\tau, \psi, \chi) d\psi d\chi \tag{4.18}$$

The function $w(\tau)$ can be related to the drainage pore volume by

$$w(\tau) = \iint \phi J(\tau, \psi, \chi) d\psi d\chi = \frac{dV_p(\tau)}{d\tau} \tag{4.19}$$

because the drainage pore volume can be written as

$$V_p(\tau) = \int_{\tau_0}^{\tau} \left(\iint \phi J(\tau, \psi, \chi) d\psi d\chi\right) d\tau \tag{4.20}$$

4.3.2 Special Cases

In this subsection, we will illustrate that the new formulation will reduce back to the ordinary diffusivity equations in 1D, 2D, and 3D homogeneous medium. For 1D linear flow, we have

$$\tau = \frac{x}{\sqrt{\alpha}} \tag{4.21}$$

where x is the linear distance. The drainage pore volume can be written as

$$V_p(\tau) = \phi A x = \phi A \sqrt{\alpha} \tau \tag{4.22}$$

where A is the intersectional area. Therefore,

$$w(\tau) = \frac{dV_p}{d\tau} = \phi A \sqrt{\alpha} \tag{4.23}$$

Substitute this equation into Equation 4.17. We get

$$\frac{\partial^2 P}{\partial \tau^2} = \frac{\partial P}{\partial t} \tag{4.24}$$

Substitute Equation 4.21 and write the equation in terms of x coordinate. Then we arrive at the ordinary diffusivity equation in 1D homogeneous medium

$$\frac{\partial^2 P}{\partial x^2} = \frac{\phi \mu c_t}{k} \frac{\partial P}{\partial t} \tag{4.25}$$

For 2D radial flow, we have

$$\tau = \frac{r}{\sqrt{\alpha}} \tag{4.26}$$

where r is the radial distance. The drainage pore volume can be written as

$$V_p(\tau) = \pi\phi r^2 h = \pi\phi\alpha\tau^2 h \tag{4.27}$$

Therefore,

$$w(\tau) = \frac{dV_p}{d\tau} = 2\pi\phi\alpha h\tau \tag{4.28}$$

Substitute this equation into Equation 4.17. We get

$$\frac{1}{\tau}\frac{\partial}{\partial\tau}\left(\tau\frac{\partial P}{\partial\tau}\right) = \frac{\partial P}{\partial t} \tag{4.29}$$

Substitute Equation 4.26 and write the equation in terms of r coordinate. Then we arrive at the ordinary diffusivity equation in 2D homogeneous medium

$$\frac{1}{r}\frac{\partial}{\partial r}\left(r\frac{\partial P}{\partial r}\right) = \frac{\phi\mu c_t}{k}\frac{\partial P}{\partial t} \tag{4.30}$$

For 3D spherical flow, we have

$$\tau = \frac{r}{\sqrt{\alpha}} \tag{4.31}$$

where r is the radial distance. The drainage pore volume can be written as

$$V_p(\tau) = \frac{4}{3}\pi\phi r^3 = \frac{4}{3}\pi\phi\alpha^{3/2}\tau^3 \tag{4.32}$$

Therefore,

$$w(\tau) = \frac{dV_p}{d\tau} = 4\pi\phi\alpha^{3/2}\tau^2 \tag{4.33}$$

Substitute this equation into Equation 4.17. We get

$$\frac{1}{\tau^2}\frac{\partial}{\partial\tau}\left(\tau^2\frac{\partial P}{\partial\tau}\right)=\frac{\partial P}{\partial t} \tag{4.34}$$

Substitute Equation 4.31 and write the equation in terms of r coordinate. Then we arrive at the ordinary diffusivity equation in 3D homogeneous medium

$$\frac{1}{r^2}\frac{\partial}{\partial r}\left(r^2\frac{\partial P}{\partial r}\right)=\frac{\phi\mu c_t}{k}\frac{\partial P}{\partial t} \tag{4.35}$$

4.3.3 Boundary Conditions

One advantage of the τ-coordinate formulation over the PSS geometric approximation is that it is more straightforward to implement the solution based on various boundary conditions and incorporate additional physics. The pressure boundary condition can be simply written as

$$P|_{\tau=\tau_w}=P_{wf} \tag{4.36}$$

for the wellbore and

$$P|_{\tau=\tau_e}=P_e \tag{4.37}$$

for the outer boundary. Here the solution domain is $[\tau_w,\tau_e]$. The lower bound τ_w corresponds with the wellbore radius and the upper bound τ_e corresponds with the boundary of the reservoir. τ_w can be calculated from the wellbore radius by

$$\tau_w=r_w\sqrt{\frac{\phi_w\mu c_t}{k_w}} \tag{4.38}$$

where ϕ_w and k_w are porosity and permeability at the wellbore. This relationship can be generalized for heterogeneous multi-layered reservoir as

$$\tau_w = r_w \sqrt{\frac{\mu c_t \sum_i \phi_{wi} h_i}{\sum_i k_{wi} h_i}} \tag{4.39}$$

where the thickness weighted summations of porosities and permeabilities for each completion layer are used.

Following the derivation from Equation 4.7 to 4.16, it can be seen that the flux term has the following corresponding relationship

$$\frac{k}{\mu} \nabla P = c_t J \phi \frac{\partial P}{\partial \tau} \tag{4.40}$$

Because from Equation 4.16 to Equation 4.17 we apply the surface integration over the area perpendicular to the reservoir flow, the flow rate relationship can then be written as

$$q = A \frac{k}{\mu} \nabla P = c_t w(\tau) \frac{\partial P}{\partial \tau} \tag{4.41}$$

Therefore, the flow rate boundary conditions can be written for Equation 4.17 as

$$\left(w(\tau) \frac{\partial P}{\partial \tau} \right)_{\tau = \tau_w} = \frac{q_w}{c_t} \tag{4.42}$$

for the wellbore and

$$\left(w(\tau) \frac{\partial P}{\partial \tau} \right)_{\tau = \tau_e} = \frac{q_e}{c_t} \tag{4.43}$$

for the outer boundary. Here q_w is the down-hole flow rate at the wellbore. For no-flow boundary condition, q_e is zero. Different boundary conditions can be imposed at different times and this will be illustrated later in the result section. The rate boundary conditions for compressible fluid is shown in Appendix C.2.

4.3.4 Drainage Volume Derivative Calculation

To solve Equation 4.17, the drainage volume derivative $w(\tau)$ needs to be evaluated. This is critical because the $w(\tau)$ function contains the reservoir heterogeneity information. The drainage pore volume $V_p(\tau)$ can be calculated using the FMM as described in Section 3. Because the reservoir is discretized into grid blocks, during the process of the FMM calculation, the drainage pore volume can be gradually accumulated as new grid blocks are being accepted. However, this raw correspondence between τ and V_p can not be directly used for derivative calculation because the data is not locally smooth. An ideal solution to this problem would be to generate 3D τ contour surfaces using the calculated τ values at each cell center. Then calculate the volume enclosed by each τ contour for the corresponding value of τ. However, this requires some 3D contouring algorithm which may be very complex and computationally expensive. We choose to use a customized Gaussian kernel smoother for the raw V_p versus τ data collected during the FMM calculation. The advantage is that it is computationally cheap and easy to implement. The disadvantage is that the bandwidth of the Gaussian kernel needs to be customized to give the best results. A super-smoother has also been tried but has not been adopted because it may over-smooth the data and give wrong results especially at the lower end of τ values. Once the V_p versus τ data has been smoothed, we can calculate the derivative based on a weighted average between the upstream and the downstream derivatives as proposed by *Bourdet et al.* (1989).

4.4 Extension for Additional Physics in Shale Gas Reservoirs

In Section 1.1.4 we have briefly introduced some additional physics that are potentially important in shale gas reservoir production. In order to make the new formulation applicable for more realistic shale gas reservoirs, in this section we at-

tempt to incorporate those additional physics into the formulation.

The reservoir compaction effect and the gas slippage effect can be treated using a decoupled model, in which the effects are represented by pressure dependant permeabilities and porosities. A more rigorous coupled model could be a future research topic. Under the decoupled model, we assume in general that permeabilities and porosities can be written as the values at the initial conditions multiplied by certain multipliers which are known functions of pressure, e.g. $k(P) = k_i M_k(P)$ and $\phi(P) = \phi_i M_\phi(P)$. Because the reservoir properties changes with time, we could not rely on the relationship of τ with the pressure front propagation for pressure calculation. As a result, it is difficult to apply the PSS geometric approximation to these situations. However, the new τ-coordinate formulation is not restricted by this. We simply use the permeabilities and porosities at the initial reservoir condition in the FMM calculation to obtain the diffusive time of flight τ, and we do not rely on any specific physical meaning of τ other than it is a spatial coordinate which has incorporated the heterogeneity information. Based on the decoupled model, following the same derivation as shown in Appendix C.2, the final τ-coordinate formulation for shale gas reservoirs can be written as

$$\frac{\partial}{\partial \tau}\left(w(\tau)\frac{M_k(P)P}{\tilde{\mu}(P)Z(P)}\frac{\partial P}{\partial \tau}\right) = w(\tau)M_\phi(P)\tilde{c}_t(P)\frac{P}{Z(P)}\frac{\partial P}{\partial t} \tag{4.44}$$

where $M_k(P)$ and $M_\phi(P)$ are permeability and porosity multipliers respectively.

The gas adsorption and diffusion can be incorporated by adding additional accumulation and source terms in the diffusivity equation (*Shabro et al.*, 2012):

$$-\nabla \cdot (\rho \vec{\mathbf{u}}) = \frac{\partial}{\partial t}\left(\rho\phi + \rho_{ST}V_{ads}\right) - \rho_{ST}J \tag{4.45}$$

In this equation, V_{ads} is the adsorbed gas (in standard cubic feet per unit volume of shale) introduced in Section 1.1.4. J is the diffusion gas flow rate (in standard cubic feet per day per unit volume of shale). ρ_{ST} is the gas density at the standard condition. We assume that a transfer function can be applied for the gas diffusion between kerogen and pore system, thus we have

$$J = \sigma D_k (C_k - C_e(P)) \tag{4.46}$$

Here σ (unit: ft^{-2}) is a factor to account for the kerogen-pore interface area per unit bulk volume. D_k (unit: ft^2/day) is the diffusion coefficient in kerogen. C_k (unit: scf/ft^3) is the gas concentration in kerogen. $C_e(P)$ is the kerogen gas concentration in equilibrium with the free gas in the pore at pressure P. Mass balance of gas in kerogen gives:

$$\frac{\partial C_k}{\partial t} = -J \tag{4.47}$$

The coupled Equations 4.45 and 4.47 should be solved together. Following the same procedure in Appendix C.2, Equation 4.45 can be re-written using the τ coordinate as

$$\frac{\partial}{\partial \tau}\left(w(\tau)\frac{P}{\tilde{\mu}(P)Z(P)}\frac{\partial P}{\partial \tau}\right) = \left\{w(\tau)\frac{\tilde{c}_t(P)P}{Z(P)} + v(\tau)Y\frac{dV_{ads}}{dP}\right\}\frac{\partial P}{\partial t} + v(\tau)YJ \tag{4.48}$$

In this equation, Y is the constant group $(P_{ST}T)/(T_{ST}c_{ti})$. A new function $v(\tau)$ is introduced as

$$v(\tau) = \frac{dV_b(\tau)}{d\tau} \tag{4.49}$$

where $V_b(\tau)$ is the reservoir bulk volume calculated as a function of τ. This can be calculate at the same time as the drainage pore volume $V_p(\tau)$.

This formulation is essentially a dual porosity model in τ-coordinate. Here the pore system can be seen as the "fracture" and the kerogen the "matrix". It is also possible to use the same formulation for dual porosity naturally fractured reservoirs.

4.5 Results and Discussions

4.5.1 Oil Case

To start with, we use homogeneous oil reservoir in 1D, 2D, and 3D to generate benchmark for both the τ-coordinate formulation and the PSS geometric approximation. As shown in Section 4.3.2, the τ-coordinate formulation reduces back to the ordinary form of the diffusivity equation for homogeneous reservoirs in 1D, 2D, and 3D. Therefore, for homogeneous reservoirs, the τ-coordinate formulation gives exactly the same results as solving the diffusivity equation directly. The calculation for the geometric approximation in homogeneous reservoirs can be done analytically as shown in Appendix D. In the following examples, we use the reservoir properties listed in Table 4.1 and the geometry data listed in Table 4.2. We use constant flow rate inner boundary condition and infinite acting outer boundary condition. Figures 4.2 to 4.4 show the pressure at the inner boundary as a function of time. Figures 4.5 to 4.7 show the pressure profile at the end of the simulation time. By comparing the results given by the PSS geometric approximation with the direct solution of the diffusivity equation, we observe relatively large error for 1D linear flow compared with the 2D and 3D cases. These errors are thought to be associated with the PSS assumption used in the formulation. The correct pressure profile in the 1D case (solid line in Figure 4.5) shows significant non-zero flux (slope of the curve) at the pressure front location. In 2D and 3D cases, the flux at the pressure front location is much smaller. This explains why the PSS geometric approximation produces larger error in the 1D case due to the zero flux assumption at the pressure front location. *Gupta*

Table 4.1: Reservoir parameters for testing of oil case.

Reservoir permeability, k	0.001 md
Reservoir thickness, h	100 ft
Reservoir porosity, ϕ	0.1
Total compressibility, c_t	3×10^{-6} psi^{-1}
Bottom-hole flow rate, q	0.1 bbl/day
Fluid viscosity, μ	1 cp
Initial reservoir pressure, P_{init}	5000 psi
Wellbore radius, r_w	0.3 ft

Table 4.2: Geometry data for 1D, 2D, and 3D cases. r_0 is the inner boundary. A is the cross-sectional area in 1D linear flow. h is the thickness in 2D radial flow.

1D	2D	3D
$r_0 = 0.3$ ft $A = 2000$ ft^2	$r_0 = 0.3$ ft $h = 100$ ft	$r_0 = 3$ ft

(2012) has provided an in-depth analysis from a theoretical point of view. Based on these examples, the original PSS geometric approximation may not provide reliable solutions for general applications involving linear flow. Direct improvement on the PSS geometric approximation is possible and is still under investigation. However, using the τ-coordinate formulation will totally eliminate the error associated with the PSS assumption. In the following discussion, we will only focus on the new τ-coordinate formulation and demonstrate its performance.

To demonstrate the capability of handling different boundary conditions, we calculate the well flow rate by setting the BHP at 4000 psi. The results are shown in Figure 4.8 compared with the analytic solution.

Next we show an example of heterogeneous oil reservoir and demonstrate that the τ-coordinate formulation is capable of incorporating the heterogeneity information. The logarithm of the reservoir permeability is shown in Figure 4.9 (a). All other

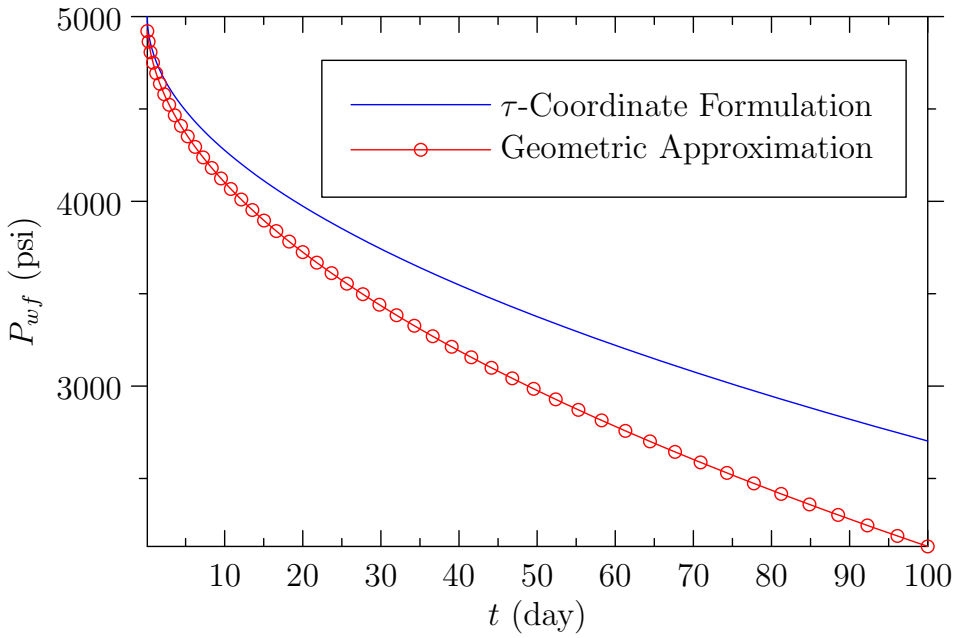

Figure 4.2: The BHP calculated by the PSS geometric approximation compared with the τ-coordinate formulation in 1D linear flow.

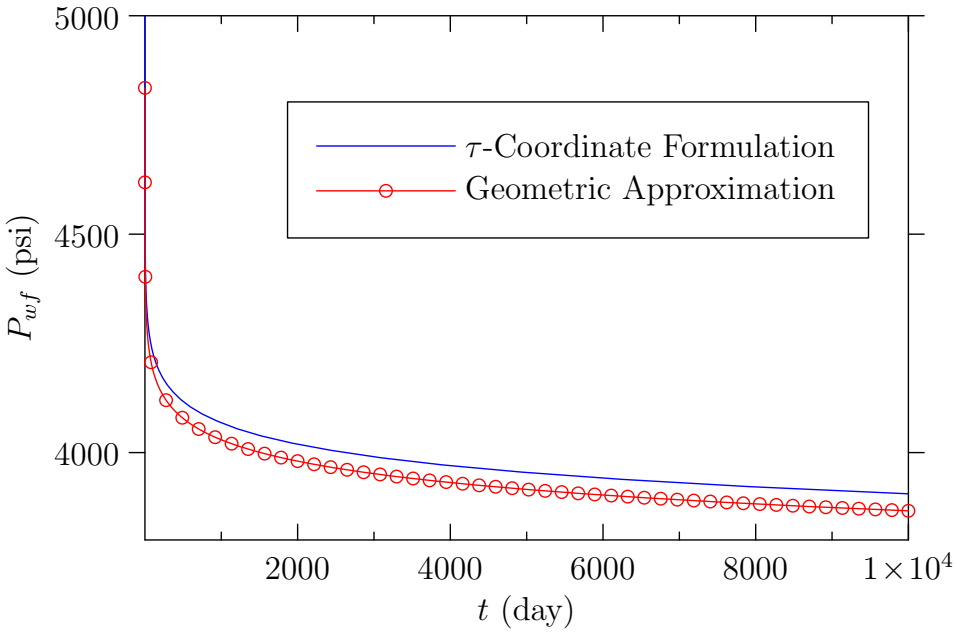

Figure 4.3: The BHP calculated by the PSS geometric approximation compared with the τ-coordinate formulation in 2D radial flow.

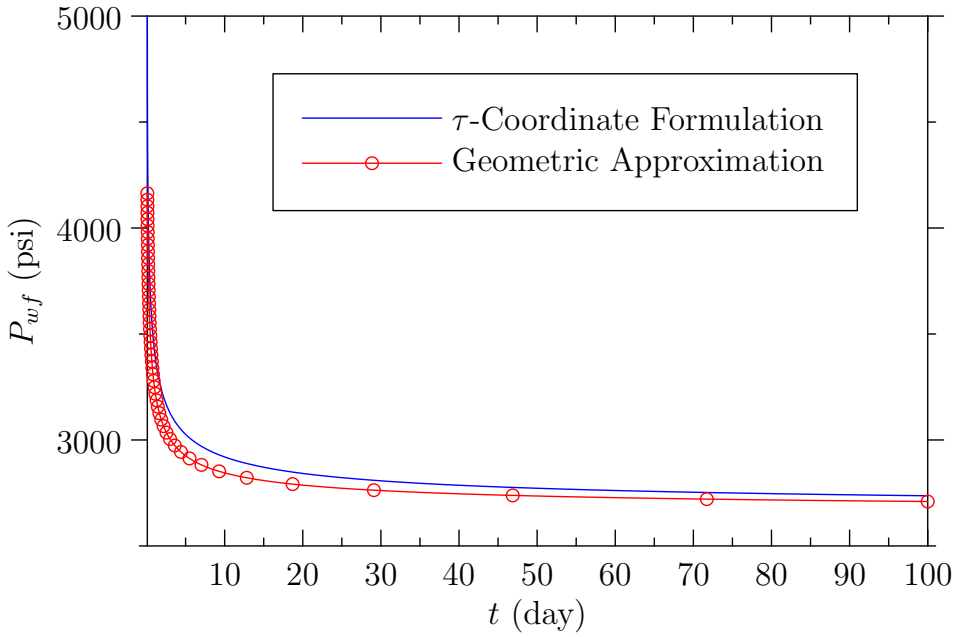

Figure 4.4: The BHP calculated by the PSS geometric approximation compared with the τ-coordinate formulation in 3D spherical flow.

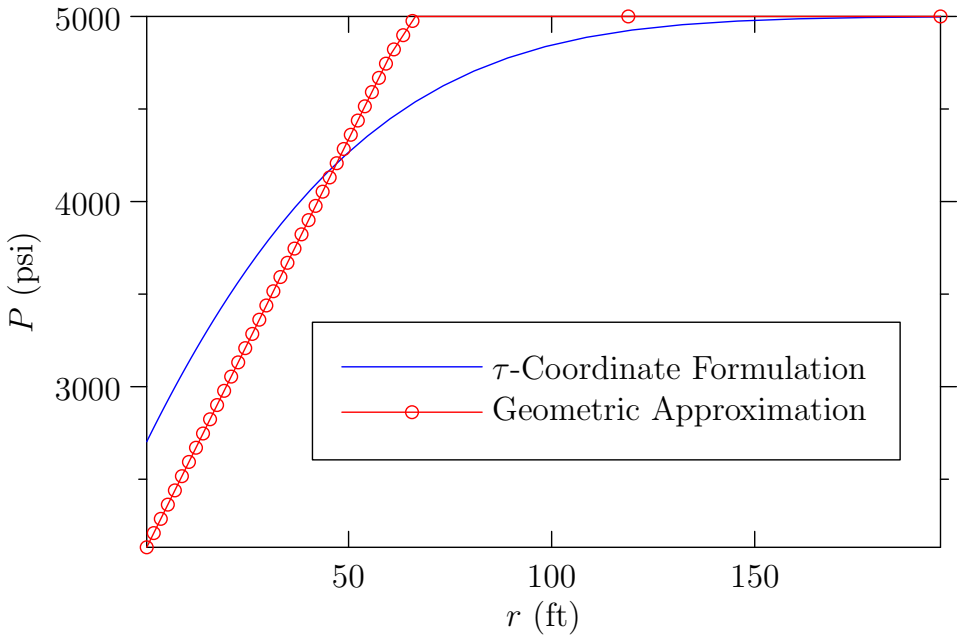

Figure 4.5: The pressure profile at the end of simulation calculated by the PSS geometric approximation compared with the τ-coordinate formulation in 1D linear flow.

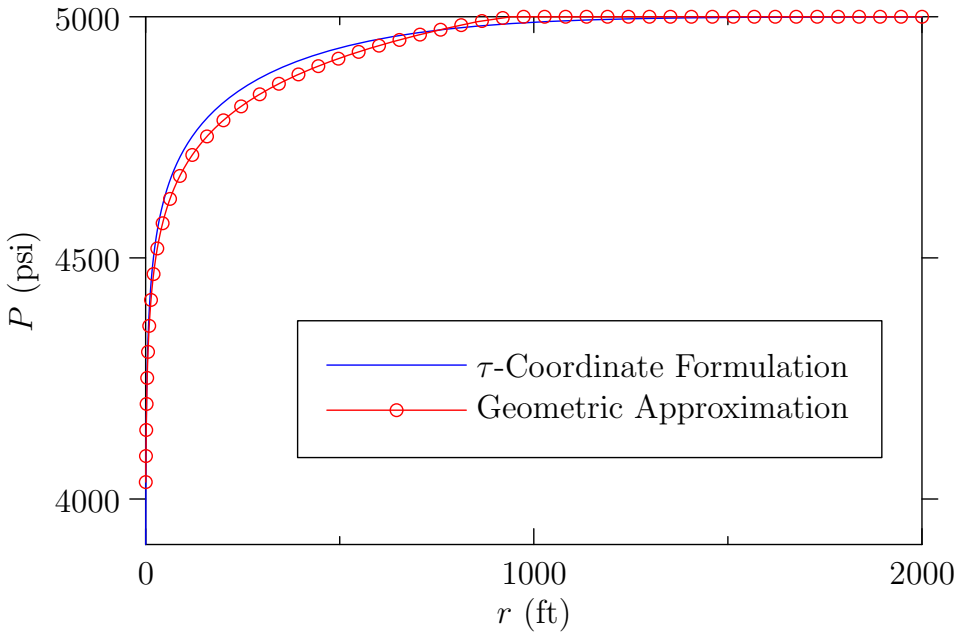

Figure 4.6: The pressure profile at the end of simulation calculated by the PSS geometric approximation compared with the τ-coordinate formulation in 2D radial flow.

parameters are the same as the homogeneous case and shown in Table 4.1. The diffusive time of flight map calculated by the FMM is shown in Figure 4.9 (b). Figure 4.10 illustrates the drainage pore volume as a function of τ and its first derivative (the $w(\tau)$ function). That is the essential information used in the τ-coordinate formulation. Figure 4.11 shows the BHP as a function of time for 10000 days. As we can see, the result obtained by the τ-coordinate formulation agrees well with the Eclipse simulation.

4.5.2 Gas Case

Reservoir parameters used for testing the gas case are shown in Table 4.3. The gas has a specific gravity of 0.7 and its formation volume factor and viscosity are shown in Figure 4.12 as functions of pressure. Figure 4.13 shows the calculated BHP versus

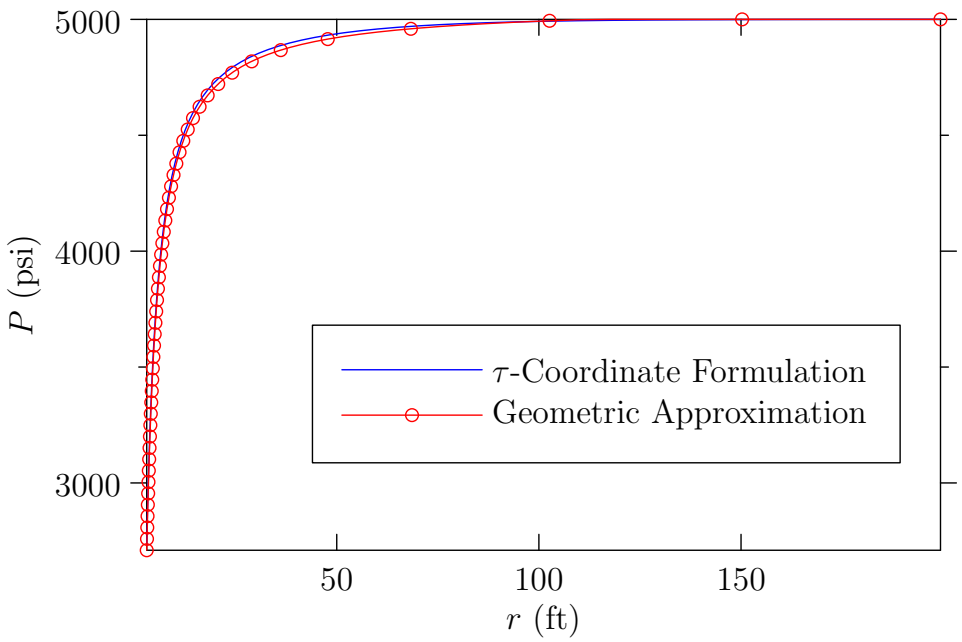

Figure 4.7: The pressure profile at the end of simulation calculated by the PSS geometric approximation compared with the τ-coordinate formulation in 3D spherical flow.

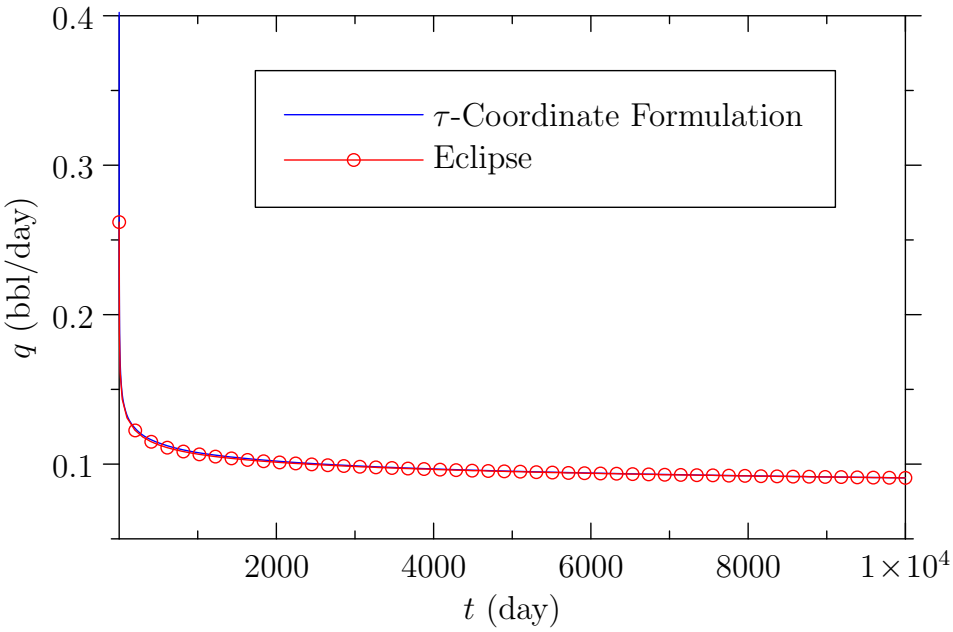

Figure 4.8: The calculated well bottom-hole flow rate under constant well BHP (4000 psi) using the τ-coordinate formulation and the Eclipse simulator for the homogeneous oil example.

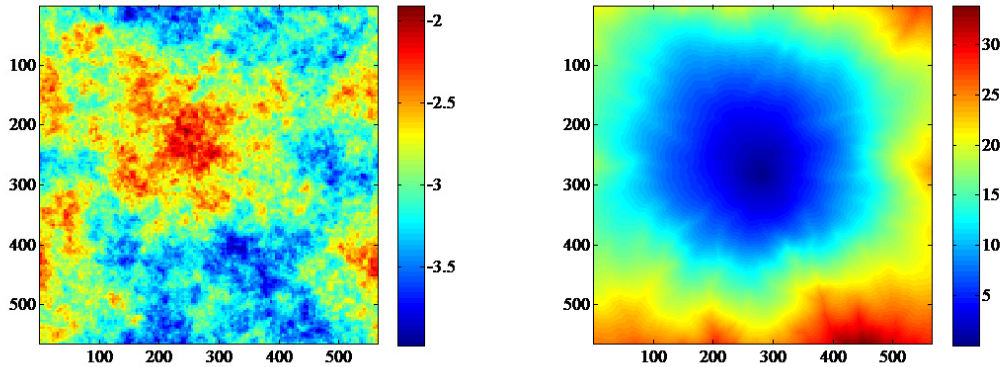

(a) (b)

Figure 4.9: (a) Logarithm of the permeability field used for testing. The grid is 564×564 with each grid block 5ft$\times$5ft. (b) Calculated diffusive time of flight τ for this permeability field for oil case.

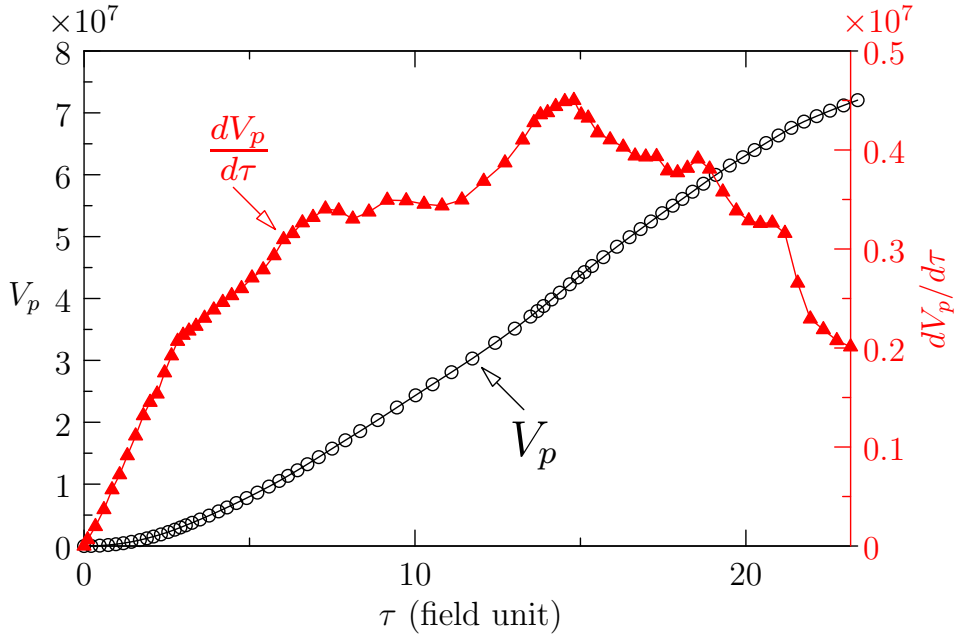

Figure 4.10: Drainage pore volume calculated as a function of the diffusive time of flight and its derivative for the heterogeneous oil reservoir example. All values are in field units shown in Table C.1

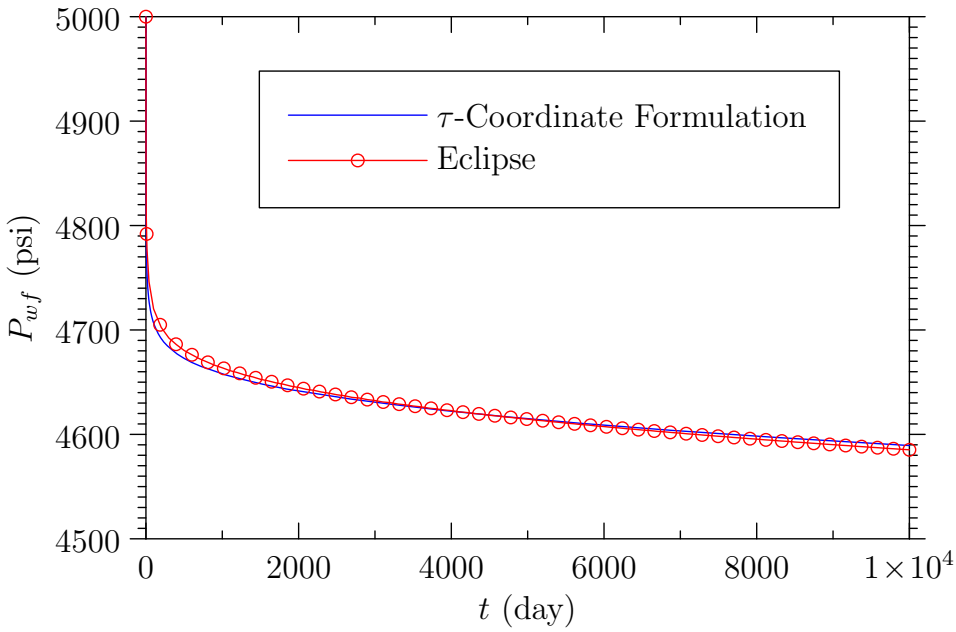

Figure 4.11: BHP calculated using the τ-coordinate formulation and the Eclipse simulator for the heterogeneous oil reservoir example.

Table 4.3: Reservoir parameters used for testing of gas case.

Reservoir permeability, k	0.0001 md
Reservoir thickness, h	100 ft
Reservoir porosity, ϕ	0.1
Formation compressibility, c_f	3×10^{-6} psi^{-1}
Gas specific gravity, γ	0.7
Gas flow rate, q	1 Mscf/day
Initial reservoir pressure, P_{init}	5000 psi
Wellbore radius, r_w	0.3 ft

time under constant rate constraint. As we can see, the τ-coordinate formulation agrees well with the Eclipse simulation result.

We tested the gas case using the same heterogeneous permeability shown in Figure 4.9 (a). Other parameters were taken from Table 4.3 as well. The calculated BHP by the τ-coordinate formulation is only slightly different from the Eclipse simulation as shown in Figure 4.14. Figure 4.15 shows the well flow rate under constant BHP (4500 psi) constraint. Again we observe a reasonable agreement between the τ-coordinate formulation and the Eclipse simulation.

One major advantage of the τ-coordinate formulation over the previous PSS geometric approximation is that it is relatively easy to handle complex well controls. As an example, Figure 4.16 shows the same heterogeneous gas case with changing flow rate and BHP controls.

4.5.3 Additional Physics

We use the homogeneous oil case for testing of the reservoir compaction effect. The reservoir parameters are shown in Table 4.1 for the base case. The permeability multiplier is shown in Figure 4.17 as a function of pore pressure. For simplicity, porosity is assumed to be constant. The calculated BHP with and without the compaction effect are shown in Figure 4.18. In this particular example, permeability

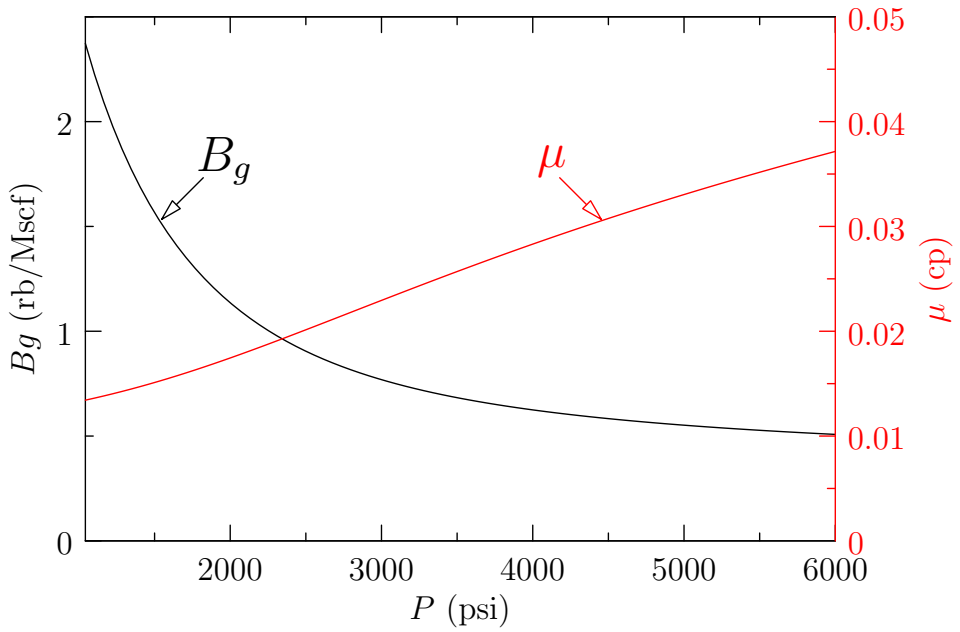

Figure 4.12: Gas formation volume factor B_g and gas viscosity μ as functions of pressure.

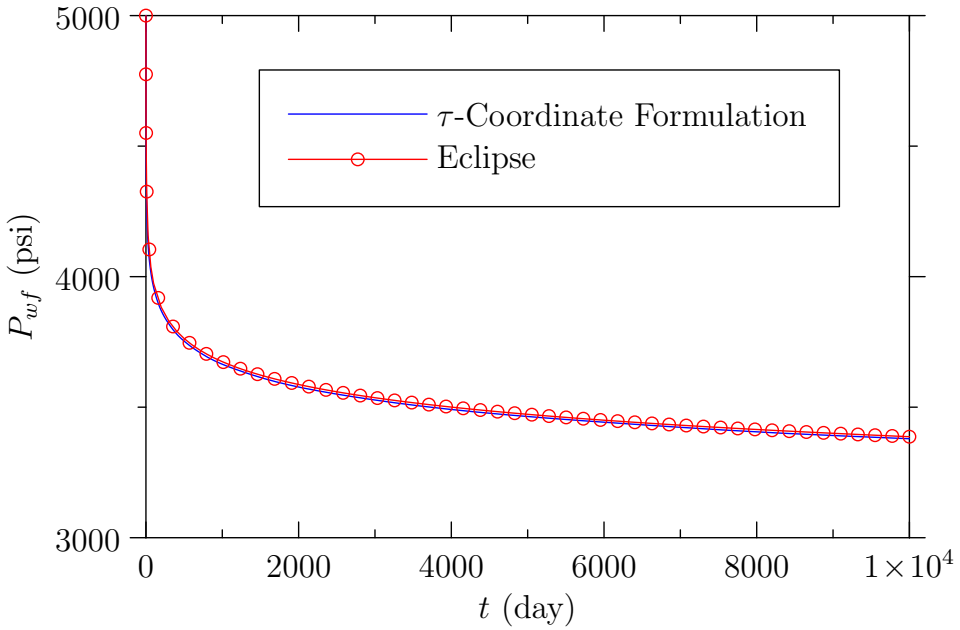

Figure 4.13: BHP calculated using the τ-coordinate formulation and the Eclipse simulator for the homogeneous gas reservoir example.

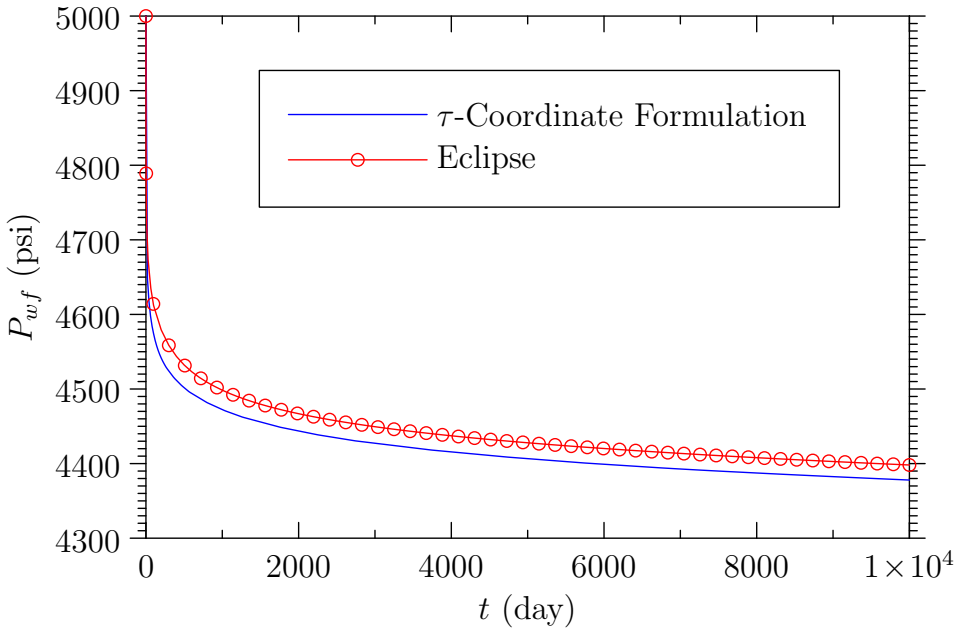

Figure 4.14: BHP calculated using the τ-coordinate formulation and the Eclipse simulator for the heterogeneous gas reservoir example.

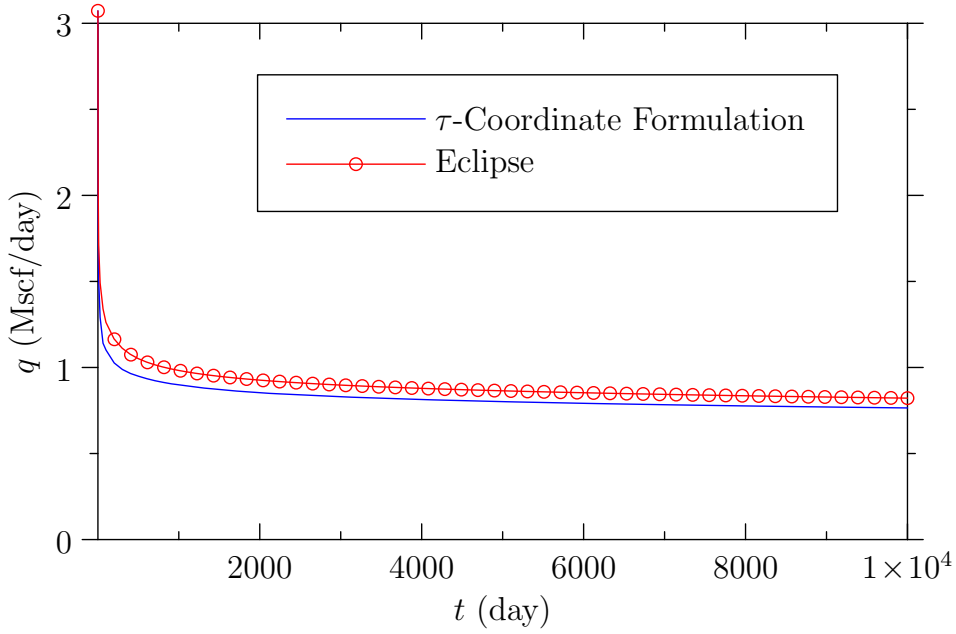

Figure 4.15: The well flow rate calculated under constant BHP (4500 psi) constraint using the τ-coordinate formulation and the Eclipse simulator for the heterogeneous gas reservoir example.

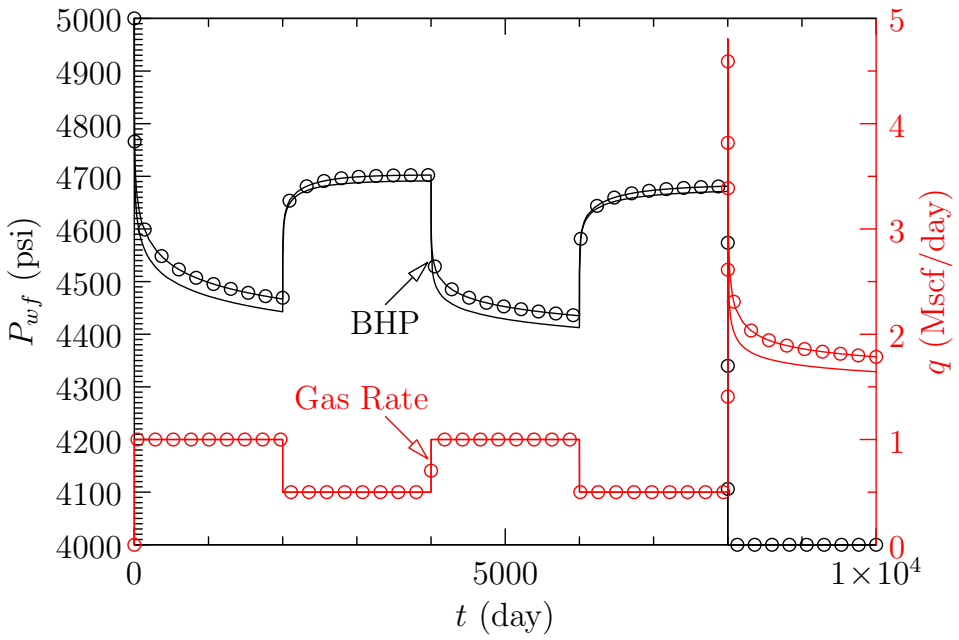

Figure 4.16: Comparison of BHP and well flow rate calculated using the τ-coordinate formulation (solid line) and the Eclipse simulation (circles) for the heterogeneous gas reservoir example under complex well flow rate and BHP controls.

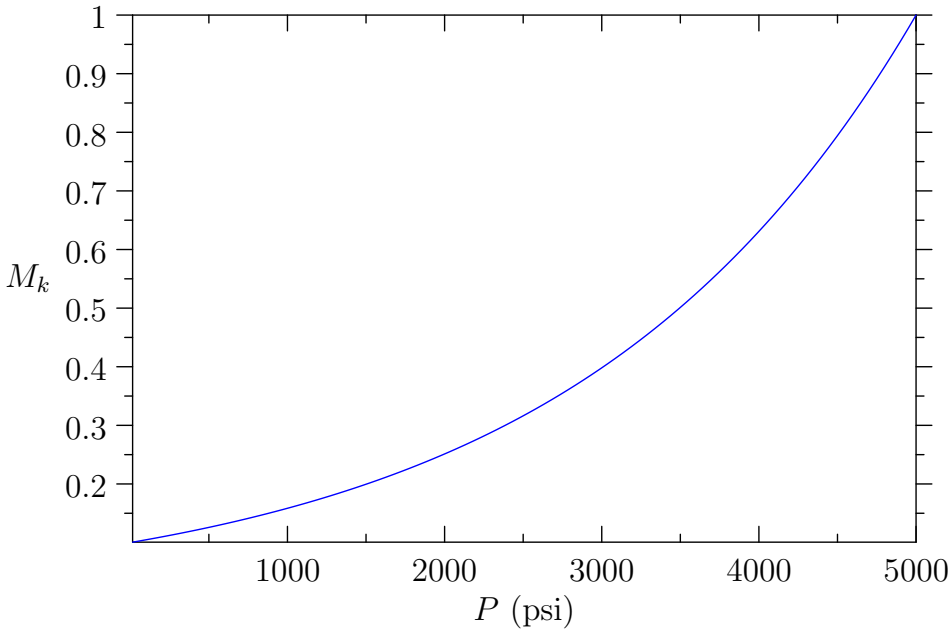

Figure 4.17: Permeability multiplier versus pore pressure due to reservoir compaction effect for the test case.

will decrease during pressure depletion. As a result, for constant production rate, the pressure drop becomes larger if the compaction effect is taken into account.

We use the homogeneous gas case for testing of the gas adsorption effect. The reservoir parameters are shown in Table 4.3 for the base case. We use the Langmuir isotherm model described in Section 1.1.4 for gas adsorption with the Langmuir volume $V_L = 2000$ scf/ft^3 and the Langmuir pressure $P_L = 4000$ psi. The calculated BHP with and without the gas adsorption effect are shown in Figure 4.19. The same calculation was done using Eclipse with gas adsorption option. It can be seen that our method produces consistent results compared with Eclipse. As we can see in Figure 4.19, the gas adsorption effect helps maintain the reservoir pressure, and thus the pressure will drop more slowly if gas adsorption is taken into consideration.

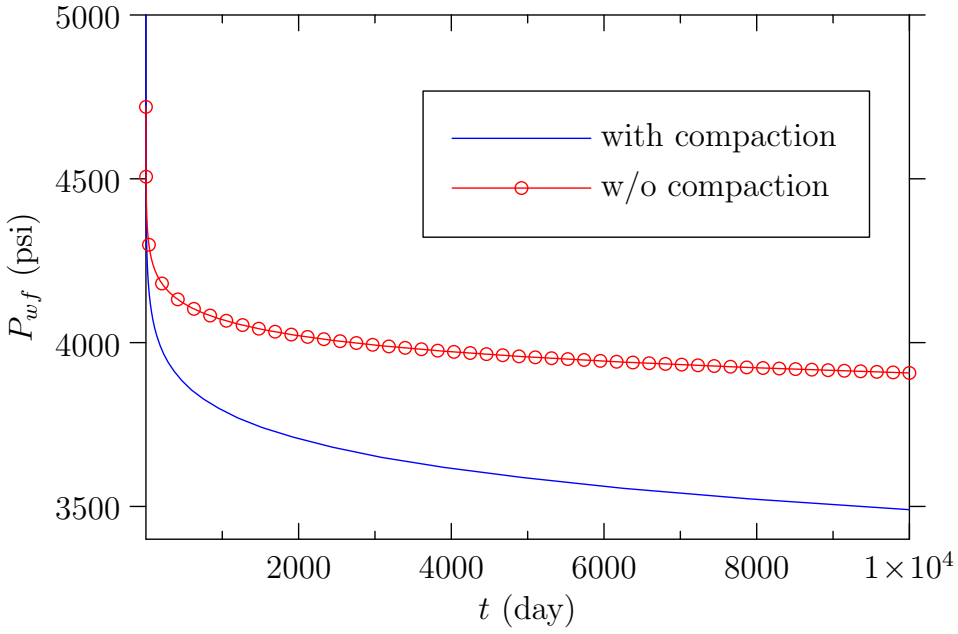

Figure 4.18: BHP calculated with and without the reservoir compaction effect using the τ-coordinate formulation.

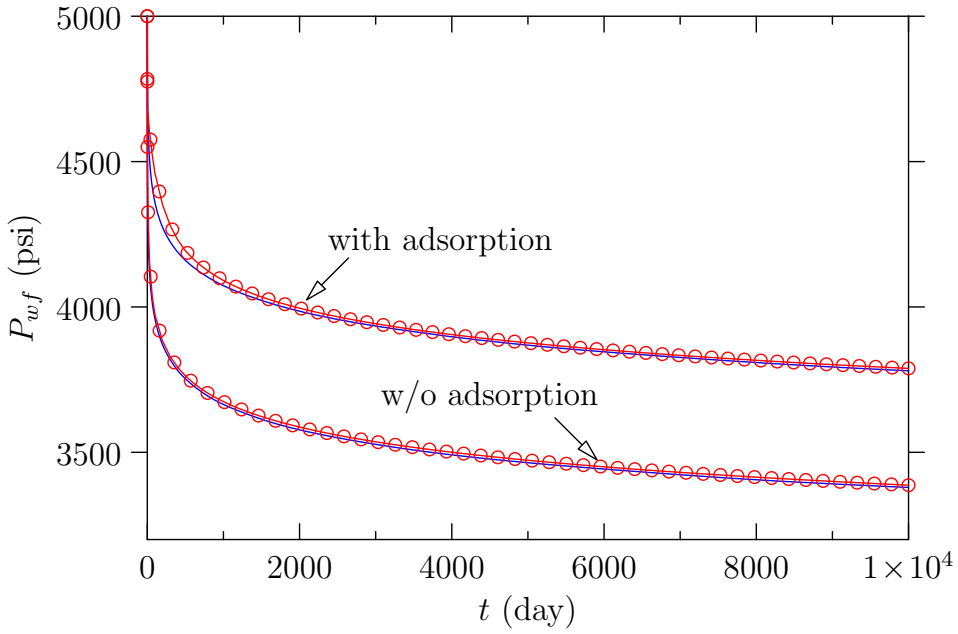

Figure 4.19: Gas adsorption effect calculated using the τ-coordinate formulation (solid lines) and the Eclipse simulation (circles) for the heterogeneous gas reservoir example.

4.6 Conclusions

In this section we have presented a novel formulation of the diffusivity equation using the diffusive time of flight τ as a spatial coordinate. The diffusive time of flight can be efficiently calculated using the FMM presented in the previous section. It is assumed that the diffusive time of flight contains the reservoir heterogeneity information and thus is able to reduce the three dimensional diffusivity equation to simply one dimensional in space. The major benefit is to significantly increase the numerical efficiency for pressure drainage calculation without losing too much of accuracy.

This τ-coordinate formulation also shows several advantages over the previously proposed PSS geometric approximation for pressure drainage calculation. It is able to eliminate the error produced by the PSS assumption. In addition, both pressure and flow rate well controls can be easily implemented using the same formulation. Last but not least, this formulation is quite general and can be extended to incorporate additional physical processes. We have demonstrated that the new formulation reduces back to the traditional diffusivity equation for homogeneous reservoirs. We have tested the performance of the new formulation for both oil and gas reservoirs under various well controls and reservoir properties. In general, the results obtained by the new τ-coordinate formulation agree will with either the analytical solution or the traditional finite difference reservoir simulation. We have demonstrated the ability of the method to take into account the reservoir compaction effect and the gas adsorption effect.

5. SUMMARY

In this dissertation, we have presented some important extensions to two highly efficient reservoir modeling methods, the streamline method and the Fast Marching Method. Both methods are alternatives to the conventional finite difference reservoir simulation. Mainly due to their numerical efficiency, they are often found to be advantageous over the conventional simulation technique for the purpose of dynamic reservoir characterization, which often requires fast forward modeling. The extensions we have achieved enable those methods to be applied to more complex grid geometries.

We have successfully extended the traditional streamline tracing algorithm, such as the Pollock's algorithm, to PEBI grids, unstructured triangular grids and grids with local refinement. Our recommended method uses a lower order interpolation scheme and satisfies local conservation. Its advantages include robustness and numerical efficiency. The recommendation is based on a comprehensive study of the velocity interpolation methods in polygons. The velocity interpolation methods investigated can assume lower order or higher order cell boundary fluxes, can be locally conservative or non-conservative, can produce continuous or discontinuous velocity field. All these alternatives are systematically evaluated according to criteria such as numerical error, efficiency, robustness etc. We have discovered that the interpolated velocity field has to be locally conservative in order to guarantee the correct volumetric transformation for the calculated streamlines and the time of flight. Results show that velocity continuity is a desirable property but may not be as important as local conservation for the purpose of streamline applications. The recommended method has been successfully applied to 2.5D PEBI grid, 2D and 3D LGR grids, and

faulted grids. For 3D LGR grids and faulted grids, the boundary layer approximation approached is applied to reduce the problem from 3D to 2D.

The formulation of the FMM in corner point grids has been developed based on the isoparametric mapping. The numerical discretization is demonstrated in detail using solution nodes based on cell centers and the local five-point stencil. For smoothly varying medium with anisotropy, we have demonstrated the causality condition if the principal direction of the permeability are aligned with the cell edges. For non-smoothly varying medium, we have done numerical experiments to study the effect of possible local violation of causality at the boundary of high permeability contrast. Results show that such effect can be mitigated by using nine-stencil scheme or doing grid refinement. An alternative discretization scheme using solution nodes based on cell vertexes can also be used to guarantee causality condition for locally high permeability contrast. However, the differences created by using different schemes are not very significant for practical applications. We have demonstrated using the FMM for drainage volume visualization for unconventional reservoirs and wells with multi-stage hydraulic fractures.

We have presented a novel formulation of the diffusivity equation using the diffusive time of flight as a spatial variable. This new formulation enables the calculation of pressure drainage based on the results of the FMM. Because the diffusive time of flight obtained by the FMM contains the reservoir heterogeneity information, the new formulation essentially reduces the 3D problem to only 1D in space. This greatly improves the numerical efficiency without losing too much of accuracy. The new formulation has been benchmarked by using various test cases including both oil and gas, homogeneous and heterogeneous reservoirs. The results have been compared with analytical solutions or commercial finite difference reservoir simulators. In order to deal with shale gas reservoirs, we have incorporated additional physical

processes in the formulation that could take into account reservoir compaction effect, gas adsorption effect etc.

REFERENCES

Aavatsmark, I., T. Barkve, Ø. Bøe, and T. Mannseth (1998), Discretization on unstructured grids for inhomogeneous, anisotropic media. part i: Derivation of the methods, *SIAM Journal on Scientific Computing*, *19*(5), 1700–1716.

Agarwal, R. G. (2010), Direct method of estimating average reservoir pressure for flowing oil and gas wells, in *SPE Annual Technical Conference and Exhibition*, Society of Petroleum Engineers, Florence, Italy, doi:10.2118/135804-MS.

Akkutlu, I. Y., and E. Fathi (2012), Multiscale gas transport in shales with local kerogen heterogeneities, *SPE Journal*, *17*(4), pp. 1002–1011, doi:10.2118/146422-PA.

Alton, K., and I. M. Mitchell (2008), Fast marching methods for stationary hamilton–jacobi equations with axis-aligned anisotropy, *SIAM Journal on Numerical Analysis*, *47*(1), 363–385, doi:10.1137/070680357.

Bourdet, D., J. Ayoub, and Y. Pirard (1989), Use of pressure derivative in well test interpretation, *SPE Formation Evaluation*, *4*(2), 293–302, doi:10.2118/12777-PA.

Bravo, M. C. (2007), Effect of transition from slip to free molecular flow on gas transport in porous media, *Journal of Applied Physics*, *102*(7), 074905, doi:10.1063/1.2786613.

Brezzi, F., and M. Fortin (1991), *Mixed and Hybrid Finite Element Methods*, Springer-Verlag, New York City.

Cipolla, C. L., E. Lolon, J. C. Erdle, and B. Rubin (2009), Reservoir modeling in shale-gas reservoirs, in *SPE Eastern Regional Meeting*, Society of Petroleum Engineers, Charleston, West Virginia, USA, doi:10.2118/125530-MS.

Cipolla, C. L., X. Weng, H. Onda, T. Nadaraja, U. Ganguly, and R. Malpani (2011a), New algorithms and integrated workflow for tight gas and shale completions, in *SPE Annual Technical Conference and Exhibition*, Society of Petroleum Engineers, Denver, Colorado, USA, doi:10.2118/146872-MS.

Cipolla, C. L., X. Weng, M. G. Mack, U. Ganguly, H. Gu, O. Kresse, and C. E. Cohen (2011b), Integrating microseismic mapping and complex fracture modeling to characterize fracture complexity, in *SPE Hydraulic Fracturing Technology Conference*, Society of Petroleum Engineers, The Woodlands, Texas, USA, doi: 10.2118/140185-MS.

Cipolla, C. L., S. C. Maxwell, and M. G. Mack (2012), Engineering guide to the application of microseismic interpretations, in *SPE Hydraulic Fracturing Technology Conference*, Society of Petroleum Engineers, The Woodlands, Texas, USA, doi:10.2118/152165-MS.

Clarkson, C. R., M. Nobakht, D. Kaviani, and T. Ertekin (2012), Production analysis of tight-gas and shale-gas reservoirs using the dynamic-slippage concept, *SPE Journal*, *17*(1), pp. 230–242, doi:10.2118/144317-PA.

Cordes, C., and W. Kinzelbach (1992), Continuous groundwater velocity fields and path lines in linear, bilinear, and trilinear finite elements, *Water Resour. Res.*, *28*, 2903–2911.

Darlow, B., R. Ewing, and M. Wheeler (1984), Mixed finite element method for miscible displacement problems in porous media, *SPE Journal*, *24*(4), 391–398, doi:10.2118/10501-PA.

Datta-Gupta, A., and M. King (2007), *Streamline Simulation: Theory and Practice*, Textbook Series, SPE, Richardson, Texas.

Datta-Gupta, A., J. Xie, N. Gupta, M. J. King, and L. W. J. (2011), Radius of investigation and its generalization to unconventional reservoirs, *JPT*, *63*(7), 52–55.

Edwards, M. G., and C. F. Rogers (1998), Finite volume discretization with imposed flux continuity for the general tensor pressure equation, *Computational Geosciences*, *2*(4), 259–290.

Fan, L., J. W. Thompson, and J. R. Robinson (2010), Understanding gas production mechanism and effectiveness of well stimulation in the haynesville shale through reservoir simulation, in *Canadian Unconventional Resources and International Petroleum Conference*, Society of Petroleum Engineers, Calgary, Alberta, Canada, doi:10.2118/136696-MS.

Fathi, E., and I. Y. Akkutlu (2013), Lattice boltzmann method for simulation of shale gas transport in kerogen, *SPE Journal*, *18*(1), pp. 27–37, doi:10.2118/146821-PA.

Fetkovich, M. (1980), Decline curve analysis using type curves, *Journal of Petroleum Technology*, *32*(6), 1065–1077, doi:10.2118/4629-PA.

Floater, M., K. Hormann, and G. Kós (2006), A general construction of barycentric coordinates over convex polygons, *Advances in Computational Mathematics*, *24*(1-4), 311–331.

Forsyth, P. A. (1990), A control-volume, finite-element method for local mesh refinement in thermal reservoir simulation, *SPE Reservoir Engineering*, *5*(4), 561–566, doi:10.2118/18415-PA.

Freeman, C., G. J. Moridis, D. Ilk, and T. Blasingame (2010), A numerical study of transport and storage effects for tight gas and shale gas reservoir systems, in *In-*

ternational Oil and Gas Conference and Exhibition in China, Society of Petroleum Engineers, Beijing, China, doi:10.2118/131583-MS.

Gupta, N. (2012), A novel approach for rapid estimation of drainage volume and prediction of pressure and rate behavior, Master's Thesis, Texas A&M University, College Station, TX, USA.

Hægland, H., H. Dahle, G. Eigestad, K.-A. Lie, and I. Aavatsmark (2007), Improved streamlines and time-of-flight for streamline simulation on irregular grids, *Advances in Water Resources*, *30*(4), 1027–1045.

Holdich, S. A. (2010), Shale gas holds global opportunities, *The American Oil & Gas Reporter*, *August 2010*, editor's choice, url: `http://www.aogr.com/index.php/magazine/editors-choice/shale-gas-holds-global-opportunities`.

Ilk, D., S. M. Currie, and T. A. Blasingame (2010), Production analysis and well performance forecasting of tight gas and shale gas wells, in *SPE Eastern Regional Meeting*, Society of Petroleum Engineers, Morgantown, West Virginia, USA, doi:10.2118/139118-MS.

Javadpour, F. (2009), Nanopores and apparent permeability of gas flow in mudrocks (shales and siltstone), *Journal of Canadian Petroleum Technology*, *48*(8), 16–21, doi:10.2118/09-08-16-DA.

Javadpour, F., D. Fisher, and M. Unsworth (2007), Nanoscale gas flow in shale gas sediments, *Journal of Canadian Petroleum Technology*, *46*(10), doi:10.2118/07-10-06.

Jimenez, E., K. Sabir, A. Datta-Gupta, and M. King (2005), Spatial error and conver-

gence in streamline simulation, in *SPE Reservoir Simulation Symposium*, Society of Petroleum Engineers, The Woodlands, Texas.

Jimenez, E., A. Datta-Gupta, and M. J. King (2010), Full-field streamline tracing in complex faulted systems with non-neighbor connections, *SPE Journal*, *15*(1), 7–17, doi:10.2118/113425-PA.

Kachuma, D. (2010), A robust streamline tracing method for systems with non-neighbor connections, in *Proceedings of the 12th European Conference on the Mathematics of Oil Recovery*, A039, Oxford, UK.

Kim, J., and G. J. Moridis (2012), Gas flow tightly coupled to elastoplastic geomechanics for tight and shale gas reservoirs: Material failure and enhanced permeability, in *SPE Americas Unconventional Resources Conference*, Society of Petroleum Engineers, Pittsburgh, Pennsylvania USA, doi:10.2118/155640-MS.

Kim, J. U., A. Datta-Gupta, R. Brouwer, and B. Haynes (2009), Calibration of high-resolution reservoir models using transient pressure data, in *SPE Annual Technical Conference and Exhibition*, Society of Petroleum Engineers, New Orleans, Louisiana, doi:10.2118/124834-MS.

King, M. J., P. R. Ballin, C. Bennis, D. E. Heath, A. D. Hiebert, W. McKenzie, J.-F. Rainaud, and J. Schey (2012), Reservoir modeling: From rescue to resqml, *SPE Reservoir Evaluation & Engineering*, *15*(2), 127–138, doi:10.2118/135280-PA.

Klinkenberg, L. J. (1941), The permeability of porous media to liquids and gases, in *Drilling and Production Practice*, pp. 200–213, American Petroleum Institute, New York City.

Konukoglu, E., M. Sermesant, O. Clatz, J.-M. Peyrat, H. Delingette, and N. Ayache (2007), A recursive anisotropic fast marching approach to reaction diffusion equation: application to tumor growth modeling, in *Proceedings of the 20th international conference on Information processing in medical imaging*, IPMI'07, pp. 687–699, Springer-Verlag, Berlin, Heidelberg.

Kulkarni, K. N., A. Datta-Gupta, and D. Vasco (2000), A streamline approach for integrating transient pressure data into high resolution reservoir models, in *SPE European Petroleum Conference*, Copyright 2000, Society of Petroleum Engineers Inc., Paris, France, doi:10.2118/65120-MS.

Langmuir, I. (1916), The constitution and fundamental properties of solids and liquids. part i. solids., *Journal of the American Chemical Society*, *38*(11), 2221–2295, doi:10.1021/ja02268a002.

Lee, S., P. Jenny, and H. A. Tchelepi (2002), A finite-volume method with hexahedral multiblock grids for modeling flow in porous media, *Computational Geosciences*, *6*(3-4), 353–379.

Lee, W. J. (1982), *Well Testing*, Seciety of Petroleum Engineers, Richardson, Texas.

Leliévre, P. G., C. G. Farquharson, and C. A. Hurich (2011), Computing first-arrival seismic traveltimes on unstructured 3-d tetrahedral grids using the fast marching method, *Geophysical Journal International*, *184*(2), 885–896.

Matringe, S., and M. Gerritsen (2004), On accurate tracing of streamlines, in *SPE Annual Technical Conference and Exhibition*, Society of Petroleum Engineers, Houston, Texas.

Matringe, S. F., R. Juanes, and H. A. Tchelepi (2006), Robust streamline tracing for

the simulation of porous media flow on general triangular and quadrilateral grids, *Journal of Computational Physics*, *219*(2), 992–1012.

Matringe, S. F., R. Juanes, and H. A. Tchelepi (2007), Streamline tracing on general triangular or quadrilateral grids, *SPE Journal*, *12*(2), 217–233, doi: 10.2118/96411-PA.

Matringe, S. F., R. Juanes, and H. A. Tchelepi (2008), Tracing streamlines on unstructured grids from finite volume discretizations, *SPE Journal*, *13*(4), 423–431, doi:10.2118/103295-PA.

Nordbotten, J. M., M. A. Celia, and S. Bachu (2004), Analytical solutions for leakage rates through abandoned wells, *Water Resour. Res.*, *40*(4), W04,204–.

Pollock, D. W. (1988), Semianalytical computation of path lines for finite-difference models, *Ground Water*, *26*(6), 743–750.

Ponting, D. (1989), Corner point geometry in reservoir simulation, in *1st European Conference on the Mathematics of Oil Recovery*, pp. 45–65, Oxford.

Prakash, C. (1987), Examination of the upwind formulation in the control volume finite-element method for fluid flow and heat transfer, *Numerical Heat Transfer*, *11*, 401–416, doi:10.1080/10407788708913562.

Prévost, M., M. G. Edwards, and M. J. Blunt (2001), Streamline tracing on curvilinear structured and unstructured grids, in *SPE Reservoir Simulation Symposium*, Society of Petroleum Engineers, Houston, Texas.

Qian, J., Y.-T. Zhang, and H.-K. Zhao (2007), A fast sweeping method for static convex hamilton-jacobi equations, *Journal of Scientific Computing*, *31*, 237–271, 10.1007/s10915-006-9124-6.

Rasmussen, A. (2010), Streamline tracing on irregular geometries, in *Proceedings of the 12th European Conference on the Mathematics of Oil Recovery*, A040.

Sethian, J. A. (1996), A fast marching level set method for monotonically advancing fronts, *Proceedings of the National Academy of Sciences*, *93*(4), 1591–1595.

Sethian, J. A. (1999a), *Level Set Methods and Fast Marching Methods: Evolving Interfaces in Computational Geometry, Fluid Mechanics, Computer Vision, and Materials Science*, Cambridge Monographs on Applied and Computational Mathematics, 2nd ed., Cambridge University Press, Cambridge, UK.

Sethian, J. A. (1999b), Fast marching methods, *SIAM Review*, *41*(2), 199–235.

Sethian, J. A., and A. Vladimirsky (2000), Fast methods for the eikonal and related hamilton-jacobi equations on unstructured meshes, *Proceedings of the National Academy of Sciences*, *97*(11), 5699–5703, doi:10.1073/pnas.090060097.

Sethian, J. A., and A. Vladimirsky (2001), Ordered upwind methods for static hamilton-jacobi equations, *Proceedings of the National Academy of Sciences*, *98*(20), 11,069–11,074, doi:10.1073/pnas.201222998.

Shabro, V., C. Torres-Verdin, and F. Javadpour (2011), Numerical simulation of shale-gas production: From pore-scale modeling of slip-flow, knudsen diffusion, and langmuir desorption to reservoir modeling of compressible fluid, in *North American Unconventional Gas Conference and Exhibition*, Society of Petroleum Engineers, The Woodlands, Texas, USA, doi:10.2118/144355-MS.

Shabro, V., C. Torres-Verdin, and K. Sepehrnoori (2012), Forecasting gas production in organic shale with the combined numerical simulation of gas diffusion in kerogen, langmuir desorption from kerogen surfaces, and advection in nanopores, in *SPE*

Annual Technical Conference and Exhibition, Society of Petroleum Engineers, San Antonio, Texas, USA, doi:10.2118/159250-MS.

Song, B., and C. A. Ehlig-Economides (2011), Rate-normalized pressure analysis for determination of shale gas well performance, in *North American Unconventional Gas Conference and Exhibition*, Society of Petroleum Engineers, The Woodlands, Texas, USA, doi:10.2118/144031-MS.

Sun, S., X. Gai, and M. F. Wheeler (2005), Streamline tracing on unstructured grids, in *SPE Annual Technical Conference and Exhibition*, Society of Petroleum Engineers, Dallas, Texas, doi:10.2118/96947-MS.

Sun, Y., and S. Fomel (1998), Fast-marching eikonal solver in the tetragonal coordinates, in *SEG Annual Meeting*, Society of Exploration Geophysicists, New Orleans, Louisiana.

Swami, V., and A. Settari (2012), A pore scale gas flow model for shale gas reservoir, in *SPE Americas Unconventional Resources Conference*, Society of Petroleum Engineers, Pittsburgh, Pennsylvania USA, doi:10.2118/155756-MS.

Valko, P. P., and W. J. Lee (2010), A better way to forecast production from unconventional gas wells, in *SPE Annual Technical Conference and Exhibition*, Society of Petroleum Engineers, Florence, Italy, doi:10.2118/134231-MS.

Vasco, D. W., H. Keers, and K. Karasaki (2000), Estimation of reservoir properties using transient pressure data: An asymptotic approach, *Water Resour. Res.*, *36*(12), 3447–3465.

Virieux, J., C. Flores-Luna, and D. Gibert (1994), Asymptotic theory for diffusive

electromagnetic imaging, *Geophysical Journal International*, *119*(3), 857–868, doi: 10.1111/j.1365-246X.1994.tb04022.x.

Wachspress, E. (1975), *A Rational Finite Element Basis*, Academic Press, New York.

Xie, J., N. Gupta, M. J. King, and A. D. gupta (2012a), Depth of investigation and depletion behavior in unconventional reservoirs using fast marching methods, in *SPE Europec/EAGE Annual Conference*, Society of Petroleum Engineers, Copenhagen, Denmark, doi:10.2118/154532-MS.

Xie, J., C. Yang, N. Gupta, M. J. King, and A. D. gupta (2012b), Integration of shale gas production data and microseismic for fracture and reservoir properties using fast marching method, in *SPE Eastern Regional Meeting*, Society of Petroleum Engineers, Lexington, Kentucky, USA, doi:10.2118/161357-MS.

Zhang, Y., M. J. King, and A. Datta-Gupta (2012), Robust streamline tracing using inter-cell fluxes in locally refined and unstructured grids, *Water Resour. Res.*, *48*(6), W06,521.

APPENDIX A

DERIVATION OF EQUATION 3.6

As shown in Figure A.1, and following *Ponting* (1989), the geometry of a corner point cell is defined by the tri-linear isoparametric mapping from the unit cube (α, β, γ) to physical space (x, y, z)

The tri-linear mapping from the unit cube point $\mathbf{x} = (\alpha, \beta, \gamma)$ to physical point $\mathbf{x} = (x, y, z)$ as follows:

$$\begin{aligned} \mathbf{x} \;=\; & \mathbf{x}_{000}(1-\alpha)(1-\beta)(1-\gamma) + \mathbf{x}_{100}\alpha(1-\beta)(1-\gamma) + \\ & \mathbf{x}_{010}(1-\alpha)\beta(1-\gamma) + \mathbf{x}_{110}\alpha\beta(1-\gamma) + \mathbf{x}_{001}(1-\alpha)(1-\beta)\gamma + \\ & \mathbf{x}_{101}\alpha(1-\beta)\gamma + \mathbf{x}_{111}\alpha\beta\gamma \end{aligned} \tag{A.1}$$

where the points $\mathbf{x}_{ijk}$ are eight cell corners. From this mapping we define three tangent vectors

$$\vec{\mathbf{t}}_i = \frac{\partial \mathbf{x}}{\partial \hat{x}_i} \qquad i = 1, 2, 3 \tag{A.2}$$

where $\hat{x}_i = (\alpha, \beta, \gamma)$, and three normal vectors

$$\vec{\mathbf{n}}_i = \vec{\mathbf{t}}_j \times \vec{\mathbf{t}}_k \qquad i, j, k = 1, 2, 3 \quad \textit{cyclic} \tag{A.3}$$

We have the following relationships

$$\vec{\mathbf{t}}_i \cdot \vec{\mathbf{n}}_j = \delta_{ij} J \tag{A.4}$$

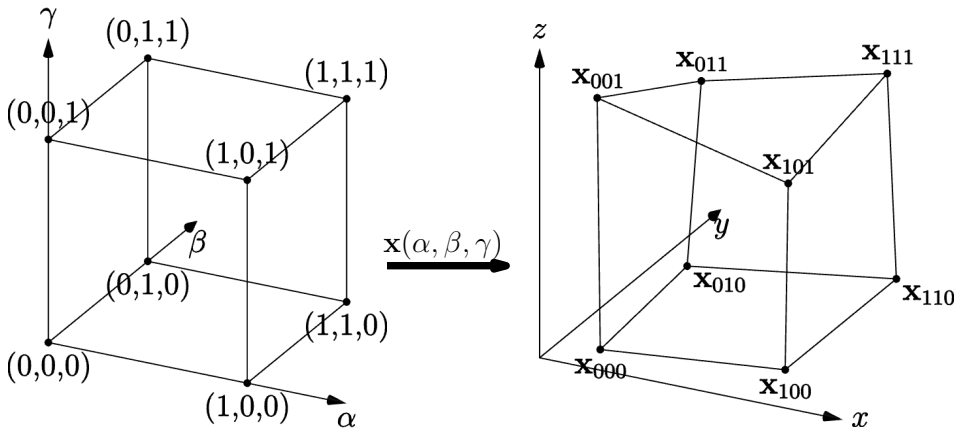

Figure A.1: Tri-linear isoparametric mapping from the unit cube to physical space

where δ_{ij} is the Kronecker delta and J is the Jacobian, and

$$\nabla = \sum_{i=1}^{3} \nabla \hat{x}_i \frac{\partial}{\partial \hat{x}_i} = \sum_{i=1}^{3} \frac{1}{J} \vec{\mathbf{n}}_i \frac{\partial}{\partial \hat{x}_i} \tag{A.5}$$

We will now derive Equation 3.6 based on the isoparametric mapping for corner point cells. Let us assume the principle directions of the permeability tensor are along the tangent vectors. Then the unit vectors associated with the principle directions of the permeability tensor are $\vec{\mathbf{t}}_i/t_i$ $(i = 1, 2, 3)$. In the reference space (unit cube), the permeability can be written as a diagonal tensor $\text{diag}(k_i)$. The transformation matrix $\mathbf{T}$ is obtained by putting together the unit vectors associated the principle directions as column vectors, i.e. $\mathbf{T} = [\vec{\mathbf{t}}_1/t_1, \vec{\mathbf{t}}_2/t_2, \vec{\mathbf{t}}_3/t_3]$. Thus the permeability tensor in the physical space is written as $\bar{\bar{k}} = \mathbf{T}\text{diag}(k_i)\mathbf{T}'$, which reduces to

$$\bar{\bar{k}} = \sum_{i=1}^{3} \frac{k_i}{t_i^2} \vec{\mathbf{t}}_i \vec{\mathbf{t}}_i \tag{A.6}$$

where k_i is the principle permeability in I, J, or K direction. Substituting Equations

A.5 and A.6 into the left hand side of Equation 3.6, we have

$$\vec{\nabla}\tau(\vec{x}) \cdot \bar{\bar{k}} \cdot \vec{\nabla}\tau(\vec{x}) = \sum_{i=1}^{3}\sum_{j=1}^{3}\sum_{k=1}^{3} \frac{1}{J}\vec{\mathbf{n}}_i \frac{\partial \tau}{\partial \hat{x}_i} \cdot \frac{k_j}{t_j^2}\vec{\mathbf{t}}_j\vec{\mathbf{t}}_j \cdot \frac{1}{J}\vec{\mathbf{n}}_k \frac{\partial \tau}{\partial \hat{x}_k} \tag{A.7}$$

Applying Equation A.4, we get

$$\vec{\nabla}\tau(\vec{x}) \cdot \bar{\bar{k}} \cdot \vec{\nabla}\tau(\vec{x}) = \sum_{i=1}^{3}\sum_{j=1}^{3}\sum_{k=1}^{3} \frac{\partial \tau}{\partial \hat{x}_i} \cdot \frac{k_j}{t_j^2} \frac{\partial \tau}{\partial \hat{x}_k} \delta_{ij}\delta_{jk} \tag{A.8}$$

This reduces to

$$\vec{\nabla}\tau(\vec{x}) \cdot \bar{\bar{k}} \cdot \vec{\nabla}\tau(\vec{x}) = \sum_{i=1}^{3} \frac{k_i}{t_i^2} \left(\frac{\partial \tau}{\partial \hat{x}_i} \right)^2 \tag{A.9}$$

This leads us to Equation 3.6.

APPENDIX B

FMM IN UNSTRUCTURED GRIDS

We will now discuss the local solution mentioned in step (4) of the basic framework of fast marching method in section 3.3. There are two distinct yet equivalent constructions of the local solver. One is based on the Fermat's principle; the other is based on Eulerian discretization. For simplicity, we will only discuss 2D case. The extension to 3D is straightforward. As shown in Figure B.1, we will first construct local triangles which are formed by the node considered (in red) and two of its adjacent neighbors. Then one of the local solvers is used to calculate the τ value based on each of the local triangle. Finally, the τ value to be updated at the node considered is the minimum value obtained from all the triangles. It can be seen from Figure B.1, both 5-stencil and 9-stencil Cartesian grids, as well as unstructured grids, can be treated in a uniform manner.

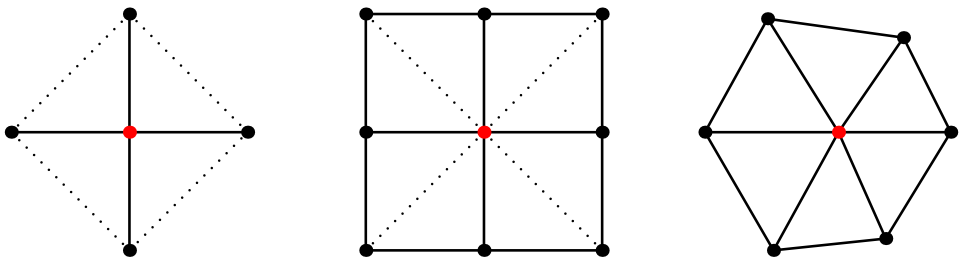

Figure B.1: Local triangles for the node in red in (a) 5-stencil square grid; (b) 9-stencil square grid; (c) Unstructured grid.

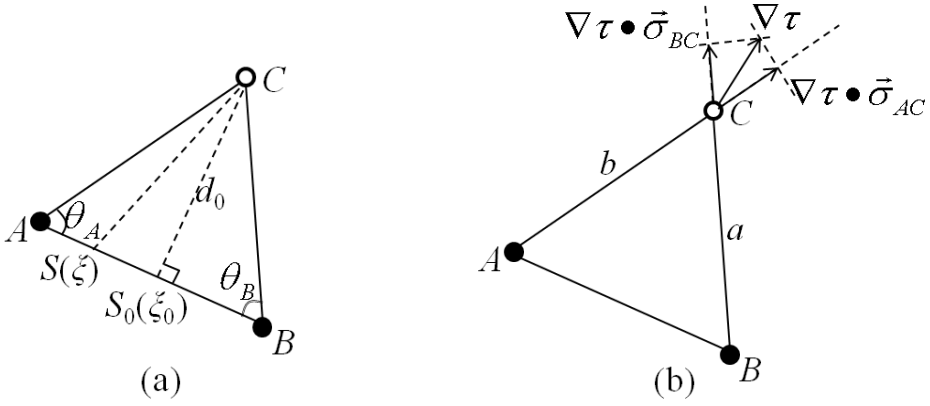

Figure B.2: Local solver based on (a) Fermat's principle and (b) Eulerian discretization

B.1 A Local Solver Based On Fermat's Principle

Here we follow the derivation of *Sun and Fomel* (1998); *Sethian* (1999b) in 2D. *Leliévre et al.* (2011) has given a 3D extension. Consider a local triangle ABC in Figure B.2(a). We would like to calculate the τ value at node C. If neither node A nor B have been accepted, we simply discard this local triangle for node C and look for the next one, because the true solution should not come from this local triangle. If only one node A or B has been accepted, then the τ value at node C can be simply calculated as a 1D problem either travelling from A to C or from B to C directly. Now we consider the case when both node A and B have been accepted and the τ values at nodes A and B are τ_A and τ_B respectively. For the lowest order approximation, we use plane wave assumption. Let ξ $(0 \leq \xi \leq 1)$ be the normalized distance from A to S along the segment AB. The travel time τ at point $S(\xi)$ is approximated by the linear interpolation:

$$\tau_S = (1-\xi)\tau_A + \xi\tau_B \tag{B.1}$$

According to Fermat's principle, the actual travel time to C corresponds to the minimum of the travel time with respect to path perturbations:

$$\tau_c = \min_{\xi \in (0,1]} \left\{ \tau_S + \sqrt{\frac{\|AB\|^2(\xi - \xi_0)^2 + d_0^2}{a}} \right\} \tag{B.2}$$

where $S_0(\xi_0)$ and d_0 are the normal projection point and the distance of C to AB. For isotropic case, diffusivity α is only a function of location and is taken at C. If the minimizer of the above equation ξ^* corresponds to the point S^* , then the direction along S^*C is the approximation of the characteristic direction. The minimization constraint $0 \leq \xi \leq 1$ makes sure the causality relationship is satisfied, i.e. the characteristic direction estimated lies inside the triangle and thus

$$\tau_C \geq \max\{\tau_A, \tau_B\} \tag{B.3}$$

This causality relationship makes sure that the acceptance of solution values will always in ascending order. Equation B.2 can be solved by setting the derivative to zero

$$\tau_B - \tau_A + \frac{\|AB\|^2(\xi - \xi_0)}{\sqrt{\alpha\|AB\|^2(\xi - \xi_0)^2 + \alpha d_0^2}} = 0 \tag{B.4}$$

This is a quadratic equation for ξ and the solution is

$$\xi = \xi_0 \pm \frac{d_0(\tau_A - \tau_B)}{\|AB\|\sqrt{\frac{\|AB\|^2}{\alpha} - (\tau_A - \tau_B)^2}} \tag{B.5}$$

We need to select the appropriate branch of solution in [0, 1] and then we can obtain the solution

$$\tau_C = d_0\sqrt{\frac{1}{\alpha} - \frac{(\tau_A - \tau_B)^2}{\|AB\|^2}} + \frac{\|BC\|}{\|AB\|}\tau_A \cos\theta_B + \frac{\|AC\|}{\|AB\|}\tau_B \cos\theta_A \tag{B.6}$$

B.2 A Local Solver Based On An Eulerian Discretization

Here we follow the derivation of *Sethian and Vladimirsky* (2000) and *Qian et al.* (2007). As shown in Figure B.2(b), let a be the length of BC and b be the length of AC. Let $\vec{\sigma}_{AC}$ be the unit vector pointing from A to C and $\vec{\sigma}_{BC}$ be the unit vector pointing from B to C. Thus,

$$\vec{\sigma}_{AC} = \frac{1}{b}(x_C - x_A, y_C - y_A) \tag{B.7}$$

$$\vec{\sigma}_{BC} = \frac{1}{a}(x_C - x_B, y_C - y_B) \tag{B.8}$$

Assuming a linear approximation of τ locally, we have the following finite difference equations

$$\frac{1}{b}(\tau_C - \tau_A) = \nabla\tau \cdot \vec{\sigma}_{AC} \tag{B.9}$$

$$\frac{1}{a}(\tau_C - \tau_B) = \nabla\tau \cdot \vec{\sigma}_{BC} \tag{B.10}$$

If we define matrix $\mathbf{P}$ with rows to be $\vec{\sigma}_{AC}$ and $\vec{\sigma}_{BC}$, then the above equations can be written in matrix form as

$$\begin{pmatrix} \frac{\tau_C - \tau_A}{b} \\ \frac{\tau_C - \tau_B}{a} \end{pmatrix} = \mathbf{P}\nabla\tau \tag{B.11}$$

Thus

$$\nabla\tau = \mathbf{P}^{-1} \begin{pmatrix} \frac{\tau_C - \tau_A}{b} \\ \frac{\tau_C - \tau_B}{a} \end{pmatrix} \tag{B.12}$$

Substitute the above equation into the Eikonal equation, we will get

$$\left(\frac{\tau_C-\tau_A}{b},\frac{\tau_C-\tau_B}{a}\right)\mathbf{P}^{-1}\alpha(\mathbf{P})^T\begin{pmatrix}\frac{\tau_C-\tau_A}{b}\\ \frac{\tau_C-\tau_B}{a}\end{pmatrix}=1 \tag{B.13}$$

This quadratic equation is solved for τ_C and the solution should be verified against the causality condition: the solved value of τ_C can only be accepted, if the update is coming from within that triangle, i.e., only if the computed characteristic direction lies inside the triangle. The reader is referred to *Qian et al.* (2007) for the details of this verification process. If there is no real solution from Equation B.13 or the real solutions fail to pass the causality condition, then we simply take the minimum value of the two 1D solutions from A and B directly to C as the value of τ_C:

$$\tau_C=\min\left(\tau_A+\frac{b^2}{\alpha},\tau_B+\frac{a^2}{\alpha}\right) \tag{B.14}$$

As shown in Figure B.1, both 5-stencil and 9-stencil Cartesian grids as well as triangular unstructured grids can all be treated in a uniform manner. For example, if 5-stencil Cartesian grid is used, such as shown in Figure B.1(a), the matrix $\mathbf{P}$ simply becomes identity matrix and Equation B.13 reduces back to the ordinary finite difference discretization in x and y directions. Using 9-stencil Cartesian grid or unstructured grid will provide better spatial resolution to more accurately estimate the characteristic direction and thus generally produce better results than the 5-stencil Cartesian grid.

Compared with the local solver based on Fermat's principle, Equation B.13 can be more straightforwardly extended to 3D case in a tetrahedron. It is also more convenient to be extended to anisotropic case (α becomes a tensor) or to use higher order approximations (*Sethian and Vladimirsky*, 2000). However, the local solver

based on Fermat's principle is more transparent to the physical meaning behind the solution and shows the causality condition in a way much easier to be understood.

APPENDIX C

REWRITING THE DIFFUSIVITY EQUATION USING THE τ-COORDINATE

C.1 Extension to Anisotropy

In this section we will derive Equation 4.17 from a different perspective to include anisotropy into the formulation. Let us imagine that we have a series of τ coutour surfaces partitioning the domain into a series of non-overlapping layers. Consider a very thin layer of volume enclosed by the contour surfaces $S(\tau)$ and $S(\tau + \Delta\tau)$. The volume element of this thin layer $d\nu$ can be written as the area element $d\sigma$ multiplied by the thickness of the layer

$$d\nu = \frac{\Delta\tau}{\|\nabla\tau\|} d\sigma \tag{C.1}$$

The diffusion equation can be written as

$$-\nabla \cdot \vec{\mathbf{u}} = \phi c_t \frac{\partial P}{\partial t} \tag{C.2}$$

We take the volumetric integral over the thin layer

$$-\oint_V \nabla \cdot \vec{\mathbf{u}} d\nu = \oint_V \phi c_t \frac{\partial P}{\partial t} d\nu \tag{C.3}$$

The left hand side can be written as the surface integral by applying Green's theorem

$$-\oint_V \nabla \cdot \vec{\mathbf{u}} d\nu = -\oint_S \vec{\mathbf{u}} \cdot \hat{\mathbf{n}} d\sigma = -\oint_S \vec{\mathbf{u}} \cdot \nabla\tau \frac{d\sigma}{\|\nabla\tau\|} \tag{C.4}$$

The surface integral can then be written in terms of the two τ contour surfaces enclosing the thin layer

$$-\oint_S \vec{\mathbf{u}} \cdot \nabla\tau \frac{d\sigma}{\|\nabla\tau\|} = -\left(\int_{S(\tau+\Delta\tau)} \nabla\tau \cdot \vec{\mathbf{u}} \frac{d\sigma}{\|\nabla\tau\|} - \int_{S(\tau)} \nabla\tau \cdot \vec{\mathbf{u}} \frac{d\sigma}{\|\nabla\tau\|} \right) \tag{C.5}$$

The right hand side of Equation C.3 can also be written as a surface integral by applying Equation C.1

$$\oint_V \phi c_t \frac{\partial P}{\partial t} d\nu = \Delta\tau \int_{S(\tau)} \phi c_t \frac{\partial P}{\partial t} \frac{d\sigma}{\|\nabla\tau\|} \tag{C.6}$$

For anisotropic permeability the velocity is given by Darcy's Law as

$$\vec{\mathbf{u}} = -\frac{\bar{\bar{k}}}{\mu} \cdot \nabla P \tag{C.7}$$

Under the assumption that the pressure gradient direction aligns with the τ gradient direction, i.e., the contour surfaces of τ are also the contour surfaces of P, we can apply Equation 4.10 and get

$$\vec{\mathbf{u}} \approx -\frac{\bar{\bar{k}}}{\mu} \cdot \nabla\tau \frac{\partial P}{\partial \tau} \tag{C.8}$$

Substituting Equation C.8 into Equation C.5 and applying the anisotropic Eikonal equation $\nabla\tau \cdot \bar{\bar{k}} \cdot \nabla\tau = \phi\mu c_t$, we are able to eliminate the permeability tensor completely. Thus the original diffusion equation (Equation C.3) has been transformed into

$$\int_{S(\tau+\Delta\tau)} \phi \frac{\partial P}{\partial \tau} \frac{d\sigma}{\|\nabla\tau\|} - \int_{S(\tau)} \phi \frac{\partial P}{\partial t} \frac{d\sigma}{\|\nabla\tau\|} = \Delta\tau \int_{S(\tau)} \phi \frac{\partial P}{\partial \tau} \frac{d\sigma}{\|\nabla\tau\|} \tag{C.9}$$

Table C.1: Field units used in Equation C.13.

Quantity	Unit	Quantity	Unit
Pressure	psi	Length	ft
Time	day	Permeability	md
Viscosity	cp	Compressibility	psi^{-1}
Oil flow rate	bbl/day	Drainage pore volume	ft^3
Gas flow rate	scf/day	Temperature	°R

Divide both sides by $\Delta\tau$ and let $\Delta\tau \to 0$

$$\frac{\partial}{\partial\tau}\left(\int_{S(\tau)} \phi \frac{\partial P}{\partial\tau}\frac{d\sigma}{\|\nabla\tau\|}\right) = \int_{S(\tau)} \phi \frac{\partial P}{\partial t}\frac{d\sigma}{\|\nabla\tau\|} \tag{C.10}$$

Under the assumption that pressure is only a function of τ and t, we can take terms containing only P outside the integral. Then we arrive at exactly the same form as Equation 4.17,

$$\frac{\partial}{\partial\tau}\left(w(\tau)\frac{\partial P}{\partial\tau}\right) = w(\tau)\frac{\partial P}{\partial t}$$

with

$$w(\tau) = \int_{S(\tau)} \phi \frac{d\sigma}{\|\nabla\tau\|} = \frac{dV_p(\tau)}{d\tau} \tag{C.11}$$

The relationship between $w(\tau)$ and the drainage pore volume $V_p(\tau)$ can be established by writing $V_p(\tau)$ according to Equation C.1

$$V_p(\tau) = \int_{\tau_0}^{\tau}\left(\int_{S(\tau)} \phi \frac{d\sigma}{\|\nabla\tau\|}\right) d\tau \tag{C.12}$$

In field units shown in Table C.1, Equation 4.17 is

$$\frac{\partial}{\partial\tau}\left(w(\tau)\frac{\partial P}{\partial\tau}\right) = 158.2\, w(\tau)\frac{\partial P}{\partial t} \tag{C.13}$$

C.2 Extension to Compressible Fluid (Gas)

For compressible fluid (gas), the fluid viscosity μ and compressibility c_g will depend on pressure. When we calculate the diffusive time of flight τ using FMM, we will use the values at the initial reservoir pressure μ_i and c_{gi} respectively. The total compressibility at the initial reservoir pressure is then $c_{ti} = c_{gi} + c_f$, where c_f is the rock compressibility and considered to be contant. For real gas, the diffusivity equation can be written as

$$-\nabla \cdot (\rho \vec{\mathbf{u}}) = \frac{\partial(\phi\rho)}{\partial t} \tag{C.14}$$

The equation of state for real gas is

$$PV = Z\frac{m}{M}RT \tag{C.15}$$

Thus the gas density can be expressed as

$$\rho = \frac{PM}{ZRT} \tag{C.16}$$

The gas compressibility is

$$c_g = -\frac{1}{V}\frac{\partial V}{\partial P} = \frac{1}{\rho}\frac{\partial \rho}{\partial P} \tag{C.17}$$

The rock compressibility is

$$c_f = \frac{1}{\phi}\frac{\partial \phi}{\partial P} \tag{C.18}$$

The total compressibility is defined as

$$c_t = c_g + c_f \tag{C.19}$$

By applying Equations C.15 to C.19 we can have the right hand side of Equation C.14 as

$$\frac{\partial(\phi\rho)}{\partial t} = \frac{M}{RT}\phi c_t \frac{P}{Z}\frac{\partial P}{\partial t} \tag{C.20}$$

The left hand side of Equation C.14 is only different from Equation C.3 by an extra density. Following exactly the same derivation as in Appendix C.1 and applying Equation C.16 for gas density, we can derive the following equation

$$\frac{\partial}{\partial \tau}\left(w(\tau)\frac{P}{\tilde{\mu}(P)Z(P)}\frac{\partial P}{\partial \tau}\right) = w(\tau)\tilde{c}_t(P)\frac{P}{Z(P)}\frac{\partial P}{\partial t} \tag{C.21}$$

where function $w(\tau)$ has been defined previously, $\tilde{\mu}(P)$ and $\tilde{c}_t(P)$ are dimensionless viscosity and total compressibility defined as

$$\tilde{\mu}(P) = \frac{\mu(P)}{\mu_i} \tag{C.22}$$

and

$$\tilde{c}_t(P) = \frac{c_t(P)}{c_{ti}} \tag{C.23}$$

If we define the real gas pseudo-pressure as

$$m(P) = \int_{P_0}^{P} \frac{PdP}{\tilde{\mu}(P)Z(P)} \tag{C.24}$$

Then Equation can be written as

$$\frac{\partial}{\partial \tau}\left(w(\tau)\frac{\partial m}{\partial \tau}\right) = w(\tau)\tilde{c}_t(m)\tilde{\mu}(m)\frac{\partial m}{\partial t} \tag{C.25}$$

$\tilde{\mu}(P)$ and $\tilde{c}_t(P)$ are functions of P and thus are also functions of m. By using a pseudo-time defined as

$$t_s(t) = \int_{t_0}^{t} \frac{dt}{\tilde{c}_t \tilde{\mu}} \tag{C.26}$$

the equation can be further reduced to the same form as the slightly compressible case

$$\frac{\partial}{\partial \tau}\left(w(\tau)\frac{\partial m}{\partial \tau}\right) = w(\tau)\frac{\partial m}{\partial t_s} \tag{C.27}$$

The pressure boundary conditions for gas case is the same as the oil gas shown in Equation 4.36 and 4.37. The rate boundary conditions can be written for the wellbore as

$$\left(w(\tau)\frac{\partial m}{\partial \tau}\right)_{\tau=\tau_w} = 2 \times \frac{P_{ST}T}{T_{ST}\mu_i c_{ti}} q_w \tag{C.28}$$

Here q_w is the gas flowing rate at the standard condition. Similar equation can be written for the outer boundary.

APPENDIX D

PSS GEOMETRIC APPROXIMATION IN HOMOGENEOUS RESERVOIRS

Based on the equation of depth of investigation equation (Equation 1.19) for linear, radial, and spherical flow, the drainage volume functions can be written analytically as

$$V_p(t) = \phi A(\sqrt{2\alpha t}) \tag{D.1}$$

for 1D linear flow,

$$V_p(t) = \phi h\pi(\sqrt{4\alpha t})^2 \tag{D.2}$$

for 2D radial flow, and

$$V_p(t) = \phi\frac{4}{3}\pi(\sqrt{6\alpha t})^3 \tag{D.3}$$

for 3D spherical flow. Here A is the cross-sectional area for 1D linear flow, and h is the domain thickness for 2D radial flow. Substituting these drainage volume functions into Equation 4.5 and integrating over time. Due to the PSS assumption, at any particular location r, the pressure drop only occurs after the pressure front arrives at this location. Therefore, the pressure drop at location r can be calculated by integrating Equation 4.5 from time $t = r^2/(\beta\alpha)$. Here β is 2, 4, and 6 for 1D, 2D, and 3D cases. Thus pressure profile at any given time can be calculated according to such integration. At the inner boundary r_0, we can get the analytical solution of the pressure as functions of time. For 1D linear flow, we have

$$P_{wf}(t) = P_i - \frac{\mu q r_0}{Ak}\left(\sqrt{\frac{2\alpha t}{r_0^2}+1}-1\right) \tag{D.4}$$

For 2D radial flow, we have

$$P_{wf}(t) = P_i - \frac{\mu q}{4\pi k h} \ln\left(\frac{4\alpha t}{r_0^2} + 1\right) \tag{D.5}$$

For 3D spherical flow, we have

$$P_{wf}(t) = P_i - \frac{\mu q}{4\pi k r_0}\left[1 - \left(\frac{6\alpha t}{r_0^2} + 1\right)^{-\frac{1}{2}}\right] \tag{D.6}$$